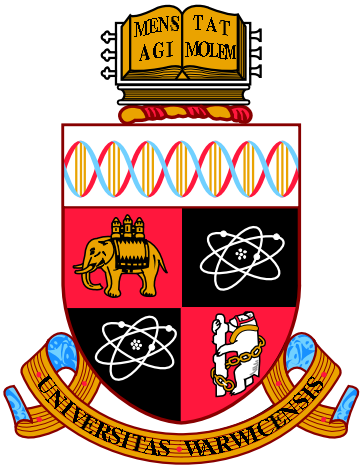

Mathematical modelling and simulations of the ion transport through confined geometries.

by

Bartlomiej Matejczyk

Thesis

Submitted to the University of Warwick

for the degree of

Doctor of Philosophy

Mathematics Institute The University of Warwick

2019

THE UNIVERSITY OF WARWICK

Contents

List of Figures

Acknowledgments

First and foremost I would like to express my sincere gratitude to my supervisor Dr Marie-Therese Wolfram for her patience, invaluable guidance, and continuous support throughout my doctoral studies. She has always found time to share her mathematical knowledge and insight and I have greatly benefited from the research environment she created.

I must thank all of my collaborators: Prof. Dr Jan-Frederik Pietschmann, Dr Giles Richardson, Dr Clemens Guhlke, Dr Rüdiger Müller as well as the entire group of Prof. Dezső Boda. I believe that all the hours we spent discussing every single detail were crucial for this thesis.

I am deeply grateful to Prof. Christian Schmeiser and Dr Björn Stinner, for many excellent suggestions which helped to improve the thesis and for their general advice.

Finally, I want to thank my family and friends for their constant support and encouragement.

Declarations

The work described in this thesis is the author's own, conducted under the supervision of Marie-Therese Wolfram (University of Warwick), except where otherwise stated. More specifically:

- Chapter 1 is an introduction containing a literature review and outline of the thesis content. This work is a literature review and has not been published.
- Chapter 2 focusses on the one dimensional limit of the Poisson-Nernst-Planck equation. The purpose of the chapter is to fill some gaps in previous presentation and has not been published.
- Chapter 3 is work done in collaboration with Giles Richardson, Marie-Therese Wolfram, and Jan-Frederick Pietschamn and has been published [102]. All of the numerical simulations and the derivation of the asymptotical method was done as a part of this thesis.
- Chapter 4 is work done in collaboration with Clemens Ghulke, Rüdiger Müller and Jürgen Furhman, and it is available as a preprint [55].
- Chapter 5 is a result of broad collaboration with a group led by prof. Dezső Boda at the University of Vesprem results were published in [103] and [95]. In addition the results presented in this thesis were followed in [138].
- Chapter 6 shows the optimal design approach to nanopores which is authors contribution and has not been published.

This thesis has not been submitted for a degree at any other university. It has not been submitted for an award at any other institution for any other qualification.

Abstract

In this dissertation, we focus on different aspects of modelling ion transport in confined geometries. The transport of the ions through pores was first investigated in the 19th century for cell membranes. In the last years, there has been a significant increase in research of ion transport in nanoscale devices, such as nanopores, nanowires and many more. Especially synthetic pores have the potential to be used as nanoscale diodes, switches or in DNA sequencing.

In this thesis, we investigate different modelling approaches and discuss their use and validity in various situations. The transport properties of nanoscale pores are strongly determined by the confined geometry as well as surface charges. Depending on the experimental setup considered finite size, electrostatic as well as electrochemical properties have to be resolved on various scales. This leads to a variety of models ranging from microscopic approaches, such as Molecular Dynamics, to macroscopic models like mean field theory. Since finite size effects and fluid dynamics effects should not be neglected in confined geometries various extensions of the Poisson-Nernst-Planck (PNP) system were introduced in the literature such as density functional theory or the coupling to fluid dynamics. Another challenge in ion transport modelling is the multiscale nature of the synthetic nanopores as their length scale is sometimes 10^4 times larger than their radial dimension.

In the first part of the thesis, we develop a multiscale method that investigates the asymptotic behaviour of the PNP equations for long and narrow nanopores. The significant difference in the radial and lateral length scale allows us to decouple the system and to solve the behaviour in the boundary layers close to the charged pore walls correctly. Two new asymptotic methods were developed to describe the transport problem inside the pore. This asymptotic approximation serves as the basis for the numerical solver. We investigate the quality of the approximations for a variety of pores with different computational experiments. We present comparison of the microscopic quantities such as concentrations and electric potential as well as macroscopic quantities such as current voltage characteristic of exemplary pores. In the second part of the thesis, we compare the simulations of the PNP system with Monte-Carlo methods in the case of ion-channels. We discuss the different modelling assumptions as well as the advantages of both methods. Yet again we present results of the numerical simulations and discuss regimes in which both methods are valid. In the last part, we investigate the optimal control problem for nanopores. Here

we want to modify the surface charge of a nanopore to obtain a desired behaviour, such as current-voltage characteristics or rectification behaviour. Two method are derived and implemented as a solution of stated problem.

Chapter 1

Modelling ion transport in confined geometries

The investigation of ion transport through narrow channels started in the 19^{th} century with the early works of Walter Nernst [106]. At the beginning experimental studies of the structure and the functions of the ion channels were of great interest. With the ongoing technical development and experimental finding the mathematical modelling of ion channels became more and more important, see [72; 73; 74; 63]. Roderick MacKinnon was awarded the Noble prize in chemistry for his work on the structure and operation of ion channels in 2003 [94]. The specific conductance and rectification behaviour of the biological channels initialised broad research about the structure of biological channels in general and how they can be used in the development of the microscopic electronic device, see [6]. Due to the sensibility of the biological pores, synthetic equivalents which are more robust and stable, initialised a lot of research in the last years. These synthetic nanopores are nowadays used as sensors, microscopic electric devices and in the DNA decomposition.

The transport of ionic particles in confined geometries is influenced by multiple physical phenomena such as difference in the chemical potential, drift caused by the presence of the electric field, particle-particle and particles-structure interactions as well as motion of the surrounding fluid to mention just the most significant of them. The high complexity and different time as well as space scale of the phenomena involved, lead to various modeling approaches, which provide a description at different levels of accuracy. In this chapter, we discuss the most commonly used models together with the assumptions they are based on as well as computational limitations they suffer from. We consider in particular: Molecular Dynamics (MD), Brownian Dynamics (BD), Monte Carlo methods and various mean field models.

1.1 Ion channels and nanopores

This thesis focuses on two different types of pores - ion channels and nanopores. Both of them form a passageway for ions across an impermeable membrane - the cell membrane in biological channels and a polymeric or silicon foil in case of nanopores. The physical process driving the flow through both of them is similar and in the both cases the narrowest part of the passage, that is the selectivity filter in ion channels or the narrow tip in nanopores, are only one length scale bigger than the size of the ion. This confined structure strongly influences the ionic flow. On the other hand fixed surface charge on the nanopore walls effects the movement of the ions. Due to the similar structural properties and physical processes involved, both types of pores can be described by similar mathematical models. However, there are two main differences: the inner structure and length scales. In the following we discuss the specific properties of the ion channels and nanopores.

Ion channels are proteins located in the cell membrane specialised in transporting certain type of particles inside and outside the cell. Being present in every living cell of every living organism, ion channels control many crucial functions like muscle contraction and the regulation of the blood pressure. There are two different mechanisms of transport through the cell membranes - active and passive. The active one is present in the Na+-K+pump, moving Na+ions out of the cell and K+ions into the cell. This process requires energy provided from outside as the ion is moved against the concentration gradient. The second one is the passive transport where ions are transported due to the difference in the electrochemical potential. This mechanism does not require any energy from outside and it is controlled only by the structure of the ion-channel. We focus on the second type of transport only. This two types of transport are associated with two states of the ion channels- closed and open as it is showed in the Figure 1.1. The process of changing from one state to the other is called gating and it is a complex physiological phenomena driven by the voltage among other. As this process is beyond the scope of this thesis we assume that all considered pores are in the open state. The usual radius of the channel is around few nanometers and it has a length of about $10nm$. The inner structure of the channel is made of long protein chains of complex structures that influence the flow through. The transport properties are determined by the so called selectivity filters - the very narrow inner region where aminoacids create a highly charged environment which allows only certain ions to pass.

Synthetic nanopores are a radially symmetric tunnels sculptured into polymeric and inorganic membranes such as Si_3N_4, Si, SiO_2 or polymeric membranes

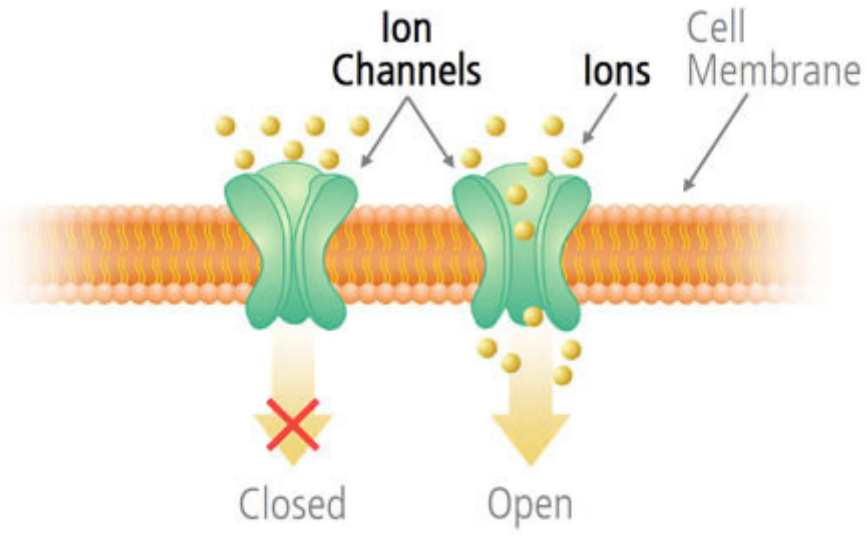

Figure 1.1: Biological ion channel inside cell membrane showing two different states of the channels - closed and open, see [10].

composed of polyethene terephthalate (PET) or polyimide Kapton. The geometry as well as the surface charge of the pore can be changed by chemical reactions. Thus pores of different shape and with desired surface charged patterns can be engineered. What is more by introducing a specific binding on the pore walls a sensor for specific species can be built. Various techniques have been developed to produce nanopores in the mentioned materials. The oldest one, the track-etching technique was first used to produce micrometer scale pore (see [81]). Here heavy ions (typically Xe, Pb Au or U) are accelerated to the kinetic energy up to 10^9eV before penetrating the foil. This creates a nanoscale size tunnel, which is subsequently modulated using wet chemical etching. Due to this process the pore has a conical shape with narrow entrance and wider exit. A similar technique can be used to obtain symmetric pores in silicon by using an etching technique from both sides of the foil. Applying the etching procedure on both sides of the foil creates a pore of conical shape and is considered to be different to the track etching. Another group of techniques is based on beams of lower energy particles such as ions or electrons. Here, a hole in a foil is drilled by the highly concentrated beam of particles of energy in the range of keV to obtain pores with the diameter as small as 3nm. The fourth class of the methods is based on breaking the end of the glass nanopipette with the laser. Here pores with a radius in the range of few nanometers [89]. Figure 1.2 shows several nanopores obtained using the etching in a PET foil. More information about nanopore production as well as the respective experimental setup can be found in

[79]. Despite the differences in shape, length and chemical composition nanopores share some common features. The can conduct constant current over time in case of an externally applied voltage on the both sides. The solid structure of the pores ensures that a single pore can be used in experiments for a long time and also allows for simple and inexpensive transport between laboratories.

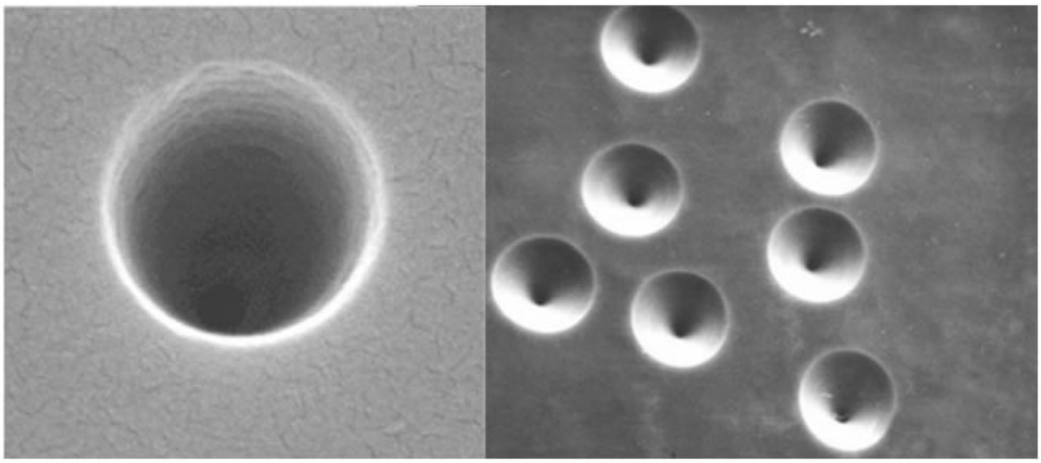

Figure 1.2: Nanopores sculptured in PET foil, see [152].

1.1.1 Experimental setup

Next we discuss a typical experimental setup which serves as the basis for the model development. In experiments, as described for example in [79], the foil or a part of the cell membrane is put into water or another solvent, such that the membrane separates two tanks. After that m salts of different valance are dissolved on both sides creating a liquid containing m ionic species and water. Next an electric potential is applied, using the electrodes located on both sides of the membrane. Due to the chemical reactions on the electrodes and the electron transfer in the electric circuit, a difference in electrochemical potential arrises and ions start to move through the membrane via the pore. This flux quickly equilibrates and the obtain current is measured when the system achieves its steady state. The size of the tanks, ensures that the concentrations of the species are constant even in the presence of continuous ionic flow. Note that the high imbalance of electrons on the diodes, leads to a double layer behaviour which reduces the value of the effective voltage. As this drop in the potential cannot be neglected, the potential difference is measured once again in the bath regions to establish the real potential acting on the pore. This potential is sometimes denoted as the reference potential. Since we do not consider the proximity of the diodes or the chemical reactions which take place in this region

we call the actual potential difference on the both sides of the pore the applied potential. Variations in the applied potential lead to different currents - the graph of the measured ionic current as a function of the applied voltage is known as the current-voltage IV curve and is a characteristic feature of a pore.

Mathematical modelling of the experiments In the experimental setup the tanks on the both sides of pores are in the lengthscale of centimetres, however all physical phenomena take place in the scale of nanometer. Therefore many models focus on the very narrow part which strongly influence the behaviour of the pore only. Scientists are interested in describing the passage of ions through the pore - either individually (in microscopic models) or by considering the respective density concentrations (in macroscopic models). The movement of the particle is influenced by the structure of the pore as well as the charged particles on the walls and other ions crossing the membrane at the same time. In what follows we consider a single open (conducing) pore, which is placed between two tanks. In that situation we distinguish between following regions - left bath, right bath and the pore connecting them.

1.2 Microscopic models

1.2.1 Molecular dynamics

Molecular dynamics simulations are based on the description of the particles on the atomic level. In these models the ions as well as all atoms that compose the membrane and the solvent are modelled as hard spheres. Their movement is described by Newton's law of motion. MD simulations can be used to describe the movement of the more complex particles, for example bi-polar water molecules or the long protein chains at the ion channels walls. Here often a coupling to the elasticity theory is considered. MD simulations describe the time evolution of the system in a completely deterministic way. The atoms movement is driven by

$$\begin{aligned} \frac{dx_i}{dt} &= u_i, \\ m_i \frac{du_i}{dt} &= F_i, \end{aligned}$$

where x_i denotes the position of the i-th particle, F_i is the associated force field, u_i stands for the velocity and m_i for the mass. List of notation can be found in the Appendix A. In the simulations all interactions between particles of the solvent and

the pore are involved leading to the high dimensional and strongly coupled system of second order ordinary differential equations. However the intuitive mathematical description as well as the possibility to use very detailed informations about the structure of the pore and the molecules involved as well as ability to cover phenomena such as chemical reactions, elastic behaviour of bigger particles and fluid-structure interactions make MD simulations a very popular tool in engineering. On the other hand, it is not clear whether the assumptions made on the microscopic interactions are valid. What is more, all simulations are restricted to a small computational domain due to the large number of the particles involved. On top of that, small time steps are required to resolve the large amount of particle interactions correctly. This makes the simulations very time consuming. The usual time scale in MD simulation are nanoseconds while capturing flow behaviour in ion-channels requires micro to milliseconds. Another disadvantage is the fact that the force fields are calibrated on small subsystems that differ significantly from the actual experimental setting. In [23] authors also point out that the non-periodic boundary conditions lead to limited usefulness of this kind of simulations for the case of different bath concentrations on both sides of the channel.

There are multiple commercial software packages available for MD simulations such as CHARM [87] or AMBER [22] that employ a variety of different force fields and the choice is left for the user. Due to the high accuracy this class of methods is often used for calibration and verification of later developed models [64; 66].

1.2.2 Brownian dynamics

A popular simplification of MD simulations are so-called Brownian Dynamics (BD) [122; 84; 37; 27]. In this model water molecules are treated implicitly. It is based on the assumption that the movement of the ions and water molecules are different - the rapid motion of the solvent and far slower collisions of ions that happen at a much lower rate. Hence the influence of water is replaced by averaged force fields acting on the charged particles. The ions are assumed to be hard spheres with the charge placed in the middle of the sphere. The naming is based on the fact that positions are calculated in a stochastic way instead of using Newton's laws of motion. In particular Langevin's equation

$$m_i \frac{du_i}{dt} = -m_i - \gamma_i u_i + R_i + F s_i,$$

is used to describe the evolution of the single particle. This Langevin's equations of motion are considered in the limit of overdamping, where the relaxation time is

much smaller than the integration time step, see [105]. Here γ_i stands for the friction coefficient, while the components involving R_i and s_i are the random and systematic forces respectively. Note that equation F stands for the Faraday's constant. The friction is coupled with the diffusion coefficient by Einstein's relation, that is

$$\gamma_i = \frac{k_B T}{m_i D_i},$$

where k_B denotes the Boltzmann constant, T the temperature and D_i stands for the diffusion coefficient.

BD is well-suited for the so-called explicit solvent models. Within these methods water (or another solvent) is approximated by a continuous force substance within the simulation domain. There are several critical issues in BD simulations. The most important is the risk of unphysical ion configurations due to the stochastic nature of the motion equations. Another problem is the inaccurate time integration of the Langevin equations which leads to differences between the prescribed model and obtained ion behaviour. In addition, the computation of the precise electrostatic forces acting on the particles is not straightforward due to the modelling complexity and could easily result in an incorrect evaluation of the motion of the ions.

All these simplifications mentioned before as well as the stochastic nature of the model makes BD less demanding in terms of computational resources than the MD simulations. This allows for simulations on time scales of microseconds which lead to more accurate computations of the ionic current cross the membrane.

1.3 Macroscopic models

1.3.1 Mean field approach

On the macroscopic level ion transport can be described by continuous densities. In our setting we are interested in the number of particles per unit volume. We denote by $n_i(x,t)$ the number of ions of type i at time t in position x. The quantity n_S stands for the number of solvent particles - in our case water. Then the evolution of the i-th ionic species can be described by the following transport equation

$$\frac{\partial n_i}{\partial t} = -\nabla \cdot \mathcal{J}_i, \tag{1.1}$$

where $\mathcal{J}_i$ denotes the flux of species i, that is rate of particle flow per unit area.

In ion channels and nanopores transport is not only driven by diffusion, but also the external electric field and the mixture of the barycentric velocities (see [43]).

We neglected the last in the following. In this case we write

$$\mathcal{J}_i = -\frac{D_i}{k_b T}\mathfrak{m}_\mathrm{i}(\vec{n})(\nabla \mu_i^e(,V)), \tag{1.2}$$

where $\vec{n}$ is the vector of ionic concentrations and D_i is the diffusion coefficient. Some authors (see [43; 42; 45; 39; 40; 41]) include also the cross-diffusion terms ($D_{i,j}$) when considering particle flow but in this thesis we narrow it and do not consider this phenomenon.

The description of the diffusion only driven transport was proposed for the first time by Adolf Eugen Fick in [49] and stated in the well known relation

$$\mathcal{J}_i = -D_i \nabla n_i.$$

Hence the flux of the i-th ionic species is proportional to the gradient of particle number. The function $\mathfrak{m}(n)$ corresponds the mobility function and μ^e denotes the electrochemical potential which is a function of the concentrations and electrical potential V. Sometimes these equations, are formulated in terms of the concentration c_i which is the given by the ratio

$$c_i(x,t) = \frac{n_i}{\sum_{i=1}^{m} n_i + n_S}$$

.

Such defined concentration describes probability distribution of particles of type i. By setting different forms of mobility and electrochemical potential in the equation (1.2) we obtain different models for the ion transport that we present in the following sections.

Equation (1.2) states that flow of the particles corresponds to the gradient of the electrochemical potential μ^e. It consists of three main components - the reference potential μ^0, the chemical potential μ^{chem} and the electric component μ^{el}, that is

$$\mu^e = \mu^0 + \mu^{chem} + \mu^{el}.$$

The reference potential μ^0 consists of all the forces that influence the flow but are not included in the chemical or electrical potential. For example particle-particle interactions or hard sphere interactions. The electrochemical potential μ^{el} describes the influence of the electric potential on the movement of the particles. The chemical part of the potential - μ^{chem} denotes the chemical forces driving the flow. It includes

diffusion as well. In the next sections we discuss the self consistent coupling of (1.2) to the Poisson-Boltzman equation to model the ion transport through the nanopores and ion-channels. We present different models which arise due to differently chosen electro-chemical potential μ^e, mobility function $\mathfrak{m}_i(n)$ as well as surrounding fluid treatment. In the following we discuss a family of models starting with the most general the Dreyer-Guhlke-Landstorfer-Müller (DGML). Then we present several modifications, which are based on different simplifications, such as Bikerman model and the well known Poisson-Nernst-Planck equations.

1.3.2 Mean field model and the solvation effect

Solvation occurs when ionised particles are dissolved in a bipolar solvent. In our case, the bipolar nature of that water molecules results in a solvent shell around charged ions as it is shown in Figure 1.3.

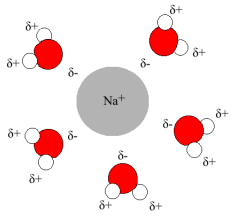

Figure 1.3: Solvent shell formed around a sodium ion. Water particles are facing the positively charged particles with the negative side.

The motion of the ions as well as the solvent particles causes constant exchange of water particles in the shell. However the effective structure of the ion with the solvent shell, forming a bigger particle remains the same. The influence of this phenomenon was studied in [108] and in the context of ion channels in [114; 7].

This effect can be included in the mean field models via solvent molecules and size exclusion such as in DGML (1.12)–(1.13), Bikerman (1.14) and the nPNP (1.19a)–(1.19b). The modelling of the solvation effect results in the following changes. First of all, it prevents overcrowding of the ions in the proximity of the charged walls. The PNP model is known to overestimate the ionic concentration close to the highly charged nanopore walls which leads to unphysical behaviour. Including the solvation effect might be a remedy for this effect yet very little is known about the solvation shells in terms of its size and behaviour in the presence of an applied potential. In Chapter 4 we discuss the influence of the solvation effect while developing new asymptotic models for ionic flows. First insight about the influence of the solva-

tion effect are shown in Chapter 4, but a further and much deeper analysis of this phenomenon is necessary for the full understanding of the problem.

1.3.3 Coupling with Poisson-Boltzman theory

The electric potential μ^{el} describes the interactions between the charged ionic species and the surrounding electric field. The electric potential is described by the Poisson-Boltzmann theory, gives $\mu^{el} = z_i e_0 V$, where e_0 is the elementary charge, z_i the valence of the ion i and V is the electric potential. To obtain a closed system of equations we couple the transport equations (1.1)–(1.2) with the Poisson's equation, that is

$$\nabla \cdot (\mathcal{E}) = \frac{n^F}{\epsilon_r \epsilon_0}, \text{ with } n^F = e_0 \sum_{i=1}^{m} z_i n_i. \tag{1.3}$$

Here $\mathcal{E}$ is the electric field, n^F denotes the free charge density, ϵ_r is the relative dielectric constant of the solvent and ϵ_0 stands for the permeability of the free space. We assume that the influence from the change in the magnetic field can be neglected. Therefore Faraday's law gives

$$\nabla V = -\mathcal{E}. \tag{1.4}$$

Then (1.3) reads as

$$\epsilon_r \epsilon_0 \nabla \cdot (\nabla V) = -e_0 \sum_{i=1}^{m} z_i n_i. \tag{1.5}$$

Equation (1.5) describes the the effect of the mobile and permanent charges on the electric field consistently. Together with the transport equation, equations (1.1)–(1.2) and explicit formula for the electrochemical potential μ^e we obtain a closed system of $m+1$ equations for $m+2$ unknowns, in particular the species and solvent particle numbers n_i and the electric potential V. To obtain a closed system of equations we need to derive a relation between the solvent and other species particle numbers. The most general form of discussed model reads as

$$\epsilon_r \epsilon_0 \nabla \cdot (\nabla V) = -e_0 \sum_{i=1}^{m} z_i n_i, \tag{1.6a}$$

$$\mathcal{J}_i = -\frac{D_i}{k_B T} \mathfrak{m}_\mathrm{i}(\vec{n})(\nabla \mu_i^e(\vec{n}, V)) \quad \text{for } i = 1, ..., m, \tag{1.6b}$$

$$\frac{\partial n_i}{\partial t} = -\nabla \cdot \mathcal{J}_i \quad \text{for } i = 1, ..., m. \tag{1.6c}$$

As the relative permeability ϵ_r of the membrane is far lower than the one of the

solvent we assume that the electric field inside the membrane is negligible. This geometrical assumptions ensures that

$$\text{supp}\{n_i(x,y,z,t)\} = \text{supp}\{V(x,y,z,t)\}.$$

Figure 1.4 shows a simplified geometry of the problem considered. Note that it is not in scale and that it omits the variation of the pores radius.

System (1.6a)-(1.6c) is considered on the domain Ω and has to be supplemented with boundary conditions. We assume that the pore is radially symmetric, that is

$$\Omega_P = \{(x,y,z) : 0 < x < L, 0 \leq \sqrt{y^2+z^2} \leq R(x)\},$$

where L denotes the length of the pore and $R(x)$ its shape function. On both sides of the channel the so called bath regions are attached. Their size and shape varies [30; 115] but we assume that

$$\begin{aligned}\Omega_B =& \{(x,y,z) : -L_B \leq x \leq 0, 0 \leq \sqrt{y^2+z^2} \leq R_B(x)\} \cup \\ & \{(x,y,z) : L \leq x \leq L_B, 0 \leq \sqrt{y^2+z^2} \leq R_B(x)\}.\end{aligned}$$

The baths correspond to the in and outside of the cell in biological channels and to the tanks with solvent in case of nanopores. The full computational domain is denoted by $\Omega = \Omega_B \cup \Omega_P$ and shown in Figure 1.4 .

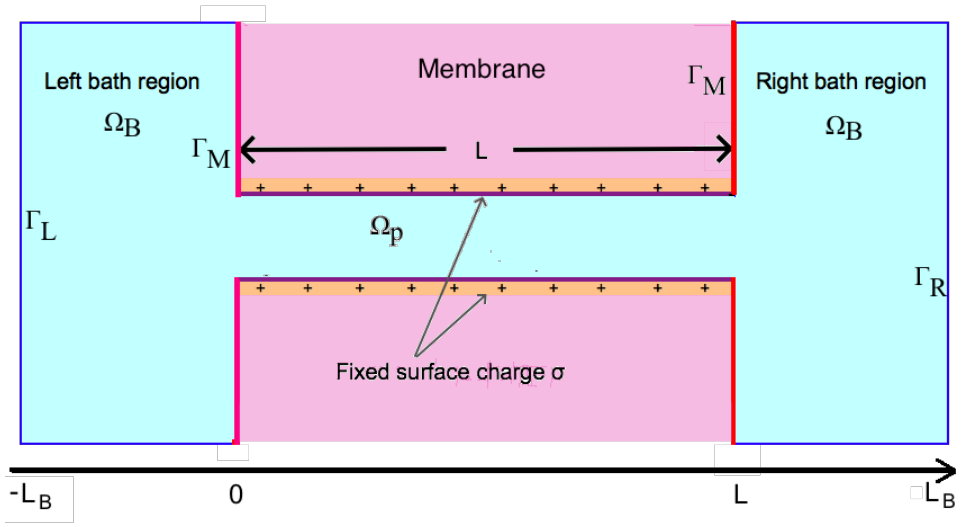

Figure 1.4: Sketch of the Ω as well as boundaries Γ_L, Γ_R and Γ_M .

Boundary conditions The fixed surface charge at the nanopore walls (see [134; 61; 150; 47]) corresponds to a Neumann boundary condition of the form

$$\frac{\sigma}{\epsilon_r} = -\nabla V \cdot N|_{\Gamma_N},$$

where N denoted the outer unit normal vector. The Neumann boundary condition is applied on $\Gamma_N = \{(x, y, z) \in \Omega_p, \sqrt{y^2 + z^2} = R(x)\}$. We assume no flux boundary conditions of the ionic species, that is

$$\mathcal{J}_i \cdot N|_{\Gamma_N} = 0 \quad \text{for } i = 1, ..., m.$$

In the bath regions Ω_B have two types of boundaries. The one facing the membrane defined as

$$\Gamma_M = \{(x, y, z) \in \Omega_B, x = 0\} \cup \{(x, y, z) \in \Omega_B, x = L\},$$

Here we assume that no particles cross the membrane and that there is no surface charge. Therefore

$$\begin{aligned} \mathcal{J}_i \cdot N|_{\Gamma_M} &= 0 \quad \text{for } i = 1, ..., m, \\ \nabla V \cdot N|_{\Gamma_M} &= 0. \end{aligned}$$

In experiments the applied electric potential is generated by two electrodes placed at least few micro-meters away from the membrane. Hence we set $V|_{\Gamma_L} = V_L = 0$ on the boundary

$$\Gamma_L = \{(x, y, z) \in \Omega_B, x = -L_B\} \cup \{(x, y, z) \in \Omega_B, \sqrt{y^2 + z^2} = R_B(x)\},$$

On the right side we set the applied potential $V|_{\Gamma_R} = V_{appl}$ where Γ_R is defined similarly as Γ_L. Since the ionic flow through the pore is of several orders of magnitude smaller then a total number of ions in the baths we assume that the concentrations on the boundary of our domain are constant. Therefore we choose the following Dirichlet boundary conditions

$$n_i|_{\Gamma_L} = n_{B,i} \quad \text{for } i = 1, ..., m,$$

where $n_{B,i}$ is the bath particle number per unit volume of the species i. Furthermore, we assume that charge neutrality holds in the bath regions, that is

$$\sum_i^m z_i n_i|_{\Gamma_L} = \sum_i^m z_i n_i|_{\Gamma_R} = 0.$$

The mean field system in the steady state As the system calibrates after milliseconds we consider its steady state only. That yields

$$\epsilon_r \epsilon_0 \nabla \cdot (\nabla V) = -e_0 \sum_{i=1}^m z_i n_i, \tag{1.7a}$$

$$\mathcal{J}_i = -\frac{D_i}{k_B T} \mathfrak{m}_i(\vec{n})(\nabla \mu_i^e) \quad \text{for } i = 1, ..., m, \tag{1.7b}$$

$$0 = \nabla \cdot \mathcal{J}_i \quad \text{for } i = 1, ..., m, \tag{1.7c}$$

together with

$$\mathcal{J}_i \cdot N|_{\Gamma_B} = 0 \quad \text{for } i = 1, ..., m \text{ and } \nabla V \cdot N|_{\Gamma_B} = 0, \tag{1.8a}$$

$$\mathcal{J}_i \cdot N|_{\Gamma_N} = 0 \quad \text{for } i = 1, ..., m \text{ and } \nabla V \cdot N|_{\Gamma_N} = \frac{\sigma}{\epsilon_r}, \tag{1.8b}$$

$$n_i = n_{B,i}|_{\Gamma_L \cup \Gamma_R} \quad \text{for } i = 1, ..., m \text{ and } V|_{\Gamma_L} = 0, V|_{\Gamma_R} = V_{appl}, \tag{1.8c}$$

$$\mathcal{J}_i \cdot N|_{\Gamma_M} = 0 \quad \text{for } i = 1, ..., m \text{ and } \nabla V \cdot N|_{\Gamma_M} = 0. \tag{1.8d}$$

1.3.4 Mean field models for ion transport in nanoscale pores

In the previous section we described a general setup for modelling the ionic transport through confined geometries. We discussed the geometry, boundary conditions and the coupling of the mass balance equation with the Poisson-Boltzman equation leading to a closed system of the partial differential equations. In the following we present the hierarchy of mean field which differ in the following way

1. Modelling of the electrochemical potential

2. Mobility: different mobility models have been discussed in the literature. In the majority of the models the mobility is assumed to be linear, but also nonlinear versions such as degenerate or porous medium type diffusion have been considered, see [91].

3. Solvent treatment: different assumptions on the surrounding fluid and its interactions with the ions have been considered in the models. If electrochemical effects are dominating the dynamics of the system, then the velocity of the fluid

can be set to $\vec{u} = 0$. If this is not the case the solvent velocity can be included via coupling to an additional equation, such as Navier-Stokes equation.

In the following section we describe different mean fields models by considering different components of the potential and mobility functions. In the entire thesis we consider isothermal case, that is $T = \text{const}$. We present the models as a complete systems of equations but the summary in terms of mobility and potential functions can be found in table 1.1.

1.3.5 Dreyer-Guhlke-Landstorfer-Müller model

The DGLM model was derived from general framework of electro-thermodynamics in [43; 42; 45]. A more detailed analytical study, as well as an existence proof of solutions can be found in [39; 40; 41]. It is based on the assumption that the masses and the volumes of the particles and the solvent satisfy

$$\frac{m_i}{v_i} = \frac{m_s}{v_s} \text{ for } i = 1, 2, ..., m, \tag{1.9}$$

where m_i stands for the mass of the species i and v_i for its specific volume. This implies that the total mass density $\sum_{i=1}^{m} m_i n_i + m_S n_S$, is constant. Then, the general constitutive equations read

$$\mathcal{J}_i = -D_i \tfrac{m_i n_i}{k_B T} \nabla \Big(\mu_i^{chem} - \tfrac{m_i}{m_S} \mu_S^{chem} + z_\beta e_0 V \Big) \qquad \text{for } i = 1, 2, ..., m. \tag{1.10}$$

In the incompressible setting the number densities have to satisfy the constraint

$$1 = \sum_{i=1}^{m} v_i n_i + n_S v_S,$$

which defines an upper bound for the number densities. The chemical potentials μ_i are defined as

$$\mu_i^{chem} = \mu_i^0 + k_B T \ln(c_i), \tag{1.11}$$

where μ_i^0 is the reference potential, which depends in general on the temperature and we assume it to be constant. Thus using the relation (1.9), the (effective) electrochemical potentials are

$$\mu_i^{\mathrm{e}} = \widetilde{\mu}_i^0 + k_B T \big(\ln(c_i) - \tfrac{m_i}{m_S} \ln(c_S) \big) + z_i e_0 V, \tag{1.12}$$

where $\widetilde{\mu}_i^0$ denotes the reference chemical potentials of ion and solvent.

Using of the chemical potential (1.11) into the mass fluxes (1.10) yields the explicit expression for the fluxes, that is

$$\begin{aligned}\mathcal{J}_i = -D_i m_i \Bigg(& \nabla n_i + n_i \frac{z_i e}{k_B T} \nabla V \\ & + \frac{n_i}{n_S} \Big[- \frac{m_i}{m_S} \nabla n_S - \frac{n_S}{n} \Big(1 - \frac{m_i}{m_S} \Big) \nabla n \Big] \Bigg),\end{aligned} \tag{1.13}$$

where the last term denotes the gradient of the total number of particles ($n = \sum_1^m n_i$). This formula of the flux represents different physical phenomena. The first term corresponds to the diffusion due to the concentration gradients, the second a drift because of the applied electrical field. The next terms describe solvent-ion interaction, term provides a correction for the different size of the constituents, while the last term represents the coupling of elastic effects and diffusion.

This model considers particles of different masses and volumes which is crucial for the solvation effect discussed in section 1.3.2. In the next sections we described simplifications of the models leading to more basic but commonly used models.

1.3.6 Bikerman model

The Bikerman model was introduced in [9] and can be considered as a simplification of the above mentioned DGML model, where masses and volumes of all of the ionic species are equal, i.e.

$$m_S = m_i \text{ and } v_i = v_S \text{ for } i = 1, ...m.$$

Then (1.12) simplifies to

$$\mu_i^{\mathrm{e}} = \widetilde{\mu}_i^0 + k_B T \big(\ln(c_i) - \ln(c_S) \big) + z_i e_0 V. \tag{1.14}$$

Due to the fact that all the particles in the Bikerman model have the same size it can be seen as a size of a lattice on which the particles are moving. The total number density is given by the lattice and is constant, which leads to

$$c_S = 1 - \sum_{\alpha=1}^{m} c_i = 1 - \rho.$$

Note that the maximal charge density has an upper bound.

1.3.7 The Poisson-Nernst-Planck and the nonlinear Poisson-Nernst-Planck equations

A usual assumption of the particle transport is that the concentrations of the ions c_i are smaller then the concentrations of the solvent c_S, namely $c_S \gg c_i$. Applying this relation to the equation (1.13) leads to the oldest and well established model, the so called Poisson-Nernst-Planck (PNP) equations [108]. That reads

$$\mathcal{J}_i = -\frac{D_i}{k_B T} c_i \nabla \mu_i^{\mathrm{e}}, \tag{1.15a}$$

$$\mu_i^{\mathrm{e}} = \widetilde{\mu}_i^0 + k_B T\big(\ln(c_i)\big) + z_i e_0 V. \tag{1.15b}$$

together with boundary conditions

$$\mathcal{J}_i \cdot N|_{\Gamma_B} = 0 \quad \text{for } i = 1, ..., m \text{ and } \nabla V \cdot N|_{\Gamma_B} = 0, \tag{1.16a}$$

$$\mathcal{J}_i \cdot N|_{\Gamma_N} = 0 \quad \text{for } i = 1, ..., m \text{ and } \nabla V \cdot N|_{\Gamma_N} = \frac{\sigma}{\epsilon_r}, \tag{1.16b}$$

$$c_i = c_{B,i}|_{\Gamma_L \cup \Gamma_R} \quad \text{for } i = 1, ..., m \text{ and } V|_{\Gamma_L} = 0, V|_{\Gamma_R} = V_{appl}, \tag{1.16c}$$

$$\mathcal{J}_i \cdot N|_{\Gamma_M} = 0 \quad \text{for } i = 1, ..., m \text{ and } \nabla V \cdot N|_{\Gamma_M} = 0. \tag{1.16d}$$

The PNP system has been used to describe the flux of carriers in semiconductor crystals [98; 99; 101]. Note that the PNP equations are known as drift-difussion equations (DDE) in the semiconductor community. The respective current flow is a few orders of magnitudes larger than nanopores, the same holds for the physical size of the semiconductor devices. Semiconductors have simpler geometry, than the long and thin pores and multiscale effects as in nanopores are not so dominant. The DDE have been used successfully to solve optimal design and parameter identification problems for semiconductor devices [147; 116] and even led to an asymptotic solutions of the problem [100].

Entropy formulation and gradient flow structure In the steady state the continuity relation (1.7b)–(1.7c) can be written as

$$0 = \nabla \cdot (\frac{D_i}{k_B T} c_i \nabla \mu_i), \tag{1.17}$$

where μ_i denotes the electrochemical potential given by

$$\mu_i = k_B T \log c_i + z_i e V. \tag{1.18}$$

This formulation is commonly used in the physics community, see for example [12; 14; 64]. It is related to a gradient flow structure of the PDE system with respect to the Wasserstein metric on the L^2 space of the entropy

$$E(c_1, .., c_m) = \sum_{i=1}^{m} \int c_i \log c_i + c_i z_i e V(c_1, .., c_m),$$

leads to a formulation of the continuity equation

$$\nabla \mu_i := \frac{\delta E}{\delta c_i}.$$

Nonlinear Poisson-Nernst-Planck model

A nonlinear version of the Poisson-Nernst-Planck model introduced in [26]. Here a nonlinear mobility model, was formally derived from a microscopic lattice based particle approach which included volume exclusion. That leads to a drift-diffusion system in which unphysical high concentrations of the particles are not possible due size exclusion which leads to an upper bound on the total concentration. The nonlinear mobility is given by $\mathfrak{m}(\vec{n}) = (1-\rho)c_i$ which results in a strong size exclusion effect. The system reads

$$\mathcal{J}_i = -\frac{D_i}{k_B T}(1-\rho) c_i \nabla \mu_i^{\mathrm{e}}, \tag{1.19a}$$

$$\mu_i^{\mathrm{e}} = \widetilde{\mu}_i^0 + k_B T\big(\ln(c_i) - \ln(c_S)\big) + z_i e_0 V. \tag{1.19b}$$

Here the term $(1-\rho) = 1 - \sum_{i=1}^{m} c_i$ corresponds to the freely available space. The lower concentrations and lower mobility than the ones observed in the classic PNP model leads to lower flow. Note that the (1.19b) corresponds to the Bikerman model, which used a linear mobility. The drift- diffusion equation is combined with the Poisson-Boltzmann equation (1.5). This system is also known as the nonlinear PNP (nPNP from now on).

Summary of the models

All the models presented above can be written in terms of an electrochemical potential and a mobility functions. The table 1.1 states the respective choices for the models.

Name of the model	$\mathfrak{m}_i(\vec{c})$	μ_i
DGLM (1.10)–(1.12)	c_i	$k_B T\big(\ln(c_i) - \frac{m_i}{m_S}\ln(c_S)\big) + ez_iV$
Bikerman (1.14)	c_i	$k_b T \log\frac{c_i}{(1-\rho)} + ez_iV$
nPNP (1.19b)–(1.19a)	$(1-\rho)c_i$	$\mathrm{k}_b T \log\frac{c_i}{(1-\rho)} + ez_iV$
PNP (1.17)- (1.18)	c_i	$k_b T \log c_i + ez_iV$

Table 1.1: Comparison of the different mean field models.

1.3.8 Related mean field approaches

Different modifications of the mean field models can be found in the literature. Some of them include phenomena such as: particle particle interactions, nonlinear diffusion and solvent movement.

Poisson-Nernst-Planck coupled to the Navier-Stokes model.

The classical Nernst-Planck equation involves the motion of the fluid as one of the components of the ionic flux. It is a very strong assumption that the flow of the water that is surrounding the ions has no influence on the movement of the charged particles. For that reasons the Navier-Stokes equation has been coupled with PNP system to obtain Navier-Stokes-Poisson-Nernst-Plank system, see [124]. Here (1.6a) – (1.6c) is coupled to

$$\rho^F(\partial_t\vec{u} + (\vec{u}\circ\nabla)\vec{u}) - \mu\Delta\vec{u} + \nabla p = -n^F\nabla V, \tag{1.20a}$$

$$\mathrm{div}(u) = 0, \tag{1.20b}$$

where p stands for the pressure and n^F is the charge density and ρ^F fluid density. In [124] existence of solutions as well as the numerical discretisation was showed. The numerical scheme proposed in [119] provides an efficient method for finite element solutions of the system at hand. In [53; 44; 50] a coupling of the PNP model to the Stokes equation have been proposed in the context of the semiconductor device modeling.

Poisson-Nernst-Planck with nonlinear diffusion term

In [91] the authors analysed generalisation of the PNP equation with the porous medium type diffusion. For a given number $k \geq 1$ and two ionic species with

concentration denoted by n and p the system is given by

$$\operatorname{div}(\nabla V) = n - p, \tag{1.21a}$$

$$\partial_t p = \Delta p^k + \operatorname{div}(p \nabla V), \tag{1.21b}$$

$$\partial_t n = \Delta n^k + \operatorname{div}(n \nabla V), \tag{1.21c}$$

for $t \geq 0$ and $x \in \mathbb{R}^d$ where $d \geq 3$. This system can be interpreted as a gradient flow with respect to the Wasserstein distance. The authors prove existence of the solutions in the case of $k = 1$ and $k > 1$.

1.4 Multiscale models

Multiscale methods have been used to resolve transport process at different scales. They allow to include small scale relations, such as particle-particle interactions, which are neglected when in mean field models. At the same time other length scales resolved using the mean field models, allowing for higher computational efficiency. In this thesis we will discuss two of these methods - a Local Equilibrium Monte Carlo method and Density Function Theory. Further information on different scale approaches can be found in for example in [56; 146; 2; 3].

1.4.1 Monte Carlo methods

Monte Carlo simulations have beed used very recently in ion channel simulations, see [12; 60; 46]. The LEMC+NP approach, see [12; 14; 64; 21], combines the continuity equations with stochastic computation of the potential equilibrium. It combines the continuity equations of charged particles together with stochastic computations of the potential in equilibrium. It assumes that the system is locally in a steady state and that fluid can be neglected.

The LEMC+NP method is used mostly among chemical engineers and is based on the NP equation, that reads

$$\mathcal{J}_i = -\frac{D_i}{k_b T} c_i \nabla \mu_i. \tag{1.22}$$

Yet again the electrochemical μ_i potential is composed of the chemical and electrical part

$$\mu_i = \mu_i^{chem} + z_i e V,$$

that as in the case of the PNP combines the chemical potential (μ_i^{chem}) with the electrical potential $z_i e V$. The reason for this formulation is that in experimental

setups these two cannot be separated. Note that the equation (1.2) is obtained from (1.22) by neglecting fluid velocity and setting

$$\mu_i^{chem} = \mu^0 + k_B T \ln(c_i).$$

where μ^0 is constant. The coupling between V and μ_i is provided by the Monte Carlo method. In early works the MC method was for a system in global equilibrium, that means the μ_i was constant in the whole domain and no external applied potential was applied. The novelty of the LEMC method is to divide the computational domain into small subvolumes and then assume that the electrochemical potential is constant in these subdomains. Due to the MC coupling, the LEMC+NP method is able to track the movement of every single particle and include the size of single charge ions. That gives better insight in the trajectories of other methods.

The LEMC+NP method combines two different modelling levels - the full particle models and the mean field approach. For that reason, it is particularly interesting in terms of comparison for both of the modelling types. Unfortunately due to its stochastic nature it is computationally demanding. However it can be used to describe the positions of the particles including the particle-particle interactions and volume exclusion phenomena in small geometries such as ion channel.

The results prepared using this method and the comparison with other methods are presented in Chapter 5.

1.4.2 Density Functional Theory

The idea of modelling multi-particles systems with density functionals was investigated for fluid dynamics by Walter Kohn and Pierre Hohenberg (see [76]) in the second half of the 20$^{\text{th}}$ century. They developed a computationally feasible approach to deal with systems containing many particles. These results were used for the PNP model by Dirk Gillespie to include size exclusion effects and local electrostatic interactions, see [59; 75].

The main idea is to introduce an additional potential to μ_i which includes an additional potential arising from the hard-sphere interactions, that is

$$\mu_i = \mu_i^{HS} + \mu_i^e.$$

Note that the computation of the μ_i^{HS} is costly and its extension into higher dimensions is not clear as the model was introduced in 1D only. The additional potential μ_i^{HS} introduces the effect of particle - particle interactions as every charged particle creates an electric field that influences other particle in the vicinity. The computa-

tion of this additional term involves the computations of high dimensional nonlinear integrals, which is based on nonlocal approximations and though expensive.

1.5 Comparison of the methods

In this chapter we presented modelling approaches which have been proposed in the literature to describe ion transport through ion channels and nanopores. Because of the different modelling assumptions they describe the transport at different orders of accuracy and scales. This leads to different levels of numerical complexity and therefore computational resources. Choosing the correct level of accuracy is a challenging task which was discussed in more details in [109].

The most in depth description is Molecular Dynamics. It is a suitable choice to model charged particles transport over short time scales and small computational domains. It allows to simulate each particle's trajectory, which at the same time is also the biggest disadvantage of the method. For every single particle Newton's laws of motion need to be integrated using a time stepping method with strong restrictions on the time steps. This limitation reduces the time which can be simulated significantly. Furthermore, with every time step the numerical error accumulates which might lead to false results [92]. In case of low ion concentrations more water molecules need to be considered, leading to further computational limitations. Nevertheless, the high microscopic accuracy and ability to trace all of the particles make MD simulations a proper tool to investigate some of the small biological ion channels over short time scales. Although, the method is being constantly developed [83; 111] its usefulness for the investigation of longer nanopores is still limited due to the high computational costs and limited time range.

Using stochastic approaches to overcome the shortcomings observed in the Molecular Dynamics models was the idea behind development of Brownian Dynamics and Monte Carlo methods. Both methods, as statistical based methods, require multiple runs and adequate averaging methods to obtain trustworthy results hence both method are computationally expensive.

On the other hand, BD produces very accurate trajectories of charged particles over much larger time horizon than the MD simulations mainly because of the treatment of water particles. Due to these assumptions larger times steps and computational domains are allowed.

Mean field approaches are based on a significant simplifications of the physical problem. By considering the concentration instead of the trajectories of the particles we lose certain amount of the information about the problem. Different

mean field models count for specific aspects such as different particle masses and volumes or the macroscopic description of the surrounding fluid flow. By concentrating on averaged effects present in mean field only the methods are less accurate than MD or BD. A common feature of all mean-field approaches introduced in this chapter is their computational feasibility. Different methods have been developed to simulate these systems of partial differential equations effectively. The computational complexity highly increases in case of additional DFT potentials, but it is still significantly lower then for MD and BD simulations. Also the analytical results available make mean field models amendable, especially in the context of inverse problems, shape optimisation or optimal design.

Combining stochastic integration methods together with the mean field approach leads to a method that has an interesting balance between accuracy and computational complexity. The LEMC+NP method posses some of the disadvantages of the stochastic methods especially in larger computational domains. Hence, it is limited to shorter pores such as the ones in silicon nitride membranes [71].

Chapter 2

Analysis of the one-dimensional Poisson-Nernst-Planck equation

In this chapter, we derive a one-dimensional area averaged limit of the stationary Poisson-Nernst-Planck equation as it was described in [123]. We begin with recalling an existence result for the stationary PNP equation (1.6a)-(1.6c) which in case of the semiconductor devices was shown in [98]. The steady state is considered in mean fields models for nanopores due to the fast equilibration of the system. In the case of the ion channels that assumption might not always be fulfilled as the complex gating mechanism may change the shape and the inner structure of the channel (see [28; 68; 148]).

Theorem 1 (Existence of the solution of the PNP system [98])**.** *Let* $\sigma \in H^{1/2}(\Gamma_N) \cap L^\infty(\Gamma_N)$*, the applied potential* $V_{app} \in H^{1/2}(\Gamma_R \cup \Gamma_L) \cap L^\infty(\Gamma_R \cup \Gamma_L)$ *and the boundary concentrations* $c_i|_{\Gamma_R} \in H^{1/2}(\Gamma_R \cup \Gamma_L) \cap L^\infty(\Gamma_R \cup \Gamma_L)$*. Then there exists a solution* $(c_1, .., c_m, V) \in \Big(H^1(\Omega) \cap L^\infty(\Omega)\Big)^{m+1}$ *to* (1.7a)*,* (1.7c)*,* (1.15a)-(1.15b) *together with the boundary conditions* (1.16a)-(1.16d)*.*

The derivation of the 1D Area Averaged model is valid for long radially symmetric pores. It is obtained by writing the PNP system in radially symmetric coordinates and passing to the limit $R \to 0$, where r stands for the radius of the pore. In the second part of the chapter, we discuss the existence and uniqueness of this 1D area averaged PNP system. The proof follows the lines of the existence results presented in [98] for the stationary drift - diffusion equations. Due to the averaging we need to adapt the argument since the mobility, diffusivity and source term depend on the area function. In the last part of the chapter, we present the existence proof for the respective 1D area averaged nPNP model.

2.1 Derivation of the one dimensional limit of the PNP model

Since nanopores and ion channels have a small aspect ratio a dimensional reduction is often used in the literature. In these models the influence of the surface charge is averaged over the pore area, see [30; 32; 143]. In this section, we present the derivation based on the H^1 convergence in case of the rotationally symmetric pores with small aspect ratio and the surface charge located on the inner pore walls. The argument is based on the statement of Theorem 1, in fact we use the regularity of the solutions of the steady-state PNP equation. In the following, we assume that length of the pore is much bigger than its radius and introduce the scaling $x^* = \bar{L}x$ and $r^* = \bar{R}r$. We denote unscaled values with the superscript * and scaling factors of the quantities by $\bar{\cdot}$. Then the PNP system in cylindrical coordinates in the domain $\Omega = \{[0, L] \times Q\}$, where $Q = \{r\cos(\theta), r\sin(\theta) | 0 < r < R \text{ and } \theta \in [0, 2\pi)\}$ and $\sqrt{(y)^2 + (z)^2} \leq R$. Here $R := \frac{R^*}{\bar{R}}$ corresponds to a scaled radius of the pore and $L = \frac{L^*}{\bar{L}}$ to its scaled length.

Let $V(x, r, \theta) = V(x, r, \theta)$. Then the Poisson-Boltzmann equation reads as

$$-\lambda_D \Big(\bar{L}^{-2} \partial_{xx} V + \bar{R}^{-2} \frac{1}{r} \partial_r (r \partial_r V) \Big) = \sum_{i=1}^{m} z_i c_i, \tag{2.1}$$

where the terms associated with ∂_θ were omitted due to radial symmetry. The scaling parameter $\lambda_D = \frac{\bar{V} \epsilon_r \epsilon_0}{\bar{c} e}$ is also known as the Debye length and relates the typical voltage $\bar{V}$ to to typical concentration $\bar{c}$. The corresponding scaled boundary condition reads

$$\partial_r V = \frac{\bar{\sigma} \bar{R}}{\epsilon_r \epsilon_0 \bar{V}} \sigma = \bar{\kappa}(\bar{R}) \sigma.$$

Using the techniques described in [123, Chapter 4] we multiply the equation (2.1) with a test function $\psi \in H_0^1(\Omega)$ to obtain a weak formulation given by

$$-\lambda_D \int_0^L \int_Q \Big(\bar{L}^{-2} \partial_{xx} V + \bar{R}^{-2} \frac{1}{r} \partial_r (r \partial_r V) \Big) \psi r dx dr d\theta = \int_0^L \int_Q \sum_{i=1}^{m} z_i c_i \psi r dx dr d\theta.$$

Integrating the left hand side of the equation by parts we obtain

$$\begin{aligned}
LHS =&\lambda_D \bar{L}^{-2} \int_0^L \int_Q \partial_x V \partial_x \psi r dx dr d\theta + \lambda_D \bar{R}^{-2} \int_0^L \int_Q r \partial_r V \partial_r \psi dx dr d\theta \\
&-\lambda_D \bar{\kappa} \int_0^L \int_0^{2\pi} r \partial_r V \psi dx d\theta \big|_{r=0}^{r=R} \\
=&\lambda_D \bar{L}^{-2} \int_0^L \int_Q \partial_x V \partial_x \psi r dx dr d\theta + \lambda_D \bar{R}^{-2} \int_0^L \int_Q r \partial_r V \partial \psi dx dr d\theta \\
&-\lambda_D \bar{\kappa} \int_0^L \int_0^{2\pi} R \sigma \psi d\theta dx.
\end{aligned}$$

Our goal is to pass with $\bar{R} \to 0$ we assume that $\lambda_D >> \bar{R}$. What is more we assume that $\bar{\kappa}\lambda_D < C$ which assumption is further discussed in next chapter (using the values mentioned in table A.1 leads to $\bar{\kappa}\lambda_D := \kappa \approx \mathcal{O}(1)$). That provides a following uniform estimate

$$\frac{\lambda_D}{L^2} \int_0^L \int_Q (\partial_x V \partial_x \psi + \Delta^{-2} \partial_r V \partial_r \psi) r dx dr d\theta \leq C(\Omega, A) \Big[\sum_{i=1}^m |z_i| \|c_i\|_{L^\infty} + \|\sigma\|_{L^\infty} \Big],$$

where $\Delta = \frac{\bar{R}}{\bar{L}} << 1$. Using the L^∞ bound on c_i and σ we obtain

$$\int_0^L \int_Q (\partial_x V \partial_x \psi) r \leq K_1 \text{ and } \int_0^L \int_Q (\partial_r V \partial_r \psi) r \leq \Delta^2 K_2.$$

By taking $\psi = V$ we conclude with the uniform estimate $\partial_r V \leq \Delta^2 K_2$. In the limit $\Delta \to 0$ we obtain that $V(x, r, \theta) \rightharpoonup V^0(x)$ along a subsequence in $H^1(Q)$. Setting $\psi = \psi(x)$ we can conclude with the convergence of the left side

$$\begin{aligned}
&\gamma \int_0^L \int_Q (\partial_x V \partial_x \psi + \Delta^{-2} \partial_r V \partial_r \psi) r dx dr d\theta \to \\
&\gamma \int_0^L \partial_x V^0 \partial_x \psi \Big(\int_Q r dr d\theta \Big) dx = \gamma \int_0^L \pi R^2 \partial_x V^0 \partial_x \psi dx,
\end{aligned}$$

where $\gamma = \frac{\lambda_D}{L^2}$. The right hand side convergence reads

$$\int_0^L \int_Q \psi \sum_{i=1}^m z_i c_i r dx dr d\theta + \kappa \int_0^L \int_0^{2\pi} \sigma \psi R dx d\theta \to$$
$$\int_0^L \psi \sum_{i=1}^m z_i c_i^0 \Big(\int_Q r dr d\theta \Big) dx + \kappa R 2\pi \int_0^L \sigma \psi dx =$$
$$\int_0^L \pi R^2 \partial_x \sum_{i=1}^m z_i c_i^0 \psi dx + \kappa R 2\pi \int_0^L \sigma \psi dx.$$

Setting $A(x) = \pi R^2$ and $\partial A(x) = 2\pi R(x)$ denote the area and circumference of the radially symmetric pore respectively. Hence we obtain

$$-\gamma \partial_x (A \partial_x V) = A \sum_{i=1}^m z_i c_i + \kappa \partial A \sigma.$$

A similar argument can be used for the continuity equation which leads to the one-dimensional PNP system

$$-\gamma \partial_x \Big(A \partial_x V \Big) = A \sum_{i=1}^m z_i c_i + \kappa \partial A \sigma, \tag{2.2a}$$
$$D_i \partial_x \Big(A [\partial_x c_i + z_i c_i \beta \partial_x V] \Big) = 0 \quad \text{for } i = 1, \dots, m, \tag{2.2b}$$

with the boundary conditions given by

$$V(0) = 0, \quad V(L) = V_D \quad \text{and} \quad c_i(0) = c_{i,B} = c_i(L).$$

A similar procedure can be applied to obtain 1D Area Averaged version of the Bikerman model and nPNP, see table 1.1. The only difference between them is the convergence of the continuity equations which is straightforward.

2.2 One dimensional PNP system

In this section we show the existence of the the system 1dpnp describing the relation between the electric potential V and the concentrations $(c_1, c_2, ..., c_m)$ of the m ionic species. The proof follows [98] and is based on the decoupling of the system in Slotboom variables and a fixed point argument. We use the fixed point argument is

based on the formulation in Slotboom variables, namely

$$u_i = c_i \exp(\beta z_i V) \text{ for } i = 1, ..., m.$$

Then the system reads as

$$-\gamma \partial_x (A \partial_x V) = A \sum_{i=1}^{m} z_i u_i \exp(-\beta z_i V) + \kappa \partial A \sigma, \tag{2.3}$$

$$0 = \partial_x (D_i A \exp(-\beta z_i V) \partial_x u_i) \text{ for } i = 1, ..., m, \tag{2.4}$$

with boundary conditions

$$\begin{aligned} V(L) = V_D \text{ and } V(0) = 0 \\ u_i = u_{i,B} = c_{i,B} \exp(\beta z_i V) \text{ on } \{0, L\} \text{ for } i = 1, ..., m. \end{aligned} \tag{2.5}$$

We will also use the notation $\vec{u} = (u_1, ..., u_m)$ in the following.

2.2.1 Existence of stationary solutions

The fixed point argument is based on the assumptions:

A1 Let Ω be an interval.

A2 The bath concentrations and the applied voltage are bounded, that is $(\vec{u}_D, V_D)|_{\partial\Omega} \in L^\infty(\partial\Omega)^{m+1}$ and there exist $U \geq 0$ such that $e^{-U} \leq \inf_{\partial\Omega} u_i$ and $e^U \geq \sup_{\partial\Omega} u_i$ for all $i = 1, ...m$.

A3 The functions $A(x) = \pi r^2(x)$ and $D = D(x)$ are measurable and $0 < D_* \leq D(x) \leq D^*$. The radius function $r(x)$ satisfies $0 < r_* \leq r(x) \leq r^*$ and for all x in Ω.

A4 The surface charge $\sigma(x) \in L^\infty(\Omega)$

Assumptions A2 and A4 bounds on the applied potential and the bath concentration on both sides of the pore as well as the surface charge. Assumption A3 ensures that the radius of the considered pore is bounded from below from 0, such that the pore is not blocked and the diffusion coefficients do not vanish.

Theorem 2. *Let assumptions (A1)-(A4) hold. Then problem* (2.3) - (2.5) *has a weak solution* $(V, \vec{u}) \in H^1(\Omega) \cap L^\infty(\Omega)^{m+1}$ *which satisfies:*

$$e^{-U} \leq u_i(x) \leq e^U \ \forall i \text{ and a.e. in } \Omega. \tag{2.6}$$

First we show existence of solutions of two following decoupled problems

1. Given $\vec{u}^0 \in L^\infty(\Omega)^{m+1}$ there exists a solution $V^1 \in H^1(\Omega) \cap L^\infty(\Omega)$ to the Poisson equation

$$-\gamma\partial_x(A(x)\partial_x V) = A(x)\sum_{i=1}^{m} z_i u_i^0 \exp\left(-\beta z_i V\right) + \kappa\partial A(x)\sigma, \tag{2.7}$$

   subject to the boundary conditions .

2. Given $V^1 \in L^\infty(\Omega)^{m+1}$, there exists a solution $\vec{u}^1 \in L^\infty(\Omega)^{m+1}$ of the continuity equations

$$0 = \partial_x(D_i A(x)\exp\left(-\beta z_i V^1\right)\partial_x u_i^1) \text{ for } i = 1, ..., m, \tag{2.8}$$

   subject to the boundary conditions $u_i^1 = u_{i,B}$ on $\{0, L\}$ for $i = 1, ..., m$.

Note that we refer to the weak solution of the problems (2.7) and (2.8). As a result of the proof regarding the existence of the solutions of the equation (2.7) we conclude that the mapping $\mathcal{H}(\vec{u}^0) = (V^1)$ is compact and bounded in L^∞ on the set

$$N = \{u \in L^2(\Omega)^m : e^{-U} \leq u_i \leq e^U \text{ a.e. in (0,L) and for } i = 1, 2, ..., m\}.$$

Next step is to show that $\mathcal{G}(\vec{V}^1) = (\vec{u}^1)$ is well defined and continuous on a precompact $\mathcal{H}(N)$ to use a corollary from Schauder's Fixed Point Theorem and conclude the solution of the entire system. We recall Schauder's Fixed Point Theorem as well as Leray-Schauder's Fixed Point Theorem as we make use of the second one as well.

Theorem 3 (Schauder's Fixed Point Theorem)**.** *Let $\mathcal{U}$ be a compact and convex set in the Banach space X and $\mathcal{T}$ be a continuous mapping of $\mathcal{U}$ into itself. Then $\mathcal{T}$ has a fixed point, that is, $\mathcal{T}x = x$ for some $x \in \mathcal{U}$.*

We also use a special case of this theorem known as

Theorem 4 (Leray-Schauder's Fixed Point Theorem)**.** *Let X be a Banach space and $\mathcal{T} : X \times [0, 1] \to X$ a compact mapping such that*

- *$\mathcal{T}(x, 0) = 0$ for each $x \in X$,*
- *there exists a constant such that for each pair $(x, \sigma) \in X \times [0, 1]$ which satisfies $\mathcal{T}(x, \sigma) = x$ we have $\|x\|_X < M$.*

Then operator $\mathcal{T}(\cdot, 1)$ has a fixed point.

We also use a corollary of the Schauder's Fixed Point Theorem from [57][Chapter 11].

Corollary 2.2.1.1. *Let $\mathcal{U}$ be a closed and convex set in a Banach space X and let $\mathcal{T}$ be a continuous mapping of $\mathcal{U}$ into itself such that a set $\mathcal{T}(\mathcal{U})$ is pre-compact. Then $\mathcal{T}$ has a fixed point.*

The proofs of both theorems can be found in [57][Chapter 11]. We begin the proof of the Theorem 2 with a lemma.

Lemma 1. *Let $\vec{u}^0 \in L^\infty(\Omega)^m$ satisfy $0 < u_* \leq u_i^0 \leq u^*$ for every i a.e. in Ω and (A1) – (A4) hold. Then (2.7) has a unique weak solution $V^1 \in H^1(\Omega) \cap L^\infty(\Omega)$.*

Proof of Lemma 1. Throughout the proof of this lemma we omit the superscript 0 in the u_i^0 to enhance readability. We will look for the solutions in a form $V = \psi + \bar{\psi}$ where $\bar{\psi}$ solves

$$-\gamma\partial_x(A(x)\partial_x\bar{\psi}) = 0 \quad \text{and } \bar{\psi}(0) = 0, \bar{\psi}(L) = V_D, \tag{2.9}$$

and ψ is a solution of the problem (2.7) satisfying $\psi(0) = \psi(L) = 0$. Then the V solves the original problem due to the superposition principle.

As a boundary value ODE with homogenous right hand side equation (2.9) can be explicitly solved with integration. First integral of the equation leads to $A\partial_x\bar{\psi} = C_1$ and then integrating for the second time leads to $\bar{\psi}(x) = \int_0^x \frac{C_1}{A(t)}dt + C_2$. The constants C_1 and C_2 are taken to satisfy the boundary equation for $\bar{\psi}$. The integrability of the last equation is provided by the fact that $A(x) > A_* \geq 0$.

Now we show the existence of the solution ψ as a fixed point of an operator $\mathcal{T}(y, \lambda) : L^2(\Omega) \times [0, 1] \to L^2(\Omega)$ that is a solution of

$$\begin{aligned} -\gamma\partial_x(A(x)\partial_x\psi) &= \lambda\left(A(x)\sum_{i=1}^m z_i u_i \exp\left(-\beta z_i y\right) + \kappa\partial A(x)\sigma(x)\right) \\ \text{and } \psi(0) &= 0, \psi(L) = 0. \end{aligned} \tag{2.10}$$

For the RHS of the equation (2.10) and $\lambda = 1$ a lower and upper bound (LB and

UB respectively) are given by

$$\begin{aligned}
LB(y) :=& A^* \sum_{\substack{i=0 \\ z_i<0}}^{m} z_i u^* \exp\left(-\beta z_i y\right) + A_* \sum_{\substack{i=0 \\ z_i>0}}^{m} z_i u_* \exp\left(-\beta z_i y\right) + \kappa \partial A_* \sigma_* \\
\leq & A \sum_{i=1}^{m} z_i u_i \exp\left(-\beta z_i y\right) + \kappa \partial A \sigma \\
\leq & A_* \sum_{\substack{i=0 \\ z_i<0}}^{m} z_i u_* \exp\left(-\beta z_i y\right) + A^* \sum_{\substack{i=0 \\ z_i>0}}^{m} z_i u^* \exp\left(-\beta z_i y\right) \\
& + \kappa \partial A^* \sigma^* := UB(y).
\end{aligned}$$

Next we take $\overline{V}$ and $\underline{V}$ to be solutions of the algebraic equations

$$LB(\underline{V}) = 0 \text{ and } UB(\overline{V}) = 0.$$

Existence of solutions of this algebraic equation is ensured by a Darboux theorem if there exist i, j such that $z_i z_j < 1$. Then $\overline{V}$ and $\underline{V}$ satisfy the following inequalities:

$$-\gamma \partial_x (A \partial_x \overline{V}) - A \sum_{i=1}^{m} z_i u_i \exp\left(-\beta z_i \overline{V}\right) - \kappa \partial A \sigma \leq 0,$$

$$-\gamma \partial_x (A \partial_x \underline{V}) - A \sum_{i=1}^{m} z_i u_i \exp\left(-\beta z_i \underline{V}\right) - \kappa \partial A \sigma(x) \geq 0.$$

Now $\overline{V}$ and $\underline{V}$ are sub– and super-solution of the problem (2.10) since the function

$$\theta(x, y) = A \sum_{i=0}^{m} z_i u_i \exp\left(-\beta z_i y\right) + \kappa \partial A \sigma,$$

is decreasing in y. Next we set $K = \max\{|\overline{V}|, |\underline{V}|\}$ and denote by f_K the truncation operator, namely

$$f_K(x) = \begin{cases} K & \text{if } f(x) > K \\ f(x) & \text{if } -K \leq f(x) \leq K \\ -K & \text{if } f(x) < -K. \end{cases}$$

We define the fixed point operator $\mathcal{T}_K(y, \lambda) : L^2(\Omega) \times [0, 1] \to L^2(\Omega)$, given by

$\mathcal{T}_K(y,\lambda)=\psi$ where ψ is the solution of

$$\begin{aligned} -\gamma\partial_x(A(x)\partial_x\psi) &= \lambda\left(A(x)\sum_{i=1}^{m} z_i u_i \exp\left(-\beta z_i y_K\right)+\kappa\partial A(x)\sigma(x)\right) \\ \text{and } \psi(0)=0, &\psi(L)=0. \end{aligned} \tag{2.11}$$

From the definition of K we immediately see that if the fixed point exists then it is bounded by the sub and super-solution so $|\psi|<K$.

Since the truncation operator from $L^2(\Omega)\to L^2(\Omega)$ is continuous, the RHS of (2.11) depends continuously in $L^2(\Omega)$ on $(y,\lambda)\in L^2(\Omega)\times(0,1)$. As the solutions of the elliptic equations in H^1 depend continuously on the L^2 right hand side and H^1 boundary data (see [57] chapter 8 corollary 8.7) we conclude that the operator $\mathcal{T}_K$ is continuous. To show that the range of $\mathcal{T}_K$ is also bounded in H^1 we take a test function $\phi=\psi$ a.e. to obtain

$$\begin{aligned} &\|\psi\|_{1,2}^2\le\|\psi\|_{L_2}^2+\|\partial_x\psi\|_{L_2}^2\le\|\psi\|_{L_2}^2+\int_\Omega|(\partial_x\psi)^2|dx \\ \le&\|\psi\|_{L_2}^2+\check{C}\int_\Omega\psi\left(A(x)\sum_{i=1}^{m} z_i u_i\exp\left(-\beta z_i y_K\right)+\partial A(x)\sigma(x)\right)dx \\ \le&\|\psi\|_{L_2}^2+\check{C}\left\|\left(A(x)\sum_{i=1}^{m} z_i u_i\exp\left(-\beta z_i y_K\right)+\partial A(x)\sigma(x)\right)\right\|_{L_2}\|\psi\|_{L_2} \\ \le&C(\Omega,A^*,\sigma^*)\left\|\left(\sum_{i=1}^{m}|z_i|u^*\exp\left(-\beta z_i K\right)\right)\right\|_{L^2}\|\psi\|_{L_2}\le\bar{C}\|\psi\|_{L_2}. \end{aligned} \tag{2.12}$$

Than applying the the Poincaré inequality we obtain

$$\|\psi\|_{1,2}^2\le\tilde{C}\|\psi\|_{1,2},$$

which leads to

$$\|\psi\|_{1,2}\le\tilde{C}. \tag{2.13}$$

Therefore, we obtain that $\mathcal{T}_K$ is compactly continuous and also $\mathcal{T}_K(y,0)=0\ \ \forall y\in L^2(\Omega)$. What is more from (2.12) we conclude that for each pair $(\psi,\lambda)\in H^1\times[0,1]$ which satisfies $\mathcal{T}_K(\psi,\lambda)=\psi$ we have $\|\psi\|_{1,2}<M$. From the boundedness of $\mathcal{T}_K$ and the Theorem 4 [Leray-Schauder's] we obtain the existence of a fixed point of $\mathcal{T}_K(\cdot,1)$. Then the function $V:=\psi+\bar{\psi}$ is a solution of problem (2.7), which satisfies $V^1\in H^1(\Omega)\cap L^\infty(\Omega)$. From the inequality (2.12) we also conclude that image $\mathcal{H}(N)$ is totally bounded in the L^∞ norm hence $\mathcal{H}$ is a compact and continuous operator. Compactness of the operator $\mathcal{H}$ ensures that the image $\mathcal{H}(N)$ is pre-compact and

totally bounded as an image of a bounded set. We conclude by showing that the solution V^1 is unique. Let us assume that there exist two solutions V_1 and V_2. Then $h = V_1 - V_2$ satisfies

$$-\partial_x(A\partial_x h) = [A\sum_{i=1}^{m} z_i u_i \exp(-\beta z_i \xi_i)]h,$$

with boundary conditions $h = 0|_{\{0,L\}}$ where $V_1 \geq \xi_i \geq V_2$. The maximum principle implies that $h \equiv 0$ hence the solution is unique. □

We showed that the mapping $\mathcal{H}(\vec{u}^0) = (V^1)$ is continuous and compact on the set

$$N = \{u \in L^2(Q)^m : e^{-U} \leq u_i \leq e^U \text{ a.e. in (0,L) and for } i = 1, 2, ..., m\}.$$

We continue by showing existence of the solutions to (2.8) and analysing properties of the $\mathcal{G}$ on a pre-compact set $\mathcal{H}(N)$.

Lemma 2. *Assume that (A1) – (A4) hold and $V^1 \in \mathcal{H}(N)$. Then problem* (2.8) *has a unique solution u^1. The solution operator $\mathcal{G} : V^1 \mapsto u^1$ maps $\mathcal{H}(N)$ to N and is continuous.*

Proof of the Lemma 2. For $V \leq K$ we have that

$$0 < D_i A(x) \exp(-\beta z_i V) \leq \hat{C}$$

for some constant $\hat{C}$. From the result in [57] for elliptic equation in divergence form we conclude that (2.8) has a unique solution u_i. Moreover the maximum principle ensures that $e^{-U} \leq u_i \leq e^U$ for all $i = 1, 2, ..., m$. Thus $\mathcal{G}$ is well defined and maps into N.

To address continuity of the operator $\mathcal{G}$ we consider sequence $V^k \to V$ in $\mathcal{H}(N) \subset L^\infty \cap H^1$. Then $D_i A(x) \exp(-\beta z_i V_k) \to D_i A(x) \exp(-\beta z_i V)$ in $L^\infty(\Omega)$ with the uniform bound. For u_i^k, a solution of the problem

$$\nabla(D_i A(x) \exp(-\beta z_i V^k)\nabla u_i) = 0,$$

we obtain that u_i^k is uniformly bounded in $H^1(\Omega)$ and hence there exists a weakly convergent subsequence $u_i^k \to \bar{u}_i$. From the density of $L^\infty(\Omega)$ and $W^{1,\infty}(\Omega)$ in $H^1(\Omega)$ and the uniqueness of the limit we conclude that $u_i^k \to u_i$ weakly in $H^1(\Omega)$ and thus strongly in $L^2(\Omega)$ which implies continuity of the operator $\mathcal{G}$. □

What is more, the concatenated operator $\mathcal{G}(\mathcal{H}(\cdot))$ maps a N into N which is a closed convex set in a Banach space $L^2(\Omega)$. In the Lemma 1 we have shown that the operator $\mathcal{H}$ is continuous and compact. In the Lemma 2 we proved that the operator $\mathcal{G}$ is continuous, hence the concatenated operator $\mathcal{G}(\mathcal{H}(\cdot))$ is compact. As a image of a bounded set N, $\mathcal{G}(\mathcal{H}(N))$ is a pre-compact subset of $L^2(\Omega)$. From the corollary 2.2.1.1 we obtain the fixed point of $\mathcal{G}(\mathcal{H}(\cdot))$ in N which is a solution of problems (2.3)-(2.4).

Global regularity

In section 2.2.1 we showed the existence of a solution of the problem (2.3)-(2.4) in $H^1(\Omega)^{m+1} \cap L^\infty(\Omega)^{m+1}$. Our next goal is to show higher regularity of the solution. What in fact we obtain is that, under some additional assumptions on the functions $A(x)$ and $D(x)$, every weak solution of considered problem belongs also to the space $H^2(\Omega)^{m+1}$.

Theorem 5. *Let the assumptions (A1)-(A4) hold and assume that $A, D_i \in W^{1,\infty}(\Omega)$, then every weak solution $(V, \vec{u}) \in H^1 \cap L^\infty(\Omega)^{m+1}$ satisfies*

$$(V, \vec{u}) \in H^2(\Omega)^{m+1}.$$

Proof. Proof of the theorem can be found in [98] and is based on [57][Chapter 8] and uses Sobolev embedding for $k = 1$. □

Uniqueness

In order to show the uniqueness we need a higher regularity of the solution than the one obtained in Theorem 2. To prove the uniqueness authors in [98] show that the Frechet derivative of 1D PNP system is invertible and bounded. Then the implicit function theorem gives the result.

Theorem 6. *Let the assumptions of the Theorem 5 hold. If U, satisfies $|U| < \theta$, for some sufficiently small θ, then the problem (2.3)-(2.4) has a locally unique solution $(\vec{u}^*, V^*) \in H^2(\Omega)^{m+1}$. This solution depends continuously differentiably on V_D when considered as a map from $\{U \in \mathbb{R} : |U| < \theta\}$ into $(H^2(\Omega))^{m+1}$.*

Proof of the theorem can be found in [98, Theorem 3.4.1].

2.3 Nonlinear PNP system

In this section we sketch an existence result of the 1D Area Averaged nonlinear Poisson-Nernst-Planck system, which was introduced in section 1.3.7. In [26] the authors discuss the existence of the solution for the nPNP system for general 2 and $3D$ setup , that is

Theorem 2.3.1 (Existence of solutions of the nPNP system [26]). *Let $\sigma \in H^1(\Gamma_N) \cap L^\infty(\Gamma_N)$, the applied potential $V_{app} \in H^{1/2}(\Gamma_R \cap \Gamma_L) \cap L^\infty(\Gamma_R \cap \Gamma_L)$ and the boundary concentrations $c_i|_{\Gamma_R} \in H^{1/2}(\Gamma_R \cap \Gamma_L) \cap L^\infty(\Gamma_R \cap \Gamma_L)$. Then there exists a solution $(c_1, .., c_m, V) \in \Big(H^1(\Omega) \cap L^\infty(\Omega)\Big)^{m+1}$ to (1.5),(1.19a), (1.19b).*

Note that the authors also provide higher regularity results for the small initial data and uniqueness of the solutions for small applied potential and small bath concentrations.

We present a sketch of the proof of the 1D Area Averaged version of the model. The proof follows the reasoning from the previous section and is based on the Schauder's Fixed Point Theorem. The 1D Area Averaged version of equation (1.19a)– (1.19b) reads

$$-\gamma \partial_x (A \partial_x V) = A \sum_{i=1}^{m} z_i c_i + \kappa \partial A \sigma, \quad (2.14)$$

$$\partial_x \Big(D_i A \Big[(1-\rho)\partial_x c_i + c_i \partial_x \rho + \beta z_i (1-\rho) c_i \partial_x V) \Big] \Big) = 0 \text{ for } i = 1, ..., m, \quad (2.15)$$

where $\rho = \sum_i^m c_i$, with Dirichlet boundary conditions

$$V(0) = 0, V(L) = V_D \quad \text{and} \quad c_i = c_{i,B}|_{\{0,L\}} \text{ for } i = 1, ..., m. \quad (2.16)$$

The existence of the solutions of the system is given by the following theorem

Theorem 7. *Let assumptions (A1)-(A4) hold. Then system* (2.14) - (2.15) *has a weak solution $(V, \vec{u}) \in H^1 \cap L^\infty(\Omega)^{m+1}$ which satisfies*

$$e^{-U} \leq u_i^* \leq e^U \text{ for all } i = 1, 2, ..., m \text{ and a.e. in } [0, L].$$

We prove the existence of the solution by decoupling the system and then using a fixed point argument. We start by introducing the entropy variables, that reads

$$c_i = \frac{\exp(u_i - \beta z_i V)}{1 + \sum_{j=1}^m \exp(u_j - \beta z_j V)}$$

which leads to the system

$$-\gamma\partial_x(A\partial_x V) = A\sum_{i=1}^{m} z_i \frac{\exp(u_i - \beta z_i V)}{1+\sum_j^m \exp(u_j - \beta z_j V)} + \kappa\partial A\sigma,$$
$$0 = \partial_x(D_i A \frac{\exp(u_i - \beta z_i V)}{(1+\sum_{j=1}^m \exp(u_j - \beta z_j V))^2}\partial_x u_i) \text{ for } i = 1, ..., m.$$

We proceed with the following steps

1. For a given $\vec{u}^0 \geq 0 \in L^2(\Omega)$ there exists a solution V^1 to the Poisson equation

$$-\gamma\partial_x(A\partial_x V) = A\sum_{i=1}^{m} z_i \frac{\exp(-u_i^0 \beta z_i V)}{1+\sum_j^m u_j^0 \exp(-\beta z_j V)} + \kappa\partial A\sigma, \tag{2.17}$$

   with respect to the boundary condition

$$V^1(L) = V_D \text{ and } V^1(0) = 0. \tag{2.18}$$

2. Operator $\mathcal{G} : (\vec{u}^0) \to (\vec{u}^0, V^1)$ where V is the solution of the equation (2.17) is compact and continuous on N.

3. For given $(V^1, u^0) \in L^\infty(\Omega)^{m+1} \cap H^1(\Omega)^{m+1}$ there exist a solution $\vec{v}^1 \in L^\infty(\Omega)^{m+1} \cap H^1(\Omega)^{m+1}$ of the continuity equations

$$\begin{aligned} 0 = \partial_x(D_i A \frac{\exp(u_i - \beta z_i V)}{(1+\sum_{j=1}^m \exp(u_j - \beta z_j V))^2}\partial_x v_i) \text{ for } i = 1, ..., m. \\ v_i = u_{i,B} \text{ on } \{0, L\} \text{ for } i = 1, ..., m, \end{aligned} \tag{2.19}$$

4. Operator $\mathcal{H} : (\vec{u}^0, V^1) \to (\vec{v}^1)$ where V^1 is the solution of the equation (2.19) is continuous on $\mathcal{G}(N)$.

5. We conclude with the convergence of the iterative schema and use the Schauder Fixed Point Theorem to ensure the solution of the system (2.14) - (2.15).

We proceed with formulation the Lemma

Lemma 3. *For a given $\vec{u}^0 \geq 0 \in L^2(\Omega)^m$ there exists a solution $V^1 \in L^\infty(\Omega) \cap H^1(\Omega)$ of the equation* (2.17) .

Proof. As the RHS of the equation (2.17) is bounded by $A^*(\sum_{i=1}^m |z_i|) + \partial A^* \sigma^*$ end therefore a super-solution (and respectively sub-solution) of the equation (2.17). This ensures existence of solution of equation (2.17). □

Lemma 4. *Operator $\mathcal{G} : (\vec{u}) \to (\vec{u}, V)$, where V is the solution of the equation* (2.17)*, is continuous on N.*

Proof. As the solutions of the elliptic equations in H^1 depend continuously on the L^2 right hand side and H^1 boundary data (see [57] chapter 8 corollary 8.7) we conclude that the operator $\mathcal{G}$ is Lipchitz continuous on N. □

Lemma 5. *For a given $(V^1, \vec{u}^0) \in L^\infty(\Omega)^{m+1} \cap H^1(\Omega)^{m+1}$ there exists a solution $\vec{v}^1 \in L^\infty(\Omega)^m \cap H^1(\Omega)^m$ of the equation* (2.19) *.*

Proof. The existence of the solution is guaranteed by [57][Theorem 8.3]. Since $D_i A \frac{\exp(u_i - \beta z_i V)}{(1+\sum_j^m \exp(u_j - \beta z_j V))^2} \leq D^* A^* \in L^\infty$ and $\bar{v}_D \leq e^U$ Theorem 8.3 in [57] ensures the existence of solutions. The function e^U is a super-solution of (2.19), hence $v \leq e^U$. □

Lemma 6. *Operator $\mathcal{H} : L^2(\Omega)^m \times H^1(\Omega) \to L^2(\Omega)^m$ is continuous.*

Proof. The lemma is a consequence of the compactness of the embedding L^2 in H^1 and the bound on the diffusion coefficient of the equation (2.19).

Therefore, we can use Schauder's fixed-point theorem, which ensures the existence of a fixed point of $\mathcal{H}(\mathcal{G}(N))$. This fixed point is a solution of (2.14) – (2.15).

Chapter 3

Asymptotic analysis of the Poisson-Nernst-Planck equations in radially symmetric pores with surface charge

In this chapter we introduce an asymptotic analysis of the PNP system applied to model ion transport through long and narrow pore. The chapter is based on the research presented in [102]. We present a simplified model for ion transport based on matching the asymptotic orders. That allows us to calculate the approximation of the PNP solution without solving the nonlinear 2D system. In the chapter we begin with the PNP system in unscaled form and then perform a scaling that allows us to distinguish different asymptotic regimes. In additions, we present an algorithm that can be used to compute the asymptotic solution. In the end of the chapter we show the results of the comparison of the obtained model with the results of the two dimensional simulations.

3.1 The PNP equations

We start by presenting the mathematical model and its scaling which serves as the basis of our asymptotic analysis. For ease of presentation, and because this is a typical set-up in practice, we restrict our attention to an ideal 1:1 electrolyte comprised of positive and negative ions of valency one and with concentrations p^* and n^* respectively (measured in moles per unit volume). Note that we use $*$ to indicate dimensional variables throughout the chapter.

The PNP equations for the electric potential $V^* = V^*(\boldsymbol{x}^*, t^*)$, negative and positive molar concentrations $n^* = n^*(\boldsymbol{x}^*, t^*), p^* = p^*(\boldsymbol{x}^*, t^*)$ read as

$$-\nabla^* \cdot (\epsilon_r \epsilon_0 \nabla^* V^*) = n_a e(p^* - n^*), \tag{3.1a}$$

$$\frac{\partial p^*}{\partial t^*} + \nabla^* \cdot \mathcal{J}_p^* = 0, \qquad \frac{\partial n^*}{\partial t^*} + \nabla \cdot \mathcal{J}_n^* = 0, \tag{3.1b}$$

$$\mathcal{J}_n^* = -D_n \left(\nabla^* n^* - \frac{e}{k_b T} n^* \nabla^* V^* \right), \tag{3.1c}$$

$$\mathcal{J}_p^* = -D_p \left(\nabla^* p^* + \frac{e}{k_b T} p^* \nabla^* V^* \right). \tag{3.1d}$$

Here $\mathcal{J}_p^*$ and $\mathcal{J}_n^*$ are the flux of positive and negative ions, respectively, n_a is the Avogadro number and the $\frac{k_b T}{e}$ is often donoted as thermal voltage. The parameters D_p and D_n are the diffusion coefficients of the positive and negative ions, respectively, and the domain Ω is assumed axially symmetric being given by

$$\Omega = \{(x^*, y^*, z^*) : 0 \leq x^* \leq L^*, 0 \leq \sqrt{y^{*2} + z^{*2}} \leq R^*(x^*)\},$$

where $R^*(x^*)$ is the radius of the pore as a function of x^*. The boundary of Ω is split into three subdomains, the left and the right entrance of the nanopore

$$\Omega_l = \{(x^*, y^*, z^*) \in \partial\Omega, x^* = 0\} \text{ and } \Omega_r = \{(x^*, y^*, z^*) \in \partial\Omega, x^* = L\},$$

as well as the nanopore walls $\Omega_N = \{(x^*, y^*, z^*) \in \partial\Omega, \sqrt{y^{*2} + z^{*2}} = R^*(x^*)\}$. System (3.1) is supplemented with the following boundary conditions:

$$V^*|_{\Omega_l} = 0, \quad V^*|_{\Omega_r} = V_{appl}, \quad \{n^*, p^*\}|_{\Omega_l} = \{n_l, p_l\}, \quad \{n^*, p^*\}|_{\Omega_r} = \{n_r, p_r\}, \tag{3.2}$$

$$\mathcal{J}_p^* \cdot \boldsymbol{N}|_{\Omega_N} = \mathcal{J}_n^* \cdot \boldsymbol{N}|_{\Omega_N} = \boldsymbol{0}, \quad \left.\frac{\partial V^*}{\partial N^*}\right|_{\Omega_N} = \frac{\sigma^*(x^*)}{\varepsilon}. \tag{3.3}$$

where $\partial/\partial N^*$ denotes the normal derivative to the pore boundary with respect to its unit outward normal $\boldsymbol{N}$, defined by

$$\boldsymbol{N} = \left(\boldsymbol{e}_r - \frac{dR^*}{dx^*} \boldsymbol{e}_x \right) \left(1 + \left(\frac{dR^*}{dx^*} \right)^2 \right)^{-1/2},$$

$\sigma(x^*)$ is the surface charge density on the pore wall and ε the permittivity of the electrolyte. The Dirichlet conditions (3.2) correspond to a prescribed applied voltage and prescribed ion concentrations at each opening of the pore and in the bath regions, respectively. Here, for computational convenience, these are imposed on a

fixed external boundary whereas it could be argued that these ought to be imposed as far-field conditions. However these two sets of boundary conditions have almost identical solutions provided the pore is sufficiently wide when it is terminated by the artificial boundaries Ω_l and Ω_r. Condition (3.3) ensures that there is no ion flux through the pore walls and prescribes the fixed surface charge at these walls. We note that surface charge condition is asymptotically correct only if the permittivity ε of the electrolyte is much greater than that of the pore walls (which is the case for aqueous electrolytes); for more details see [33].

The current-voltage curve (IV curve in short) is commonly used to characterise the behaviour of ion channels and nanopores. The respective current flow $I^*(x^*, t^*)$ can be computed by calculating the current flow through a cross-section on the pore, at $x^* = X^*$ say, being given by

$$\mathcal{J}^*(x^*, t^*) = n_a e \int\limits_{\{y^{*2}+z^{*2} \leq R^{*2}(X^*)\} \cap \{x^* = X^*\}} \boldsymbol{e}_x \cdot (\mathcal{J}_p^* - \mathcal{J}_n^*)|_{x^*=X^*} dS^*. \tag{3.4}$$

3.1.1 Scaling

We nondimensionalise system (3.1) by introducing a typical lateral lengthscale L, a typical pore radius $\bar{R}$, a typical concentration $\bar{c}$, and a typical surface charge $\bar{\sigma}$. The great disparity in size between the lateral lengthscale L and the pore radius $\bar{R}$ motivates us to rescale differently in the these two dimensions. This results in different scalings for the fluxes in the radial and lateral directions. We introduce the radial variables $r^* = \sqrt{y^{*2} + z^{*2}}$ and nondimensionalise as follows

$$x^* = \bar{L}x, \quad r^* = \bar{R}r, \quad p^* = \bar{c}p, \quad n^* = \bar{c}n, \quad \sigma^* = \bar{\sigma}\sigma, \quad V^* = \frac{k_B T}{e}\phi$$
$$\mathcal{J}_p^* \cdot \boldsymbol{e}_x = \frac{\bar{D}\bar{c}}{L}u_p, \quad \mathcal{J}_p^* \cdot \boldsymbol{e}_r = \frac{\bar{D}\bar{c}\bar{R}}{\bar{L}^2}w_p, \quad \mathcal{J}_n^* \cdot \boldsymbol{e}_x = \frac{\bar{D}\bar{c}}{\bar{L}}u_n, \mathcal{J}_n^* \cdot \boldsymbol{e}_r = \frac{\bar{D}\bar{c}\bar{R}}{\bar{L}^2}w_n,$$

where $\bar{D}$ is a typical ionic diffusivity which we assume to be constant everywhere inside the domain. This leads to the following dimensionless formulation of system

(3.1)

$$\frac{\partial p}{\partial t} + \frac{\partial u_p}{\partial x} + \frac{1}{r}\frac{\partial}{\partial r}(r w_p) = 0, \tag{3.5a}$$

$$\frac{\partial n}{\partial t} + \frac{\partial u_n}{\partial x} + \frac{1}{r}\frac{\partial}{\partial r}(r w_n) = 0, \tag{3.5b}$$

$$\delta^2 \frac{\partial^2 \phi}{\partial x^2} + \frac{1}{r}\frac{\partial}{\partial r}\left(r\frac{\partial \phi}{\partial r}\right) = \frac{1}{\Lambda^2}(n-p), \tag{3.5c}$$

$$u_p = -\kappa_p\left(\frac{\partial p}{\partial x} + p\frac{\partial \phi}{\partial x}\right), \quad w_p = -\frac{\kappa_p}{\delta^2}\left(\frac{\partial p}{\partial r} + p\frac{\partial \phi}{\partial r}\right), \tag{3.5d}$$

$$u_n = -\kappa_n\left(\frac{\partial n}{\partial x} - n\frac{\partial \phi}{\partial x}\right), \quad w_n = -\frac{\kappa_n}{\delta^2}\left(\frac{\partial n}{\partial r} - n\frac{\partial \phi}{\partial r}\right), \tag{3.5e}$$

$$w_p - \frac{dR}{dx}u_p\Big|_{r=R(x)} = 0, \qquad w_n - \frac{dR}{dx}u_n\Big|_{r=R(x)} = 0, \tag{3.5f}$$

$$\frac{\partial \phi}{\partial r} - \delta^2 \frac{dR}{dx}\frac{\partial \phi}{\partial x}\Big|_{r=R(x)} = \Upsilon\left(1+\delta^2\left(\frac{dR}{dx}\right)\right)^{1/2}\sigma(x), \tag{3.5g}$$

and the scaled boundary conditions at the ends of the pore. (3.5h)

The dimensionless parameters in the problem are defined by

$$\Upsilon = \frac{\bar{R}\bar{\sigma}}{\varepsilon\frac{e}{k_B T}}, \quad \delta = \frac{\bar{R}}{\bar{L}}, \quad \Lambda = \frac{L_D}{\bar{R}}, \quad \kappa_p = \frac{D_p}{\bar{D}}, \quad \kappa_n = \frac{D_n}{\bar{D}}, \tag{3.6}$$

and where L_D, the Debye length, is given by

$$L_D = \left(\frac{\varepsilon n_a k_B T}{\bar{c}e^2}\right)^{1/2}.$$

Note that δ is the aspect ratio of the pore (typically small), while Λ measures the ratio of the Debye length of the electrolyte to the typical pore width. Thus where Λ is large the pore radius is much smaller than the Debye length (which is the limit used to derive 1D Area Averaged PNP equations). However given that L_D for even a 0.01 Molar solution is only around 4.5nm it is much more appropriate to consider $\Lambda = O(1)$ (or possibly even $\Lambda \ll 1$). The other particularly interesting parameter is Υ; if $\Upsilon \ll 1$ then the surface charge is insufficient to induce significant ion concentration changes across the pore whereas if $\Upsilon = O(1)$, or greater, it induces concentration changes that are sufficiently large to alter the pore's macroscopic behaviour. Finally κ_p and κ_n are the dimensionless diffusivities, which assuming a sensible measure of typical diffusivity $\bar{D}$ is chosen will be of $O(1)$, unless the two ion diffusivities differ significantly. The scaled current is given by $I^* = ((F\bar{D}\bar{c}\bar{R}^2)/L)I$

and can be determined from

$$\mathcal{J}(x,t) = \int_0^{R(x)} r(u_p - u_n)dr. \tag{3.7}$$

3.1.2 Parameter estimates and asymptotic limits

Nanopore devices vary in terms of length and opening radius as much as in terms of chemical composition. In this paper we focus on long and narrow pores, which have been studied in many experimental setups covered in the literature, see for example [115; 134]. In these pores the length is typically magnitudes of order bigger than the radius - for example Siwy et al. [134] work with pores of 12μm length and a few nanometers radius. We assume that the typical length is around $\bar{L} = 1\mu$m. The usual ionic concentration inside the pore varies from 0.01 Molar up to 1 Molar. The variations in the concentration lead to parameter ranging from $L_D = 0.3 - 3$nm. The opening radius may vary in the range $\bar{R} = 1 - 100$nm, hence the aspect ratio is in the range $\delta = 10^{-3} - 10^{-1}$. All other parameter values are listed in Table A.1.

k_B	$1.3806504 \times 10^{-23}$ [J/K]	$\bar{\sigma}$	1 [e/nm^2] = 0.16[C/m^2]
T	300 [K]	$\frac{e}{k_B T}$	0.025 [V]
ϵ_0	$8.854187817 \times 10^{-12}$[C /(Vm)]	$\bar{c}$	1 [M]
ϵ_r	78.4	$\bar{D}$	10^{-9} [m^2/s]
ϵ	$\epsilon_0\epsilon_r$	D_p	1.33
e	1.602176×10^{-19} [C]	D_n	0.79

Table 3.1: Physical constants and parameters.

The discussed parameter regimes motivate the following asymptotic limits. Let the dimensionless diffusivities κ_p and κ_n to be both $O(1)$. We shall only consider $\Upsilon = O(1)$, noting that the limit $\Upsilon \ll 1$ is uninteresting (because it corresponds to a wall charge that is too small to significantly affect the potential and concentrations inside the pore) and that the behaviour for the limit $\Upsilon \gg 1$ can be extracted directly from the distinguished limit $\Upsilon = O(1)$. The size of the one remaining parameter Λ, measuring the ratio of the Debye length to the pore radius, determines the asymptotic structure of the solution to the PNP equations. In particular there are three different limits that one might wish to consider

i) $\Lambda \gg 1$, corresponding to a Debye length that it much greater than the pore radius,

ii) $\Lambda = O(1)$ corresponding to a Debye length that is comparable to the pore radius, and

iii) $\Lambda \ll 1$ corresponding to a Debye length much smaller than the pore radius.

The large Λ limit (I) has been considered in detail in a number of previous works (*e.g.* [33; 26]) and is only applicable to extremely dilute aqueous solutions and narrow pores because the Debye length L_D is very small even for fairly dilute solutions (*e.g.* 1.3nm for a 0.1M solution). The small Λ limit (III) turns out to be physically rather dull because it corresponds to a Debye length that is much smaller than the pore radius meaning the the surface charge on the inside of the pore is effectively screened by the electrolyte and so does not significantly alter ion transport through the pore. Note that a similar limit was considered by Markowich in [98] in case of the semiconductor equations with no surface charge. The most interesting limit, both from a mathematical and physical perspective is (II) for which $\Lambda = O(1)$. Furthermore we claim that this limit is a distinguished asymptotic limit so that the results obtained by analysing this case also provides a good description of (III) the small Λ limits.

3.2 Asymptotic analysis in the limit $\Lambda = O(1)$, $\Upsilon = O(1)$, $\delta \ll 1$ and derivation of the Quasi-1D PNP model

In this section we discuss large aspect ratio nanopores ($\delta \ll 1$) with radii comparable to the Debye length, (*i.e.* $L_D = O(\bar{R})$ and hence $\Lambda = O(1)$). In this scenario the influence of the surface charge cannot be averaged over the area of the domain, resulting in a leading order problem that must be solved both in x and r. As discussed in Section 3.1.2, we shall also consider significant surface charge by formally taking the distinguished limit $\Upsilon = O(1)$.

In order to find an asymptotic solution of system (3.5a)-(3.5h) in the limit $\delta \to 0$, and with all other parameters of size $O(1)$ we make the following ansatz:

$$\begin{aligned}
&n = n_0(r,x,t) + \delta n_1(r,x,t) + \cdots, && p = p_0(r,x,t) + \delta p_1(r,x,t) + \cdots,\\
&\phi = \phi_0(r,x,t) + \delta \phi_1(r,x,t) + \cdots, &&\\
&u_n = u_{n,0}(r,x,t) + \delta u_{n,1}(r,x,t) + \cdots, && w_n = \delta w_{n,1}(r,x,t) + \cdots,\\
&u_p = u_{p,0}(r,x,t) + \delta u_{p,1}(r,x,t) + \cdots, && w_p = \delta w_{p,1}(r,x,t) + \cdots.
\end{aligned} \tag{3.8}$$

At leading order in δ in the flux equations (3.5d)-(3.5e) give the two equations

$$\frac{\partial n_0}{\partial r} - n_0 \frac{\partial \phi_0}{\partial r} = 0 \quad \text{and} \quad \frac{\partial p_0}{\partial r} + p_0 \frac{\partial \phi_0}{\partial r} = 0,$$

which can be integrated to obtain

$$n_0 = Q(x,t)\exp(\phi_0(r,x,t)) \quad \text{and} \quad p_0 = S(x,t)\exp(-\phi_0(r,x,t)), \tag{3.9}$$

where the functions $Q(x,t)$ and $S(x,t)$ are yet to be determined. Inserting these expressions into the Poisson-Boltzmann equation and its boundary condition, (3.5c) and (3.5g) gives

$$\frac{1}{r}\frac{\partial}{\partial r}\left(r\frac{\partial \phi_0}{\partial r}\right) = \frac{1}{\Lambda^2}\left(Q(x,t)\exp(\phi_0(r,x,t)) - S(x,t)\exp(-\phi_0(r,x,t))\right), \tag{3.10a}$$

$$\left.\frac{\partial \phi_0}{\partial r}\right|_{r=R(x)} = \Upsilon\sigma(x). \tag{3.10b}$$

3.2.1 Leading order solution for the potential

We seek solutions to (3.10a)-(3.10b) by introducing the new variables (*e.g.* see [4, Chapter 12])

$$\phi_0(r,x,t) = \frac{1}{2}\log\frac{S(x,t)}{Q(x,t)} + \psi(\xi,x,t) \quad \text{and} \quad r = R(x)\xi, \tag{3.11}$$

which result in the following problem for ψ:

$$\frac{1}{\xi}\frac{\partial}{\partial \xi}\left(\xi\frac{\partial \psi}{\partial \xi}\right) = \frac{1}{\lambda^2(x,t)}(e^{\psi} - e^{-\psi}), \tag{3.12a}$$

$$\psi \ \text{ bounded at } \ \xi = 0, \ \text{and} \ \left.\frac{\partial \psi}{\partial \xi}\right|_{\xi=1} = \beta(x). \tag{3.12b}$$

where

$$\beta(x) = \Upsilon\sigma(x)R(x), \qquad \text{and} \qquad \lambda(x,t) = \frac{\Lambda}{R(x)(S(x,t)Q(x,t))^{1/4}}. \tag{3.13}$$

Here $\lambda(x,t)$ gives the ratio of the Debye length, evaluated from the evolving ion concentrations, to the local pore radius. Thus the solution to (3.12a)-(3.12b),

$$\psi = \psi\left(\xi; \lambda(x,t), \beta(x)\right),$$

depends parametrically on x and t through $\lambda(x,t)$ and $\beta(x)$.

Approximate solution to (3.12a)-(3.12b) for $\beta(x) \gg 1$. We can make use of the fact that $\beta(x)$ is typically large (so that the gradient of ψ at the edge of the pore $\xi = 1$ is large) by noting that this suggests that $\psi(\xi;\lambda,\beta)$ is also large (an hypothesis

we justify *a posteriori* for sufficiently large λ). Making the large ψ ansatz means that (3.12a) can be approximated by

$$\frac{1}{\xi}\frac{\partial}{\partial\xi}\left(\xi\frac{\partial\psi}{\partial\xi}\right) \sim \frac{1}{\lambda^2(x,t)}e^{\psi} \tag{3.14}$$

which, when solved together with (3.12b), has a solution of the form

$$\psi(\xi,x,t) \sim 2\log\left(\operatorname{cosech}\left(\operatorname{arcoth}\left(\frac{\beta(x)+2}{2}\right)-\log\xi\right)\right)-\log\left(\frac{\xi^2}{2\lambda^2(x,t)}\right). \tag{3.15}$$

Notably this expression for ψ has a minimum (as a function of ξ) at the centre of the pore given by

$$\psi|_{\xi=0} = 3\log 2 + 2\log\lambda - 2\operatorname{arcoth}\left(\frac{\beta+2}{2}\right), \tag{3.16}$$

which for $\beta \gg 1$ is well-approximated by $\psi|_{\xi=0} = 3\log 2 + 2\log\lambda$. The approximation in going from (3.12a) to (3.14) can thus be justified if $\exp(-2\psi|_{\xi=0}) \ll 1$ which is true only if

$$\lambda(x,t) \gg \frac{1}{2^{3/2}}.$$

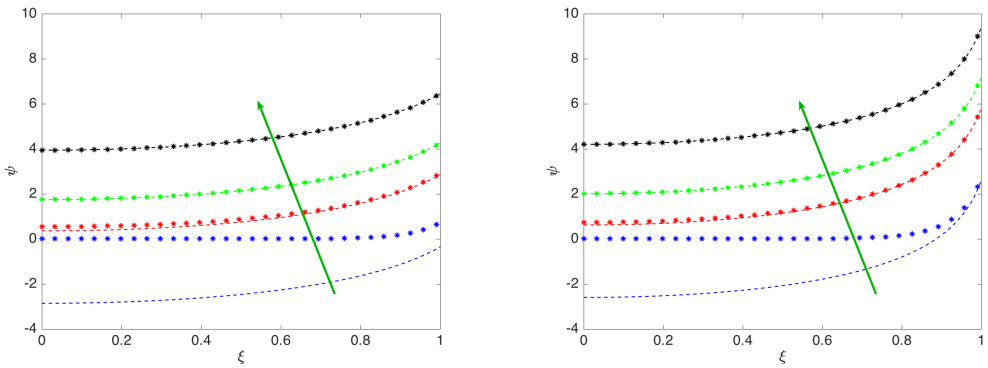

Figure 3.1: Comparison between numerical solution to (3.12) (stars) and its large-β asymptotic approximation (3.15) (dashed line). Here in the left-hand panel $\beta = 10$ while in the right $\beta = 50$. In both panels the values of λ taken are $\lambda = [0.1, 0.5, 1, 3]$ and the arrows indicate the direction of increasing λ.

Figure 3.1 illustrates the quality of the asymptotic solution for different values of λ and realistic values of $\beta = 10, 50$. Note that the approximation quality of the asymptotic solution improves as λ increases.

Approximate solution to (3.12a)-(3.12b) for $\lambda(x,t) \ll 1$. In this regime narrow Debye layers of width $O(\lambda)$ exist close to surface $\xi = 1$. In order to investigate the solution further we rescale, in the standard manner (see [100; 101]), about this surface by introducing the Debye layer coordinate ζ defined by

$$\xi = 1 - \lambda\zeta. \tag{3.17}$$

Rewriting (3.12a)-(3.12b) in terms of this new coordinate leads to the following equation and boundary condition for ψ

$$\frac{\partial^2\psi}{\partial\zeta^2} + \lambda\left(\zeta\frac{\partial^2\psi}{\partial\zeta^2} - \frac{\partial\psi}{\partial\zeta}\right) + O(\lambda^2) = (e^{\psi} - e^{-\psi}), \tag{3.18}$$

$$\left.\frac{\partial\psi}{\partial\zeta}\right|_{\zeta=0} = -B \qquad \text{where} \quad B = \lambda\beta, \tag{3.19}$$

$$\frac{\partial\psi}{\partial\zeta} \to 0 \qquad \text{as} \quad \zeta \to +\infty. \tag{3.20}$$

Here we consider the distinguished limit $B = O(1)$, that is $\beta = O(1/\lambda)$ noting that the solution we obtain is still valid for other sizes of this parameter. Formally we look for a solution in the Debye layer by expanding ψ in the form $\psi = \psi_0^{(d)} + \lambda\psi_1^{(d)} + \cdots$, substituting into (3.18)-(3.20) and taking the leading order terms. This results in the following problem for $\psi_0^{(d)}$

$$\frac{\partial^2\psi_0^{(d)}}{\partial\zeta^2} = (e^{\psi_0^{(d)}} - e^{-\psi_0^{(d)}}), \tag{3.21}$$

$$\left.\frac{\partial\psi_0^{(d)}}{\partial\zeta}\right|_{\zeta=0} = -B, \qquad \text{and} \qquad \frac{\partial\psi_0^{(d)}}{\partial\zeta} \to 0 \quad \text{as} \quad \zeta \to +\infty. \tag{3.22}$$

This, as is well-known, has the solution

$$\psi_0^{(d)} = \begin{cases} 2\log_e\left(\coth\left[\dfrac{1}{\sqrt{2}}\left(\zeta + \dfrac{1}{\sqrt{2}}\operatorname{arcsinh}\left(\dfrac{2\sqrt{2}}{B}\right)\right)\right]\right) & \text{for} \quad B > 0, \\ 2\log_e\left(\tanh\left[\dfrac{1}{\sqrt{2}}\left(\zeta + \dfrac{1}{\sqrt{2}}\operatorname{arcsinh}\left(-\dfrac{2\sqrt{2}}{B}\right)\right)\right]\right) & \text{for} \quad B < 0. \end{cases} \tag{3.23}$$

Notably this solution has the property that

$$\psi_0^{(d)} \to 0 \quad \text{as} \quad \zeta \to +\infty,$$

and so is uniformly valid for all values of $\xi \in [0, 1)$ or equivalently for $\zeta \in [1/\lambda, 0)$. It follows that we do not need to look for a solution for ψ in an outer region.

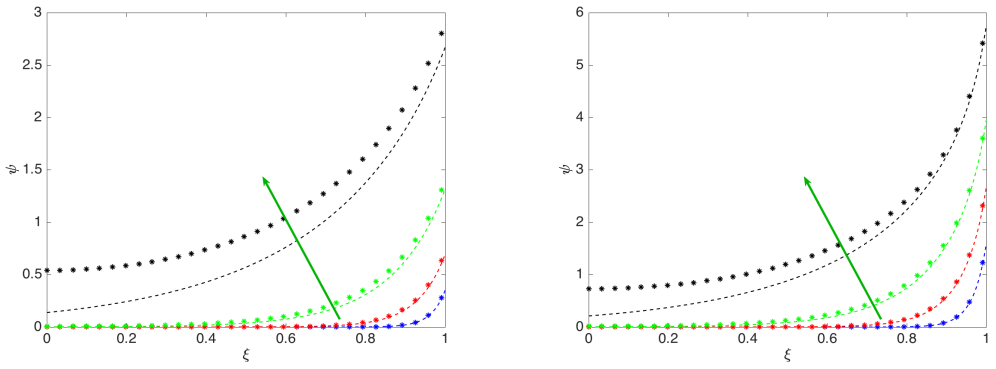

Figure 3.2: Comparison between numerical solution to (3.12) (stars) and its small-λ asymptotic approximation (3.15) (dashed line). Here in the left-hand panel $\beta = 10$ while in the right $\beta = 50$. In both panels the values of λ taken are $\lambda = [0.05, 0.1, 0.2, 0.5]$ and the arrows indicate the direction of increasing λ.

Figure 3.2 illustrates the asymptotic solution as well as the numerical solution of (3.12) for different values of λ and realistic values of $\beta = 10, 50$. In this case the approximation quality, as expected, increases as λ decreases.

3.2.2 Leading order flux conservation and the simplified 1D model

The purpose of this section is to derive flux conservation conditions in the x-direction that will give rise to evolution equations for $Q(x,t)$ and $S(x,t)$. Together with the approximations of the previous section, we are then in a position to numerically solve the approximated system. We start by considering the leading order terms in the ion conservation equations (3.5a)-(3.5b), namely

$$\frac{\partial p_0}{\partial t} + \frac{\partial u_{p,0}}{\partial x} + \frac{1}{r}\frac{\partial}{\partial r}(r w_{p,1}) = 0, \tag{3.24}$$

$$\frac{\partial n_0}{\partial t} + \frac{\partial u_{n,0}}{\partial x} + \frac{1}{r}\frac{\partial}{\partial r}(r w_{n,1}) = 0. \tag{3.25}$$

where expressions for $u_{p,0}$ and $u_{n,0}$ are obtained from the leading order expansions of (3.5d) and (3.5e) and are

$$u_{p,0} = -\kappa_p \left(\frac{\partial p_0}{\partial x} + p_0 \frac{\partial \phi_0}{\partial x} \right), \quad \text{and} \quad u_{n,0} = -\kappa_n \left(\frac{\partial n_0}{\partial x} - n_0 \frac{\partial \phi_0}{\partial x} \right). \tag{3.26}$$

The boundary conditions on $w_{p,1}$ and $w_{n,1}$ come from the leading order expansion of (3.5f) and are

$$w_{p,1}|_{r=R(x)} = \left.\frac{dR}{dx}u_{p,0}\right|_{r=R(x)}, \qquad w_{n,1}|_{r=R(x)} = \left.\frac{dR}{dx}u_{n,0}\right|_{r=R(x)}. \tag{3.27}$$

Multiplying both (3.24) and (3.25) by r and integrating between $r = 0$ and $r = R(x)$ gives

$$\int_0^{R(x)} \left(\frac{\partial p_0}{\partial t} + \frac{\partial u_{p,0}}{\partial x}\right) r dr + [r w_{p,1}]_{r=0}^{R(x)} = 0,$$
$$\int_0^{R(x)} \left(\frac{\partial n_0}{\partial t} + \frac{\partial u_{n,0}}{\partial x}\right) r dr + [r w_{n,1}]_{r=0}^{R(x)} = 0.$$

On applying the boundary conditions (3.27) it can be seen that these equations can be rewritten in conservation form

$$\frac{\partial}{\partial t}\left(\int_0^{R(x)} r p_0(r,x,t) dr\right) + \frac{\partial}{\partial x}\left(\int_0^{R(x)} r u_{p,0} dr\right) = 0, \tag{3.29a}$$
$$\frac{\partial}{\partial t}\left(\int_0^{R(x)} r n_0(r,x,t) dr\right) + \frac{\partial}{\partial x}\left(\int_0^{R(x)} r u_{n,0} dr\right) = 0. \tag{3.29b}$$

Substituting for $p_0(r,x,t)$ and $n_0(r,x,t)$ from (3.9) and $u_{p,0}$ and $u_{n,0}$ from (3.26) leads to an alternative reformulation

$$\frac{\partial}{\partial t}\left(S(x,t)\Theta_1(x,t)\right) = \kappa_p \frac{\partial}{\partial x}\left(\frac{\partial S}{\partial x}\Theta_1(x,t)\right), \tag{3.30a}$$
$$\frac{\partial}{\partial t}\left(Q(x,t)\Theta_2(x,t)\right) = \kappa_n \frac{\partial}{\partial x}\left(\frac{\partial Q}{\partial x}\Theta_2(x,t)\right), \tag{3.30b}$$

where

$$\Theta_1(x,t) = \pi \int_{r=0}^{R(x)} r \exp(-\phi_0(r,x,t)) dr \quad \text{and} \tag{3.31a}$$
$$\Theta_2(x,t) = \pi \int_{r=0}^{R(x)} r \exp(\phi_0(r,x,t)) dr. \tag{3.31b}$$

On substituting for ϕ_0 and r, in terms of ψ and ξ, from (3.11) we can rewrite these expressions in the form

$$\Theta_1(x,t) = A(x)\left(\frac{Q(x,t)}{S(x,t)}\right)^{1/2} G_1(x,t) \quad \text{and} \tag{3.32a}$$

$$\Theta_2(x,t) = A(x)\left(\frac{S(x,t)}{Q(x,t)}\right)^{1/2} G_2(x,t), \tag{3.32b}$$

where $A(x) = \pi R^2(x)$ is the cross-sectional area of the pore and the functions G_1 and G_2 are defined by

$$G_1(x,t) = \int_{\xi=0}^{1} \xi \exp\left(-\psi\left(\xi;\lambda(x,t),\beta(x)\right)\right) d\xi, \tag{3.33a}$$

$$G_2(x,t) = \int_{\xi=0}^{1} \xi \exp\left(\psi\left(\xi;\lambda(x,t),\beta(x)\right)\right) d\xi. \tag{3.33b}$$

Here $\lambda(x,t)$ and $\beta(x)$ are defined in (3.13). Notably since $\psi(x,t)$ satisfies the problem (3.12a)-(3.12b) we can show (by multiplying (3.12a) by $\xi\lambda^2(x,t)$, integrating between $\xi = 0$ and 1 and imposing the boundary conditions (3.12b)) that

$$G_2(x,t) - G_1(x,t) = \lambda^2(x,t)\beta(x). \tag{3.34}$$

The leading order current flowing through the pore can be calculated from (3.7), (3.9), (3.26) and (3.31b) and is

$$\mathcal{J} \sim -\kappa_p \frac{\partial S}{\partial x}\Theta_1 + \kappa_n \frac{\partial Q}{\partial x}\Theta_2. \tag{3.35}$$

or equivalently, on referring to (3.32b),

$$\mathcal{J} \sim A(x)(SQ)^{1/2}\left(\kappa_n G_2 \frac{\partial}{\partial x}\log_e Q - \kappa_p G_1 \frac{\partial}{\partial x}\log_e S\right). \tag{3.36}$$

As mentioned in the introduction, the most commonly available data from nanopore experiments are IV curves. Thus equation (3.35) (and (3.36)) allow us to compute the IV curves very efficiently, without solving a non-linear Poisson equation (as it is the case in the classical Scharfetter–Gummel iteration for PNP, [62]). From the computational point of view this is the main advantage of our approach.

Approximations of $G_1(x,t)$ and $G_2(x,t)$ for $\beta \gg 1$ and $\lambda = O(1)$. In this instance we can find asymptotic expressions for G_1 and G_2 simply by substituting (3.15), the large β asymptotic expression for ψ, directly into (3.33a)-(3.33b) to

obtain

$$G_1(x,t) \sim \frac{1}{48\lambda^2(x,t)} \frac{\beta^2(x) + 12\beta(x) + 48}{\beta(x)(\beta(x)+4)}, \quad \text{and} \quad G_2(x,t) \sim \lambda^2(x,t)\beta(x). \tag{3.37}$$

Note that these expressions still satisfy the identity (3.34) asymptotically in the limit $\beta \to \infty$ since $G_1 \ll G_2$. However the asymptotic expansion breaks down for $\lambda \ll 1$, as noted previously, and so we need to obtain alternative expressions for G_1 and G_2 in this limit. Note that the case $\beta \ll -1$ can be solved by setting $u = -\psi$ in equation (3.14) and following the calculations detailed above to obtain approximations for G_1 and G_2.

Approximations of $G_1(x,t)$ and $G_2(x,t)$ for $\lambda \ll 1$. In order to approximate the integrals in (3.33a)-(3.33b) based on the Debye layer solution for ψ in the small λ limit (3.23) we split the integrals up as follows

$$G_1(x,t) = \int_{\xi=0}^{1} \xi d\xi - \int_{\xi=0}^{1} \xi \left(1 - \exp\left(-\psi\left(\xi;\lambda,\beta\right)\right)\right) d\xi,$$
$$G_2(x,t) = \int_{\xi=0}^{1} \xi d\xi - \int_{\xi=0}^{1} \xi \left(\exp\left(\psi\left(\xi;\lambda,\beta\right)\right) - 1\right) d\xi$$

before substituting $\xi = 1 - \lambda\zeta$ and formally taking the limit $\lambda \to 0$ to obtain the following asymptotic expressions

$$G_1 \sim \frac{1}{2} - \lambda \int_{\zeta=0}^{\infty} \left(1 - \exp\left(-\psi_0^{(d)}\right)\right) d\zeta \quad \text{and} \quad G_2 \sim \frac{1}{2} + \lambda \int_{\zeta=0}^{\infty} \left(\exp\left(\psi_0^{(d)}\right) - 1\right) d\zeta.$$

Evaluating these expressions, in the distinguished limit that $B = \lambda\beta = O(1)$, gives the following relations for G_1 and G_2 in the small λ limit

$$G_1 \sim \frac{1}{2} - \lambda \frac{2\sqrt{2}B}{\sqrt{8+B^2}+2\sqrt{2}+B} \quad \text{and} \quad G_2 \sim \frac{1}{2} + \lambda \frac{2\sqrt{2}B}{\sqrt{8+B^2}+2\sqrt{2}-B}. \tag{3.38}$$

In this instance it turns out that these asymptotic expressions for G_1 and G_2, which are formally of the same order, satisfy the condition (3.34) identically. Figure 3.3 shows that by choosing the right cut-off value of λ it is possible to obtain an adequate approximations to G_1 and G_2 for all values of λ provided that β is large. This approximation can be much improved by smoothing between the two asymptotic representations of the solutions, in the limits $\beta \gg 1$ and $\lambda \ll 1$. The smoothed, uniformly valid asymptotic, representation of G_1 is discussed further in Appendix B in [102] and the accuracy of the fit to the numerical solutions for G_1 can be

appreciated by inspecting Figure 3.3. Note that once a good representation of G_1 has been obtained G_2 can be directly evaluated from the relation (3.34).

3.2.3 Summary of the Quasi-1D model

Since the resulting 1D model (comprised of equations (3.9), (3.11)-(3.13), (3.30a)-(3.30b), (3.32b)-(3.33a), (3.34) and (3.38), (3.37) is quite intricate we summarise it in the following paragraph. The leading order ion concentrations and potential are given in terms of the functions $Q(x,t)$, $S(x,t)$ and $\psi(\xi,x,t)$ by the following:

$$n(r,x,t) = (Q(x,t)S(x,t))^{1/2} \exp\left(\psi\left(\frac{r}{R(x)},x,t\right)\right), \tag{3.39a}$$

$$p(r,x,t) = (Q(x,t)S(x,t))^{1/2} \exp\left(-\psi\left(\frac{r}{R(x)},x,t\right)\right), \tag{3.39b}$$

$$\phi(r,x,t) = \frac{1}{2}log(\frac{S(x,t)}{Q(x,t)}) + \psi\left(\frac{r}{R(x)},x,t\right), \tag{3.39c}$$

where $\psi(\xi,x,t)$ satisfies the following series of ODE problems in ξ

$$\frac{1}{\xi}\frac{\partial}{\partial\xi}\left(\xi\frac{\partial\psi}{\partial\xi}\right) = \frac{R^2(x)(Q(x,t)S(x,t))^{1/2}}{\Lambda^2}(e^{\psi}-e^{-\psi}), \tag{3.40a}$$

$$\psi \text{ bounded at } \xi = 0, \text{ and } \frac{\partial\psi}{\partial\xi}\Big|_{\xi=1} = \Upsilon\sigma(x)R(x). \tag{3.40b}$$

In turn the functions $Q(x,t)$ and $S(x,t)$ satisfy the PDEs

$$\frac{\partial}{\partial t}\left((Q(x,t)S(x,t))^{1/2}G_1(x,t)\right) = \frac{\kappa_p}{A(x)}\frac{\partial}{\partial x}\left(A(x)\left(\frac{Q(x,t)}{S(x,t)}\right)^{1/2}G_1(x,t)\frac{\partial S}{\partial x}\right), \tag{3.41a}$$

$$\frac{\partial}{\partial t}\left((Q(x,t)S(x,t))^{1/2}G_2(x,t)\right) = \frac{\kappa_n}{A(x)}\frac{\partial}{\partial x}\left(A(x)\left(\frac{S(x,t)}{Q(x,t)}\right)^{1/2}G_2(x,t)\frac{\partial Q}{\partial x}\right), \tag{3.41b}$$

where $G_2(x,t)$ and $G_1(x,t)$ are given by the expressions

$$G_2(x,t) = G_1(x,t) + \frac{\Lambda^2\Upsilon\sigma(x)}{R(x)(Q(x,t)S(x,t))^{1/2}}, \tag{3.42a}$$

$$G_1(x,t) = \int_0^1 \xi\exp(-\psi(\xi,x,t))d\xi. \tag{3.42b}$$

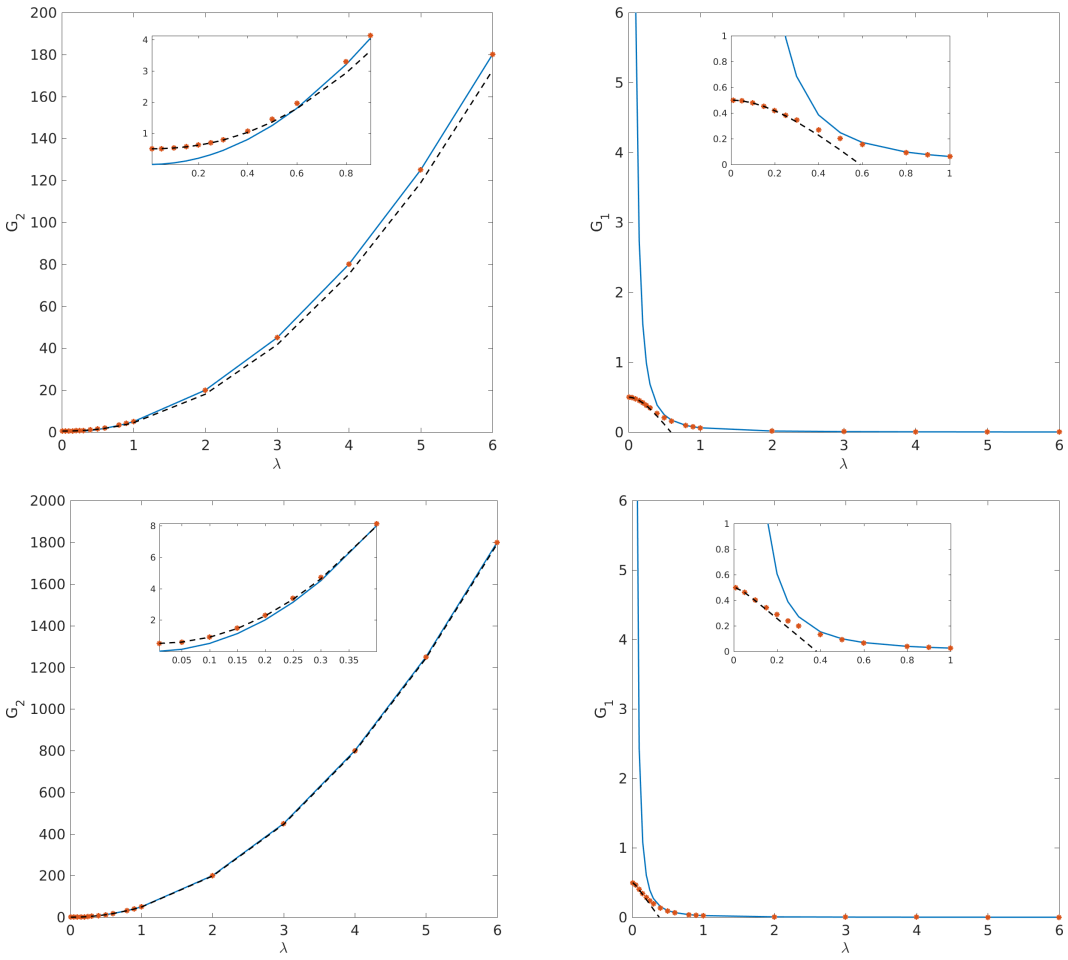

Figure 3.3: Comparison of the numerical evaluation of the expressions G_1 (right) and G_2 (left) as a function of λ for $\beta = 5$ (top row) and $\beta = 50$ (bottom row). Red stars correspond to the values of G_1 and G_2 calculated from the full equations (3.33a)–(3.33b) The blue solid line corresponds to the approximation (3.37) ($\beta \gg 1$) while the black dashed one stands for (3.38) ($\lambda \ll 1$).

The main point of the method is that the integrals G_1 and G_2 are not calculated via integrating the ψ but using the polynomial approximations obtained in the equations (3.38) and (3.37) for different values of the $\lambda(x)$. Thus (3.41a)–(3.41b) are decoupled from (3.40a)–(3.40b). As mentioned in Remark 3.2.2, this is a particular advantage since it allows to calculate the ion current (via (3.36)) without having to solve a nonlinear equation. To ensure a smooth transition between the two regimes a smoothing procedure was implemented as described in detail in the Appendix B in [102], that is by writing

$$G_1(x,t) \approx G_1^{(\text{smooth})}\left(\frac{\Lambda}{R(x)(S(x,t)Q(x,t))^{1/4}}, \Upsilon\sigma(x)R(x)\right) \tag{3.3}$$

where the function $G_1^{(\text{smooth})}(\lambda,\beta)$ is defined in the Appendix A in [102]. This approximation of $G_1(x,t)$ taken together with (3.41a)-(3.42a) allows us to solve a one-dimensional spatial problem for $S(x,t)$ and $Q(x,t)$. If the purpose of the calculation is solely to determine the current I flowing through the pore (for example when calculating I-V curves) this calculation is sufficient since I may be calculated solely from $S(x,t)$, $Q(x,t)$, $G_1(x,t)$ and $G_2(x,t)$ via the formula (3.36), that is by

$$\mathcal{J} = A(x)(SQ)^{1/2}\left(\kappa_n G_2 \frac{\partial}{\partial x}\log_e Q - \kappa_p G_1 \frac{\partial}{\partial x}\log_e S\right). \tag{3.4}$$

If in addition to determining the current flow through the pore we wish also to obtain the spatial distributions of the carrier concentrations and the electric potential we need also to solve for the function $\psi(\xi,x,t)$ in order to use it in (3.39a)-(3.39c) in order to calculate $n(r,x,t)$, $p(r,x,t)$ and $\phi(r,x,t)$. Although it is possible to obtain a reasonable approximation to the function $\psi(\xi,x,t)$ in the large β limit by using the appropriate asymptotic solution, (3.15) for $\lambda = O(1)$ or (3.23) for $\lambda \ll 1$, we instead choose to solve the full boundary value problem for $\psi(\xi,x,t)$ numerically, as specified in (3.12a)-(3.12b); that is we solve

$$\frac{1}{\xi}\frac{\partial}{\partial\xi}\left(\xi\frac{\partial\psi}{\partial\xi}\right) = \frac{R^2(x)(S(x,t)Q(x,t))^{1/2}}{\Lambda^2}(e^{\psi}-e^{-\psi}), \tag{3.5a}$$

$$\psi \text{ bounded at } \xi = 0, \text{ and } \left.\frac{\partial\psi}{\partial\xi}\right|_{\xi=1} = \Upsilon\sigma(x)R(x), \tag{3.5b}$$

for each position x and time t. We adopt this numerically costly procedure here because it provides more accurate asymptotic representations of $n(r,x,t)$, $p(r,x,t)$ and $\phi(r,x,t)$ with which to compare to the full 2D numerical solutions (see figures 3.6, 3.7, 3.10 and 3.11). We do however believe that it should be possible to obtain a uniformly valid asymptotic expansion for $\psi(\xi,x,t)$ in the large β limit that is capable of accurately capturing the solution for all values of λ, much as we do for G_1 in Appendix B in [102].

3.2.4 An alternative formulation.

It is possible to reformulate the Quasi One-1D PNP Model derived in section 3.2.1-3.2.2 and contained in (3.30a)-(3.33b) in more physically appealing forms. We give one such reformulation below but note that there are others.

We start by noting that the (dimensionless) electrochemical potentials of positive and negative ions, μ_p and μ_n respectively, are

$$\mu_p = \log_e p + \phi, \quad \text{and} \quad \mu_n = \log_e n - \phi. \tag{3.6}$$

The chemical potential of the electrolyte, defined by $\mu_e = \frac{1}{2}(\mu_p + \mu_n) = \frac{1}{2}\log_e(np)$, is obtained at leading order by substituting the approximations to n and p found in (3.9) into this expression; this gives

$$\mu_e(x,t) \approx \log_B\left((Q(x,t)S(x,t))^{1/2}\right). \tag{3.7}$$

In addition we define an effective electric potential $\widetilde{\Phi}$ by

$$\widetilde{\Phi}(x,t) = \log_e\left(\left(\frac{S(x,t)}{Q(x,t)}\right)^{1/2}\right). \tag{3.8}$$

We now introduce two further quantities $\bar{P}$ and $\bar{N}$, the cross-sectionally averaged ion densities, as defined by

$$\bar{P}(x,t) = \frac{\pi}{A(x)}\int_0^{R(x)} r p_0 dr \quad \text{and} \quad \bar{N}(x,t) = \frac{\pi}{A(x)}\int_0^{R(x)} r n_0 dr. \tag{3.9}$$

Substituting for n_0 and p_0 from (3.9), and making use of the definitions (3.31b), allows us to re-express these quantities in the form

$$\bar{P}(x,t) = \frac{S(x,t)\Theta_1(x,t)}{A(x)}, \quad \text{and} \quad \bar{N}(x,t) = \frac{Q(x,t)\Theta_2(x,t)}{A(x)}. \tag{3.10}$$

In turn substituting for Θ_1 and Θ_2 from (3.32b), and using the formula (3.7) to eliminate Q and S, allows us to rewrite $\bar{P}$ and $\bar{N}$ as follows:

$$\bar{P}(x,t) = \exp(\mu_e) G_1(\mu_e; x), \quad \bar{N}(x,t) = \exp(\mu_e) G_2(\mu_e; x). \tag{3.11}$$

In the above we have written both G_1 and G_2 in a form that makes it explicit that these quantities are independent of $\widetilde{\Phi}$ and depend only on Q and S through $\mu_e(x,t)$. On using the definitions (3.7) and (3.8) to eliminate Q and S and (3.10) to eliminate Θ_1 and Θ_2 the governing evolution equations (3.30a)-(3.30b) can be rewritten in the intuitively appealing form

$$\frac{\partial}{\partial t}\left(A(x)\bar{P}\right) + \frac{\partial}{\partial x}\left(A(x)\bar{J}_p\right) = 0, \quad \text{where} \quad \bar{J}_p = -\kappa_p \bar{P} \frac{\partial}{\partial x}\left(\mu_e + \widetilde{\Phi}\right), \tag{3.12a}$$

$$\frac{\partial}{\partial t}\left(A(x)\bar{N}\right) + \frac{\partial}{\partial x}\left(A(x)\bar{J}_n\right) = 0, \quad \text{where} \quad \bar{J}_n = -\kappa_n \bar{N} \frac{\partial}{\partial x}\left(\mu_e - \widetilde{\Phi}\right). \tag{3.12b}$$

Furthermore, λ can be expressed in terms of μ_e as follows

$$\lambda = \frac{\Lambda}{R} e^{-\mu_e/4}.$$

Thus the reformulation of the Quasi-1D PNP model consists of a straightforward method for evaluating the two functional dependence of $G_1(\mu_e; x)$ and $G_2(\mu_e; x)$ on μ_e and x (contained in (3.12a)-(3.13) and (3.33a)-(3.33b)) and the two coupled parabolic PDEs for μ_e and $\widetilde{\Phi}$, (3.11)-(3.12b). A further simplification can be obtained from (3.34), the relation between G_1 and G_2, from which we can deduce the local charge neutrality condition

$$A(x)(\bar{P} - \bar{N}) + \Sigma_l(x) = 0, \qquad \Sigma_l(x) = \Lambda^2 \Upsilon(2\pi R(x)\sigma(x)). \tag{3.13}$$

Here $\Sigma_l(x)$ represents the fixed charge per unit length (in appropriate dimensionless form) on the wall of the pore. In effect this relation means that we only need to calculate one of the expressions $G_1(\mu_e; x)$ or $G_2(\mu_e; x)$, use this to determine either $\bar{P}$ or $\bar{N}$ from (3.11), and evaluate the other from the relation (3.13).

Calculating the steady state solution In practice we are usually only interested in the steady state solution to (3.11)-(3.12b). Neglecting the time derivatives in (3.12a)-(3.12b), summing the two equations and taking their difference yields to

the following two equations

$$\frac{\partial}{\partial x}\left(A(x)\left((\bar{N}+\bar{P})\frac{\partial \mu_e}{\partial x}-(\bar{N}-\bar{P})\frac{\partial \widetilde{\Phi}}{\partial x}\right)\right) = 0,$$
$$\frac{\partial}{\partial x}\left(A(x)\left((\bar{N}-\bar{P})\frac{\partial \mu_e}{\partial x}-(\bar{N}+\bar{P})\frac{\partial \widetilde{\Phi}}{\partial x}\right)\right) = 0.$$

We now write

$$\bar{N}+\bar{P} = e^{\mu_e}\hat{\Psi}(\mu_e;x), \quad \text{where} \quad \hat{\Psi}(\mu_e;x) = G_1+G_2 = \int_0^1 \xi\left(e^{\psi}-e^{-\psi}\right)d\xi. \tag{3.14}$$

and substitute for $(\bar{N}-\bar{P})$ from (3.13) in order to obtain two coupled ODEs for μ_e and $\widetilde{\Phi}$

$$\frac{\partial}{\partial x}\left(A(x)e^{\mu_e}\hat{\Psi}(\mu_e;x)\frac{\partial \mu_e}{\partial x}-\Sigma_l(x)\frac{\partial \widetilde{\Phi}}{\partial x}\right) = 0, \tag{3.15a}$$
$$\frac{\partial}{\partial x}\left(\Sigma_l(x)\frac{\partial \mu_e}{\partial x}-A(x)e^{\mu_e}\hat{\Psi}(\mu_e;x)\frac{\partial \widetilde{\Phi}}{\partial x}\right) = 0. \tag{3.15b}$$

Note that the function $\hat{\Psi}(\mu_e;x) = G_1+G_2$ can be obtained either by direct solution for $\psi(\xi;\beta,\lambda)$ from (3.12a)-(3.12b) in which $\lambda = \Lambda e^{-\mu_e/4}/R$, or (in the large β limit) from the uniformly valid asymptotic expression for G_1 discussed in Appendix B in [102].

3.3 Numerical methods and results

In this section we will present numerical methods for both the full 2D PNP system, the 1D Area Averaged PNP system as well as for the asymptotic Quasi-1D PNP model developed in §3.2. They will be used to compare the results for two examples: (I) a trumpet shaped pore (see figures 3.5 & 3.6) and (II) a conical pore geometry (see figures 3.9 & 3.10).

The Quasi-1D PNP solver. The numerical solver of the Quasi-1D PNP is based on the uniformly-valid large β expression for G_1 and on the identity (3.34), relating G_2 to G_1. This thus obviates the need to solve the Poisson equation (3.12a)-(3.12b) for $\psi(\xi,\lambda(x,),\beta(x))$ at every value of x. Instead it only requires the solution of the 1D (stationary) continuity equations (3.30a)-(3.32b) in x. This represents a very considerable reduction in computational complexity and gives a very fast method,

which is particularly suited for the calculation of IV curves. Finally, for an applied voltage above a certain threshold, we introduce a relaxation in the iteration. Once Q and S are known, we use (3.35) to calculate the total current I. The full iterative procedure is detailed in Algorithm 1.

Set $S(x) = p_0(x)/\exp(-\phi_0(x))$, for $x \in \{0, \bar{l}\}$;
Set $Q(x) = n_0(x)/\exp(\phi_0(x))$, for $x \in \{0, \bar{l}\}$;
Initialise $Q^0(x), S^0(x)$;
while $err > \varepsilon$ **and** $max\_iter > m$ **do**
  Calculate $\lambda^m(x)$ using (3.13);
  Calculate $G_1^{m+1}(x)$ and $G_2^{m+1}(x)$ using interpolation between (3.37), (3.38) and (3.42b). ;
  Using $G_1^{m+1}(x)$ and $G_2^{m+1}(x)$ and equations (3.30a)-(3.30b) calculate Q^{m+1}, S^{m+1} ;
  $err = \|Q^{m+1} - Q^m\|_2 + \|S^{m+1} - S^m\|_2$;
  $m = m + 1$;
end
Calculate $\mathcal{J}$ using (3.36)

Algorithm 1: Fixed point scheme to calculate Q and S in the steady state.

The 2D PNP solver. The full 2D steady state PNP system, *i.e.* equations (3.5a)–(3.5h) is solved using a standard $P1$ finite element discretisation and a Scharfetter Gummel iteration, [62]. For both geometries, we use a non-uniform mesh strongly refined at the charged pore walls in order to properly resolve the Debye layers. The meshes are created using Netgen [125], while we use MATLAB to assemble and solve the corresponding discrete systems. We use a similar method to solve the 1D Area Averaged PNP system as described in Section 2.1.

The considered geometry of the testcase pores are depicted in Figure 3.4. In the same Figure, we also present a more realistic geometry, in which additional *bath regions* are attached at each end of the pore.

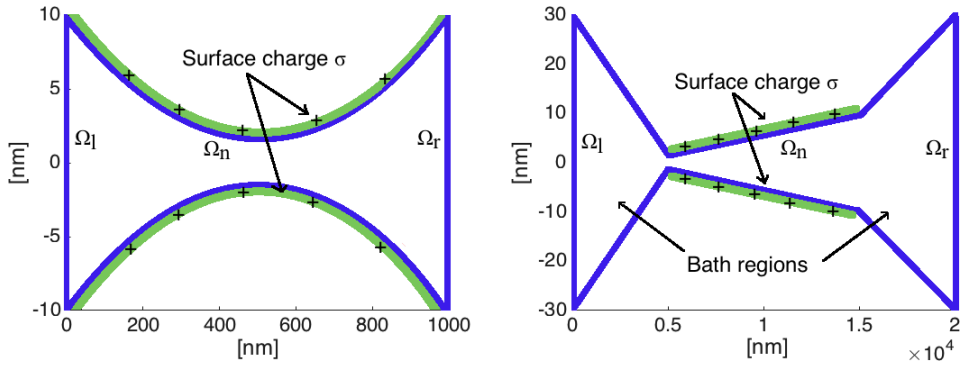

Figure 3.4: Sketches of the geometries considered for the nanopores.

3.3.1 Trumpet shaped pores

We consider a trumpet shaped pore of length 1000nm and a radius varying form 1.5nm to 10nm. The corresponding radius is given by $R(x) = 10^{-6}(34x^2 - 34x + 10)$, where both r and x are measured in units of nanometers, hence the values of λ and β change continuously with respect to x. We set the following parameters:

$$V_{appl} = 0.2\text{V} \text{ and } \quad n_r = n_l = p_r = p_l = 0.1\text{moles/litre} \tag{3.16}$$

$$\text{Surface charge profile} \qquad \sigma = \begin{cases} 1\text{e/nm}^2 & \text{for} \quad 100\text{nm} < x < 900\text{nm} \\ 0\text{e/nm}^2 & \text{for} \quad |x - 500| > 400\text{nm} \end{cases} . \tag{3.17}$$

To obtain accurate and precise results for the 2D solver a mesh of 360000 triangular elements was used. The results of the Quasi-1D and Area Averaged PNP were obtained using a discretization of 1000 intervals. Figure 3.5 and 3.6 show the solutions to the 2D PNP model and the Quasi-1D PNP model, respectively.

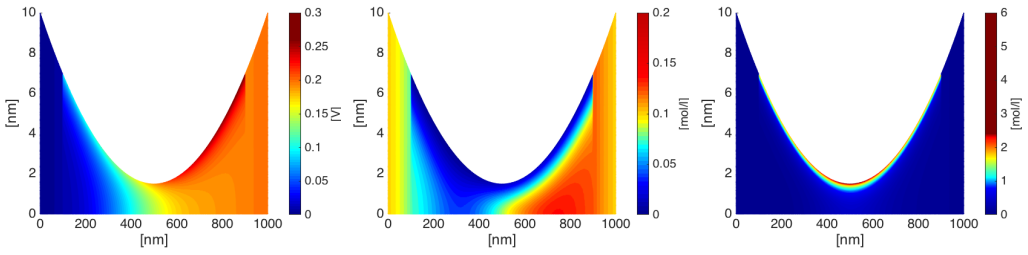

(a) Potential. (b) Positive ions conc. (c) Negative ions conc.

Figure 3.5: Heat maps of the potential and two ionic concentrations obtained using the 2D PNP solver.

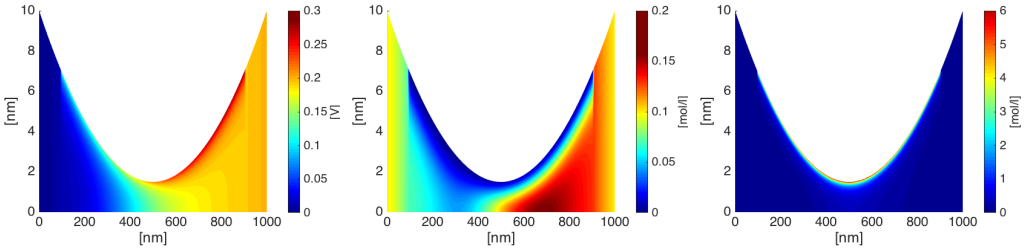

(a) Potential. (b) Positive ions conc. (c) Negative ions conc.

Figure 3.6: Heat maps of the potential and two ionic concentrations obtained using the Quasi-1D PNP solver.

In order to compare the results from the two different methods we plot the cross sectional profiles of the potential and concentrations at $x = 200, 500$ and 800nm in Figure 3.7. We observe that the solution to the Quasi-1D PNP model is a very good match to that of the full 2D PNP equations. This is especially so for the potential (left column) and the negative ions concentration (right column) for which both solutions have almost identical behaviour within the Debye layers.

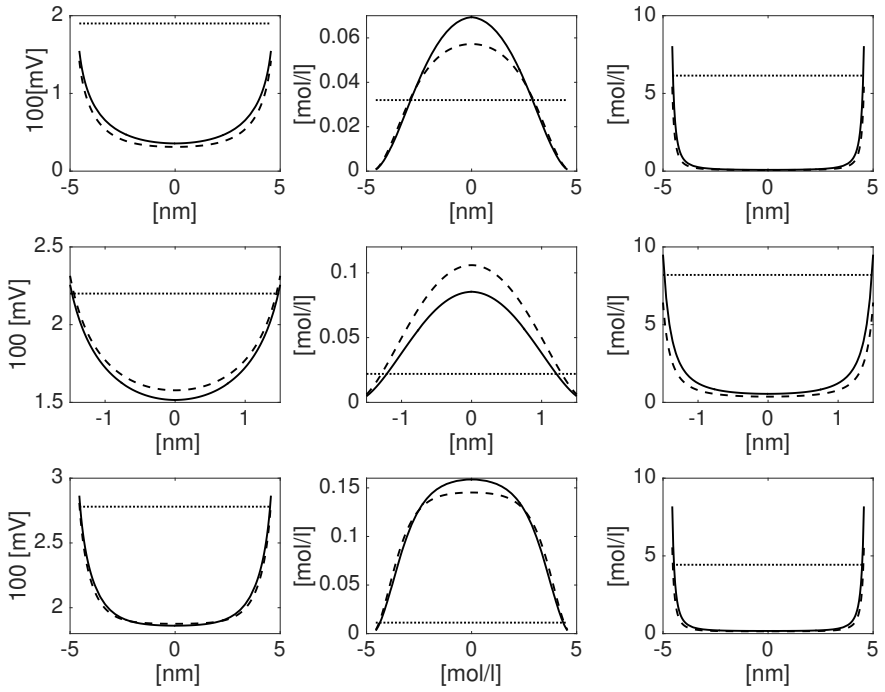

Figure 3.7: Comparison of the potential (left column), positive ions concentrations (centre column) and negative ions concentrations (right column) calculated over the cross-section at $x = 200$nm (top row), $x = 500$nm (middle row) and $x = 800$nm (bottom row), obtained using the 2D finite element solver (solid lines), the 1D Area Averaged PNP (dotted lines) and the Quasi-1D PNP solver described in Algorithm 1 (dashed lines) for a trumpet shaped shape pore of length 1000nm and radius varying from 1.5 to 10nm.

Next we compare the IV curves in the case of different surface charge densities $\sigma = 1$ e/nm^2 and $\sigma = 0.2$ e/nm^2 within the central region of the pore $|x - 500| < 400$nm (we take $\sigma = 0$ outside this region) see Figure 3.8. We observe very good agreement between results from the full 2D PNP model and the Quasi-1D PNP model for both values of the surface charge density. Notably the agreement of the Area Averaged PNP to the full 2D PNP model is much worse than that of the Quasi-1D PNP model.

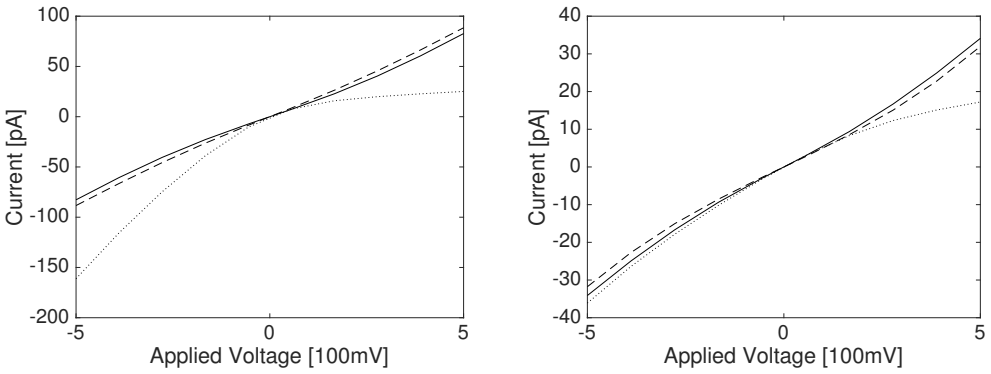

(a) $\sigma = 1$ e/nm^2 (b) $\sigma = 0.2$ e/nm^2

Figure 3.8: IV curves for surface charges $\sigma = 0.2$ e/nm^2 (right plot) and $\sigma = 1$ e/nm^2 (left plot) obtained using the Quasi-1D PNP solver (dashed lines), the 2D PNP solver (straight lines) and 1D Area Averaged PNP method (dotted lines).

3.3.2 Conical Shaped pores

Here, motivated by experimental work on etched pores with conical shape [134], we consider a conically shaped pore of length 10000nm with radius varying between 1.5nm and 10nm (see figures 3.9 & 3.10). This very narrow pore tip is a good model for the tip of a polyethylene terephthalate (PET) nanopore, as used in *et al.* [134]. It is well known that such narrow tips strongly influences the ion transport through the pore [115]. We include two bath regions of 5 μm length each. Here we consider a pore with uniform surface charge density inside the pore which corresponds with 5000nm$< x <$15000nm and zero outside this section. Because of the different length scales and the boundary layer scale we use a highly anisotropic mesh of 7×10^5 triangular elements (calculated using Netgen [125]) refined at the boundary to capture the boundary effects. Figures 3.9 and 3.10 show the results of the full 2D model and those of the Quasi-1D PNP model, respectively. The corresponding cross sectional profiles are depicted in Figure 3.11.

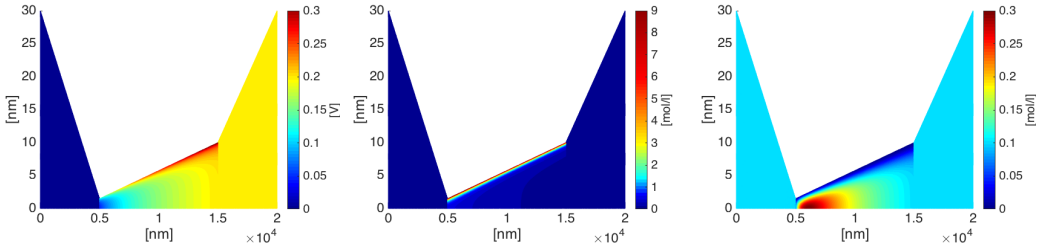

(a) Potential. (b) Negative ions conc. (c) Positive ions conc.

Figure 3.9: Heat maps of the potential and two ionic concentrations obtained using the 2D PNP solver for the conical pore.

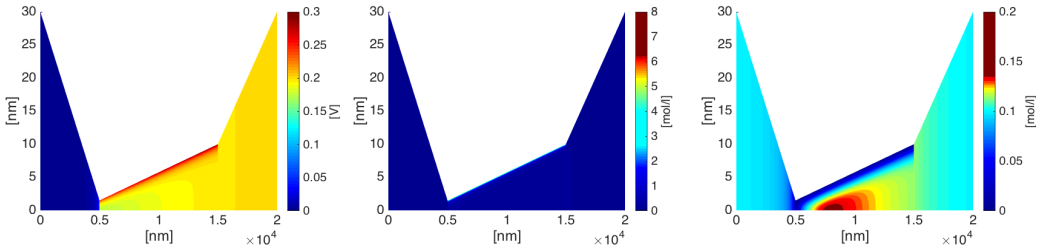

(a) Potential. (b) Negative ions conc. (c) Positive ions conc.

Figure 3.10: Heat maps of the potential and two ionic concentrations obtained using Quasi-1D PNP solver for the conical pore.

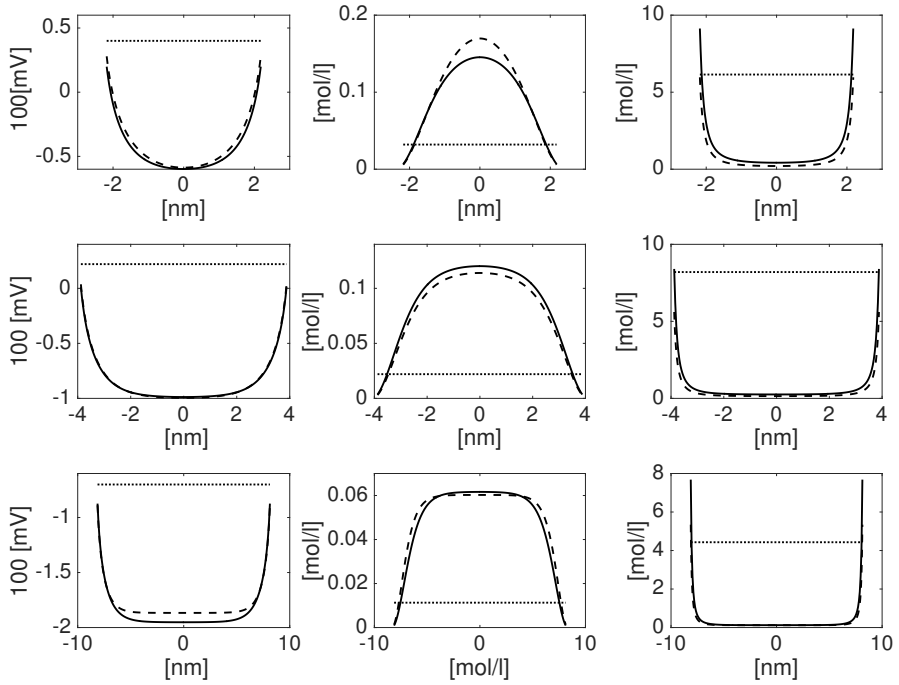

Figure 3.11: The conical pore. Comparison of the potential ϕ (left column), negative ion concentration n (centre column) and positive ion concentration p (right column) calculated over the cross-section at $x = 5800$nm (top row), $x = 7800$nm (middle row) and $x = 12800$nm (bottom row), obtained using the 2D finite element solver (solid lines) the 1D Area Averaged PNP (dotted lines) and the Quasi-1D PNP solver described in Algorithm 1 (dashed lines) for a linear pore of length 10000nm and radius varying from 1.5 to 10nm.

Again we observe very good agreement between the Quasi-1D PNP model solution and the full 2D results close to the charged pore walls. While the discrepancies between the potentials and the negative ions calculated using these two methods are negligible those for the positive ion concentrations are more marked.

Finally Figure 3.12 shows the IV curves obtained from the 2D FEM code, the Quasi-1D PNP solver and the Area Averaged PNP equations. There is much better agreement between the full 2D solver and the Quasi-1D PNP solver than between either of these and the 1D Area Averaged PNP solver (this again overestimates the influence of the geometrical asymmetry of the pore and surface charge influence on the current). Note that the Quasi-1D PNP solver captures the nonlinear IV curve, and the corresponding rectification behaviour, much better than the 1D Area Averaged PNP solver.

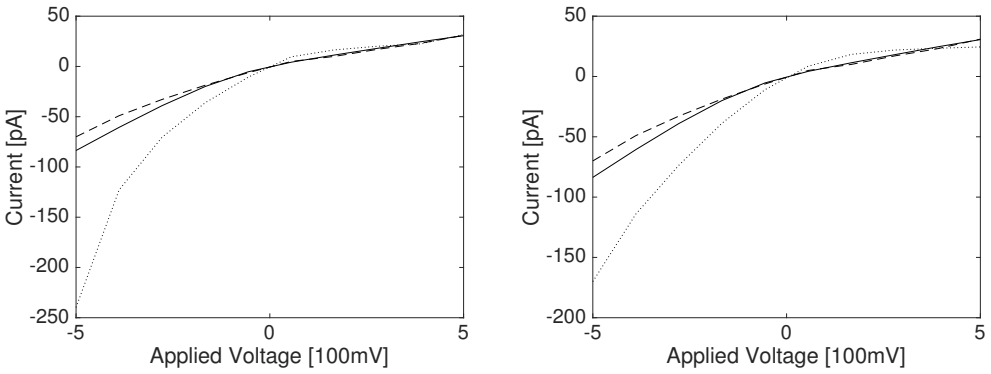

(a) $\sigma = 1$ e/nm^2 (b) $\sigma = 0.2$ e/nm^2

Figure 3.12: IV curves for the conical pore obtained using the surface charges $\sigma = 0.2$ e/nm^2 (right plot) and $\sigma = 1$ e/nm^2 (left plot), in the region 5000nm $< x <$ 15000nm, obtained using the Quasi-1D PNP (dashed lines), 2D PNP solver (solid lines) and 1D Area Averaged PNP method (dotted lines).

3.4 Conclusion

In this work we applied asymptotic methods to a two dimensional Poisson-Nernst-Planck (PNP) model, for the transport processes occurring within a long thin electrolyte filled nanopore with charged walls, in order to systematically derive a reduced order model for ion transport within the nanopore. We term this the Quasi-1D PNP model. In order to investigate the validity of this novel model we conducted numerical experiments on two different nanopore geometries in which we compared results from the Quasi-1D PNP model to solutions of the full two dimensional PNP model, which we solved using a finite element method. In the geometries we considered the comparison between the two approaches was very favourable and furthermore the computational cost of solving the reduced order model was many times less than that for solution of the full 2D model, which requires the use of a very large number of finite elements in order to obtain sufficient accuracy. In addition, we also compared the solution of these two models to the solutions of the one-dimensional Area Averaged PNP equations, which is a commonly used approximation of the PNP model in nanopores, and showed that this model gives a poor representation of the full PNP equations. In this context we also note that the Area Averaged PNP equations are also widely applied to biological ion channels [127; 33] but that no comparison has yet been made between numerical solutions to the PNP equations in 3D and solutions to the 1D Area Averaged equations in an ion channel geometry. Furthermore, given that the Debye length in intra- and extra-cellular fluid ($\approx$0.14

Molar) is around 1.3nm, and that the narrow neck of an ion channel is around 0.4nm (comparable to the Debye length), one might expect that the Quasi-1D PNP provides at least as good an approximation (if not better) to the full 3D PNP as the Area Averaged PNP (which should only be valid if the dimensions of the channels are much smaller than the Debye Length).

The numerical experiments presented here confirm the validity of the assumptions made in the derivation of the Quasi-1D PNP equations. We observe that the method resolves the behaviour of solutions inside the Debye layers correctly and gives substantially better results then the commonly used 1D area averaged approximations. Since surface charge influences the transportation and rectification behaviour of the pore significantly, the correct resolution of the numerical simulations is of great importance. The proposed asymptotics serves as a starting point for further developments in this direction, in particular

- the efficient implementation of a 1D solver to calculate IV curves for nanopores
- the extension of the asymptotic analysis for nonlinear PNP models
- and the comparison on the results with experimental data.

Chapter 4

Asymptotic analysis of a nonlinear Poisson-Nernst-Planck system in radially symmetric pores with surface charge

In this chapter we present work published in [55] tohether with CLemens Ghulke, Ruediger Mueller and Juergen Fuhrmann. We focus on the approximate asymptotic models for the class of the mean field models with linear mobility function which can be reduced to one-dimensional systems. We study three different models starting form the PNP and then Bikerman and DGML as described in Chapter 1. We present different method of the matched asymptotic expansions than the one used in the Chapter 3 to obtain a one dimensional reductions of the model. The method used in this chapter allows us to obtain a model for more general form of the electrochemical potential function. On the other hand the method is presented only for simplified nanopore geometry that does not include the radial symmetry.

In the end of the chapter we present a numerical study where we compare simulation results obtained from solution of the asymptotic 1D-models with those obtained by discretisation of the full resolution models. Moreover, we discuss the influence of the solvation effect on the obtained ionic flow.

4.1 Model description

As it was described in the Chapter 1 the three mean field models can be written in a general framework. We first go through the scaling procedure, as we did in the previous chapter, once again for the convenience of the reader.

$$\partial_{t^*} n_i^* + \nabla \cdot (-\tfrac{D_i^* c_i^*}{k_B T} \nabla \mu_i^e) = 0, \qquad \text{for} \quad i = 1, \dots, m \tag{4.1a}$$

$$-\nabla \cdot (\varepsilon \nabla V^*) = \sum_{i=1}^{N} z_i e_0 n_i^*, \tag{4.1b}$$

$$v_S^* n_S^* = 1 - \sum_{i=1}^{m} v_i^* n_i^*, \tag{4.1c}$$

with the (effective) electrochemical potentials

$$\mu_i^e = \mu_i^0 + z_i e_0 V^* + k_B T \times \begin{cases} \ln \frac{n_i^*}{n} & \text{Nernst–Planck,} \\ \ln \frac{n_i^*}{n_S^*} & \text{Bikerman,} \\ \ln \frac{n_i^*}{n} - \frac{v_i^*}{v_S^*} \ln \frac{n_S^*}{n} & \text{DGLM.} \end{cases} \tag{4.2}$$

where n_S denotes the concentration of the solvent. The next step is to introduce scaling by

$$x^* = \bar{L} x, \quad r^* = R(x) \bar{R} r, \quad n_i^* = \bar{n} n_i, \quad \sigma^* = \bar{\sigma} \sigma, \quad V^* = \frac{e}{k_B T} \phi,$$
$$\mu_i^* = k_B T \mu_i, \quad D_i^* = \frac{L^2}{\bar{t}} D_i, \quad \sigma = \frac{\varepsilon k_B T}{e R} \sigma,$$

which as in the previous section leads to

$$\widetilde{\lambda} := \sqrt{\frac{\varepsilon k_B T}{e_0^2 \bar{n} \bar{L}^2}} \quad \text{and} \quad \widetilde{\delta} := \frac{\bar{R}}{\bar{L}}. \tag{4.3}$$

The first constant is related to the Debye-length $\widetilde{\lambda} L$, that characterise the width of the electrical double layer at charged pore walls. The second constant is the aspect ratio of the pore. Both constants appear quadratic in the dimensionless system.

A nanopore filled with aqueous electrolyte is characterised by these scaling

quantities

$$\bar{t} = 1\text{s}, \qquad \bar{L} = 10^{-5}\text{m}, \qquad \bar{R} = 10^{-9}\text{m}, \tag{4.4}$$

$$\bar{n} = 1\text{mol/L}, \qquad T = 300\text{K}. \tag{4.5}$$

These values imply for the dimensionless constants

$$\widetilde{\lambda} \approx 10^{-8} \quad \text{and} \quad \widetilde{\delta} \approx 10^{-8}. \tag{4.6}$$

For diffusion coefficients and the surface charges in the range of

$$D_i = 10^{-9}\frac{\text{m}^2}{\text{s}} \quad \text{and} \quad \sigma = 10^{-1}\frac{\text{C}}{\text{m}^2}, \tag{4.7}$$

the corresponding dimensionless quantities are of order one. This motivates a second rescaling of the variables where now we introduce a small parameter $\varepsilon \approx 10^{-8}$ and the substitutions

$$\widetilde{\lambda}^2 = \varepsilon\lambda^2 \quad \text{and} \quad \widetilde{\delta}^2 = \varepsilon\delta^2, \tag{4.8}$$

such that now λ^2 and δ^2 are of of order $\mathcal{O}(1)$. Writing down the entire model in dimensionless quantities leads to

$$\partial_t n_i - D_i\big(\partial_x - \tfrac{R'}{R} r\partial_r\big)\big(n_i\partial_x\mu_i^e - n_i\tfrac{R'}{R} r\partial_r\mu_i^e\big) - \tfrac{1}{\varepsilon}\tfrac{D_i}{\delta^2 R^2}\partial_r(c_i\partial_r\mu_i^e) = 0, \tag{4.9a}$$

$$-\lambda^2\varepsilon(\partial_x - \tfrac{R'}{R} r\partial_r)(\partial_x\phi - \tfrac{R'}{R} r\partial_r\phi) + \tfrac{\lambda^2}{\delta^2 R^2}\partial_{rr}\phi = \sum_{i=1}^{m} z_i n_i, \tag{4.9b}$$

$$\upsilon_S n_S = 1 - \sum_{i=1}^{m} \upsilon_i n_i. \tag{4.9c}$$

The dimensionless electrochemical potentials are define as

$$\mu_\alpha^e = \widetilde{\mu}_\alpha^{ref} + z_\alpha\varphi + \begin{cases} \ln\frac{n_i}{n} & \text{Nernst–Planck,} \\ \ln\frac{n_\alpha}{n_S} & \text{Bikerman,} \\ \ln\frac{n_\alpha}{n} - \frac{\upsilon_i}{\upsilon_S}\ln\frac{n_S}{n} & \text{DGLM.} \end{cases} \tag{4.10}$$

The dimensionless boundary conditions at the pore wall and the symmetry axis are

$$-D_i n_\alpha \big(\partial_r \mu_i^e - R' R\varepsilon\delta^2(\partial_x - \tfrac{R'}{R}\partial_r)\mu_i^e\big)|_{r=1} = 0, \qquad \partial_r n_i|_{r=0} = 0, \tag{4.11a}$$

$$\tfrac{1}{\sqrt{\varepsilon\delta^2(R')^2+1}}\big(\tfrac{1}{R}\partial_r\varphi - \delta^2\varepsilon R'(\partial_x - \tfrac{R'}{R}\partial_r)\varphi\big)|_{r=1} = \sigma, \qquad \partial_r\varphi|_{r=0} = 0. \tag{4.11b}$$

4.1.1 Derivation of an asymptotic model

In this section we discuss a leading order problem in terms of ε that must be solved both in x and r direction. In order to find an asymptotic solution of system (4.9a)-(4.11) in the limit $\varepsilon \to 0$, and with all other parameters of size $\mathcal{O}(1)$, we assume the existence of expansions of the form

$$\phi = \phi^{(0)}(r,x,t) + \varepsilon\,\phi^{(1)}(r,x,t) + \varepsilon^2\,\phi^{(2)}(r,x,t) + \cdots, \tag{4.12a}$$

$$n_i = c_i^{(0)}(r,x,t) + \varepsilon\, n_i^{(1)}(r,x,t) + \varepsilon^2\, n_i^{(2)}(r,x,t) + \cdots, \tag{4.12b}$$

$$\mu_i^e = \mu_i^{\mathrm{e},(0)}(r,x,t) + \varepsilon\,\mu_i^{\mathrm{e},(1)}(r,x,t) + \varepsilon^2\,\mu_i^{\mathrm{e},(2)}(r,x,t) + \cdots. \tag{4.12c}$$

These expansions are entered into the equations and boundary conditions. Then, the terms are sorted with respect to their polynomial order in ε. In the following we focus on the first order approximations of the equations and match the respective order in considered equations. For the simplicity of the presentation, we omit the superscripts $^{(0)}$, that are referring to the order in the expansion.

Leading order equations for the cross-sections. Introducing the expansions (4.12) into (4.9a)-(4.11) provides us with the first order approximations (and dropping the ^{0} superscripts) of the the system which read

$$\partial_r \mu_i^e = 0, \qquad \text{for} \qquad i = 1,\dots,N \tag{4.13a}$$

$$-\tfrac{\lambda^2}{\delta^2 R^2}\partial_{rr}\phi = \sum_{i=1}^N z_i c_i, \tag{4.13b}$$

$$\upsilon_S n_S = 1 - \sum_{i=1}^N \upsilon_i c_i. \tag{4.13c}$$

The boundary conditions simplify to

$$\partial_r \mu_i^e|_{r=1} = 0, \qquad \partial_r c_i|_{r=0} = 0, \tag{4.14a}$$

$$\partial_r \phi|_{r=1} = R\sigma, \qquad \partial_r \phi|_{r=0} = 0. \tag{4.14b}$$

Leading order equations for the averaged ion concentrations. In the following, we indicate quantities that are averaged over the r-coordinate by a superscript bar, i.e. for a generic function u the corresponding averaged quantity is $\bar{u} = \int_0^1 u\, dr$. The integration of the system (4.13) in r-direction leads to the leading order system for the averaged number densities,

$$\partial_t \bar{n}_i - \tfrac{D_i}{R} \partial_x (R\, \bar{n}_i\, \partial_x \bar{\mu}_i^e) = 0, \qquad i = 1, \dots, N, \tag{4.15a}$$

$$-\tfrac{\lambda^2}{\delta^2 R} \sigma = \sum_{i=1}^{N} z_i \bar{c}_i, \tag{4.15b}$$

$$\upsilon_S \bar{n}_S = 1 - \sum_{i=1}^{N} \upsilon_i \bar{c}_i. \tag{4.15c}$$

For the derivation we used the boundary conditions (4.11) and the leading order equations for the cross-section (4.13).

4.1.2 Reduction to averaged 1D problem

The asymptotic analysis above decouples the fluxes in x and in r direction and thereby splits the full 2D system into two coupled 1D systems. The equation system (4.15a)–(4.15c) determines the evolution of the averaged number densities along the nanopore and the equation system (4.13a)–(4.13c) determines the specific ion concentration profiles in each cross-section of the nanopore. A similar coupled 1+1D system for the rotational symmetric case is the basis for the quasi-1D PNP model developed in [102]. In the following we derive a reduction from the asymptotic 1+1D system to a single 1D system, that is also applicable for the Bikerman and in the DGLM model.

Exact solution in the cross-section. At first we integrate the inner equations (4.13a) for $i = 1, \dots, N$, as well as for $i = S$, to get implicit representations of the mole fractions, that reads

$$c_i = c_i^0 \exp(-z_i(\phi - \phi^0)) \times \begin{cases} 1 & \text{Nernst–Planck,} \\ \frac{c_S}{c_S^0} & \text{Bikerman,} \\ \left(\frac{c_S}{c_S^0}\right)^{\upsilon_i/\upsilon_S} & \text{DGLM.} \end{cases} \tag{4.16}$$

Here the c_i^0 and ϕ^0 denotes mole fractions and potentials at $r = 0$ respectively. The mole fraction of the solvent is given by,

$$c_S = 1 - \sum_{i=1,\dots,N} c_i, \tag{4.17}$$

and the total number density n can be then determined using the equation (4.13c). Form the equations (4.16) and (4.13c) we conclude that the number densities n_i can be expressed as functions of the electric potential ϕ and the number densities n_i^0 and electric potential ϕ^0.

Multiplication of the Poisson equation (4.15b) by $\partial_r\phi$ yields

$$-\tfrac{\lambda^2}{2\delta^2 R^2}\partial_r(\partial_r\phi)^2 = \Big(\sum_{i=1}^{N} z_i n_i\Big)\partial_r\phi. \tag{4.18}$$

In the Nernst–Planck case, the right hand side of (4.18) can be expressed as the r derivative of a function that depends on $\phi - \phi^0$ and n_i^0. For Bikerman and DGLM, we differentiate (4.17) with respect to r and by use of (4.16) and (4.13c) we get the identity

$$\tfrac{1}{\upsilon_S}\partial_r \ln(c_S) = \Big(\sum_{i=1}^{N} z_i n_i\Big)\partial_r\phi.$$

We use the identity to replace the free charge density in equation (4.18) by the r-derivative of $\ln(c_S)$. This allows us to integrate the Poisson equation to obtain a relation between the r- derivative of the electric potential and the mole fraction of the solvent.

$$\partial_r\phi = \operatorname{sgn}(\sigma) R\tfrac{\sqrt{2}\delta}{\lambda}\sqrt{P(\phi - \phi^0, n_1^0, \dots, n_N^0)}, \tag{4.19}$$

where P is defined as

$$P(\phi - \phi^0, n_1^0, \dots, n_N^0) = \begin{cases} \sum_{i=1}^{N} n_i^0 \left(\exp(-z_i(\phi - \phi^0)) - 1\right) & \text{Nernst–Planck,} \\ \frac{1}{\upsilon_S}\ln\left(\frac{n_S^0}{n_S}\right) & \text{Bikerman,} \\ \frac{1}{\upsilon_S}\ln\left(\frac{c_S^0}{c_S}\right) & \text{DGLM.} \end{cases} \tag{4.20}$$

Let ϕ^R denote the electric potential at the pore wall. The relation (4.19) and the boundary conditions (4.14b) relate the potential difference $\phi^R - \phi^0$ to the surface

charge and number densities at $r = 0$,

$$\sigma = \operatorname{sgn}(\sigma)\tfrac{\sqrt{2}\delta}{\lambda}\sqrt{P(\phi^R - \phi^0, n_1^0, \ldots, n_N^0)}. \tag{4.21}$$

The number densities for $i = 1, \ldots, N$, as well as for $i = S$ can now be expressed in terms of P as

$$n_i = n_i^0 \exp(-z_i(\phi - \phi^0)) \times \begin{cases} 1 & \text{Nernst–Planck,} \\ \exp(-\upsilon_i P) & \text{Bikerman,} \\ \dfrac{n}{n^0}\exp(-\upsilon_i P) & \text{DGLM.} \end{cases} \tag{4.22}$$

When evaluating the mean values of the number densities, we use this relation to substitute the integration with respect to r by an integration with respect to ϕ for the averaging. To compensate a singularity in the integral, we average the deviation from the values at the axis, i.e. $\bar{n}_i = n^0 + \overline{n_i - n^0}$, and get

$$\bar{n}_i = n_i^0 + \tfrac{1}{R}\tfrac{\lambda}{\sqrt{2}\delta}\int_0^{\phi^R - \phi^0} \frac{n_i - n_i^0}{\sqrt{P(\widetilde{\phi}, n_1^0, \ldots, n_N^0)}}\, d\widetilde{\phi} \qquad i = 1, \ldots, N. \tag{4.23}$$

As the first order electrochemical potentials are r independent (see equation (4.13a)), the mean chemical potentials for $i = 1, \ldots, N$ are given by their respective values at $r = 0$,

$$\bar{\mu}_i^e = \widetilde{\mu}_i^{ref} + z_i\phi^0 + \begin{cases} \ln\frac{n_i^0}{n_S} & \text{Nernst–Planck,} \\ \ln\frac{n_i^0}{n_S^0} & \text{Bikerman,} \\ \ln\frac{n_i^0}{n^0} - \frac{\upsilon_i}{\upsilon_S}\ln\frac{n_S^0}{n^0} & \text{DGLM.} \end{cases} \tag{4.24}$$

Resulting 1D system and 2D reconstruction. The variables φ^0 and n_α^0 for $\alpha = 1, \ldots, N$, as well as φ^R and $\bar{n}_\alpha$ for $\alpha = 1, \ldots, N$ are determined by a system consisting of one dimensional PDEs in x-direction (4.15a) and (4.15b), and in addition for each point in x the non-linear algebraic equations (4.21) and (4.23). The

system reads

$$\partial_t \bar{n}_\alpha = \tfrac{D_{\alpha\alpha}}{R} \partial_x (R\, \bar{n}_\alpha\, \partial_x \bar{\mu}^e_\alpha) \qquad \alpha = 1, \dots, N, \tag{4.25a}$$

$$-\tfrac{\lambda^2}{\delta^2 R} \sigma = \sum_{\alpha=1}^{N} z_\alpha \bar{n}_\alpha, \tag{4.25b}$$

$$\sigma = \operatorname{sgn}(\sigma) \tfrac{\sqrt{2}\delta}{\lambda} \sqrt{P(\varphi^R - \varphi^0, n_1^0, \dots, n_N^0)}\ .$$

$$\bar{n}_\alpha = n_\alpha^0 + \tfrac{1}{R} \tfrac{\lambda}{\sqrt{2}\delta} \int_0^{\varphi^R - \varphi^0} \frac{n_\alpha - n_\alpha^0}{\sqrt{P(\widetilde{\varphi}, n_1^0, \dots, n_N^0)}}\, d\widetilde{\varphi} \qquad \alpha = 1, \dots, N,$$

For the averaged potentials $\bar{\mu}^e_\alpha$ (4.24) is applied. To get n_S^0, (4.13c) is used,

$$\upsilon_S n_S^0 = 1 - \sum_{\alpha=1}^{N} \upsilon_\alpha n_\alpha^0. \tag{4.26}$$

In the Nernst–Planck case the function P is explicitly determined by (4.20) as a function of n_α^0 and φ^0. In contrast for the Bikerman and DGML model P is implicitly determined by equation

$$n_S + \sum_{\alpha=1}^{N} n_\alpha = n,$$

together with the representation (4.22) of the number densities.

Finally, a 2D solution can be recovered in a post processing step. Given the solution φ^0, φ^R and n_α^0, we use (4.13b) to determine φ in all of Ω, i.e.

$$-\tfrac{\lambda^2}{\delta^2 R^2} \partial_{rr} \varphi = \sum_{\alpha=1}^{N} z_\alpha n_\alpha(\varphi, P), \tag{4.27a}$$

$$\varphi|_{r=0} = \varphi^0, \qquad \varphi|_{r=R} = \varphi^R, \tag{4.27b}$$

$$n(\varphi, P) = \sum_{\alpha=1}^{N} n_\alpha(\varphi, P) + n_S(\varphi, P), \tag{4.27c}$$

$$1 = \sum_{\alpha=1}^{N} \upsilon_\alpha n_\alpha(\varphi, P) + \upsilon_S n_S(\varphi, P), \tag{4.27d}$$

where we again use the representation (4.22) for n_α.

4.2 Numerical results

In this section we present numerical study focused on two questions:

- How accurate is the 1D-method derived in the Section 4.1.2 in comparison with the solution of the 2D model?
- What is the influence of the different solvation models as discussed in previous sections?

To answer these questions we study two, experimentally driven, pore examples: (i) a trumpet shaped pore and (ii) a conical pore geometry which are shown in Fig. 3.4. We consider a binary electrolyte consisting only of the solvent and – for simplicity – monovalent anions and cations and use the indices $\alpha \in \{A, C\}$ instead of $\alpha \in \{1, 2\}$ for referencing the ionic species. Further we assume that the number of solvent molecules in the solvation shell of the ions is equal. We refer to the solvation shell number as κ. The atomic masses and the specific volume of the ions are given by the simple relation

$$m_\alpha = (1 + \kappa)m_S \quad \text{and} \quad \upsilon_\alpha = (1 + \kappa)\upsilon_S \quad \text{for} \quad \alpha = A, C.$$

By this assumption the mass-volume-ratio of all constituents is equal and the constraint (4.26) is satisfied.

4.2.1 Comparison 1D and 2D model

In this section we compare the 1D and 2D solutions for discussed models. We focus on the results for the DGLM model with $\kappa = 0$ and with $\kappa = 10$. The case $\kappa = 0$ coincides with the Bikerman model where the solvation effect is not present. We also compared the 1D and 2D results from the Nernst–Planck model and found only minor differences compared to the Bikerman ($\kappa = 0$) case. Therefore we omit these results here. For comparison reasons we use similar, in terms of geometry, boundary concentrations, applies voltage and surface charge distributions; test cases as we did in the Chapter 3, that is parabolic and conical shape with attached bath regions.

The computations are performed with the parameters given in Table 4.1. On the left and the right domain boundary the surface charge vanishes and the electric potential and the number densities are thus constant in r direction. The prescribed potential difference between the left and the right boundary is denoted by V_{appl} and the number densities on the left and right boundary are set to the values n_{AC}^{bath} that correspond to the bulk concentrations in the baths on both sides of the pore.

Table 4.1: Parameters used in the numerical computations.

$k_B \approx 1.3806488 \times 10^{-23}\,\mathrm{J/K}$	$T = 300\,\mathrm{K}$	
$e \approx 1.602176565 \times 10^{-19}\mathrm{C}$	$\varepsilon_0 \approx 8.85418781762^{-12}\mathrm{C/(V\,m)}$	$\sigma_0 = 1\,e/\mathrm{nm}^2$
$\chi = 77.5$	$z_A = -1$	$z_C = +1$
$(\upsilon_S)^{-1} = 55\,\mathrm{mol/L}$	$V_{appl} = 0.2\,\mathrm{V}$	$n_{A/C}^{\mathrm{bath}} = 0.1\,\mathrm{mol/L}$

Numerical methods For the 1D problem, we use a P1 finite element method for the stationary version of (4.25a), i.e. we discretise

$$\int_0^L \partial_x \xi \cdot R\,\bar{n}_\alpha\,\partial_x \bar{\mu}_\alpha \,\mathrm{d}x = 0 \qquad \text{for all testfunctions } \xi,$$

where we apply element wise constant approximation of $R\,\bar{n}_\alpha$ by its value in the element mid point. The solution of the approximate model is obtained in two steps. First equation (4.25a) – (4.25b) and (4.24) are solved to obtain the x dependent quantities such as n_0, φ^R and φ^0. For that we use a uniform mesh in x-direction and the integral in (4.23) is approximated by trapezoidal rule with a uniform partition and 500 evaluation points. The resulting non-linear system is solved by Newton's method and implemented for use with GNU Octave and MATLAB. The second step is to recover r dependent quantities n_α and φ. For that the equation (4.27) is solved in a mesh containing 1000 elements using Newton's method.

To solve the full 2D steady state system, we used two different implementations.

On the one hand, a variant of the method described in in [102] applying a standard P1 finite element discretisation and a Gummel iteration, [62] is used to solve the problems for the Bikerman model ($\kappa = 0$). We use non-uniform meshes that are strongly refined at the charged pore walls in order to properly resolve the Debye layers. The meshes are created using Netgen [125], while we use MATLAB to assemble and solve the corresponding discrete systems. Because of the different length scales and the boundary layer scale we use a highly anisotropic mesh of 7×10^5 triangular elements.

On the other hand the method described in [51; 52] is used to solve the problems for the DGLM model ($\kappa = 10$). It is based on a re-formulation of the system in terms of (effective) species activities $a_\alpha = \exp\left(\frac{\mu_\alpha - \frac{m_\alpha}{m_S}\mu_S}{k_B T}\right)$ and a two point flux finite volume method based on a thermodynamically consistent modification of the Scharfetter–Gummel flux [121]. Here, the resulting non-linear systems are solved via Newton iteration and parameter embedding. The discretization meshes are created from an anisotropic rectangular mesh with graded refinement in the

vicinity of the pore wall and subsequent transformation to the pore geometries. The method is implemented within the C++/python based framework pdelib [85].

Solutions from both codes where tested for coincidence for the classical Nernst–Planck and the Bikerman model. As in the previous chapter we consider two types of pore - parabolic and conical shape as it is shown in in Fig. 3.4.

Parabolic shape geometry. The first on is of length $L = 1000$nm and a radius is varying form 1.5nm to 10nm . This pore shape is usually obtained by the double etching technique and due to its symmetry in the x direction shows different behaviour then the more popular conical shaped pore. The pore boundary is given by

$$\frac{R(x)}{\bar{R}} = \big(34\big(\tfrac{x}{L}\big)^2 - 34\tfrac{x}{L} + 10\big),$$

where we chose $R = 1$nm and it is the same pore as considered in the previous chapter. We assume a smooth charge distribution of the form

$$\sigma(x) = \sigma_0 \exp\Big(1 + \frac{(\bar{L})^2}{(2x - \bar{L})^2 - (\bar{L})^2}\Big).$$

The solution of the 1D problem is shown in Fig. 4.1. We observe that on the center line $r = 0$ in x direction the electric potential is not linear but instead but shows a stronger growth on the left side of the pore center at $x = 500$nm and a slower growth to the right of the center. The anions show some accumulation in the middle of the pore where the positive surface charge is the highest. The diffusion of cations from the right to the left side is hindered by the pore resulting in accumulation "before" and depletion "behind" the pore. Fig. 4.2 shows a 2D reconstruction for $\kappa = 10$. We observe a very sharp layer near the charged pore wall where the anions accumulate to compensate the surface charge.

Comparing the solution obtained with the 1D model with the results of the full 2D computations show very good agreement along the center line $r = 0$ and for the potential difference between the pore wall and the center line, cf. Fig. 4.1. A more detailed comparison of the 1D and 2D results and of the impact of the model parameter κ, can be obtained from cross-sections of the (reconstructed 2D) solutions for fixed values of the variable x. In Fig. 4.3, cross-sections are displayed in the pore middle at $x = 500$nm and at some distance to the left and right. Again, we observe perfect agreement between the 1D and 2D solutions over the complete distance of the cross-sections. The potential shows in all cases similar profiles from $r = 0$ to $r = R(x)\bar{R}$ with an increase in the order of 0.08V. At $x = 500$nm we see that, due to the higher concentration at $r = 0$, the anions accumulate very strongly

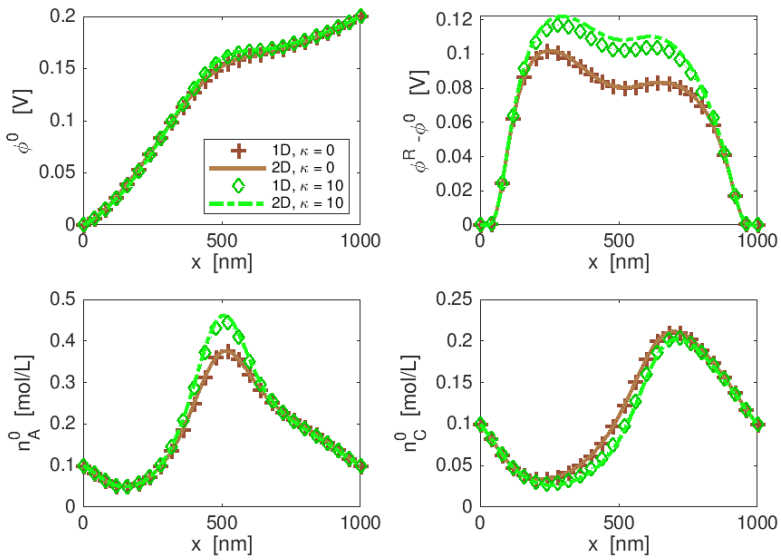

Figure 4.1: Comparison of the 1D and 2D solution for the trumpet shape pore. We observe good agreement between the 1D and 2D solution along the line $r = 0$ (functions $\varphi^0(x)$, $n_A^0(x)$ and $n_C^0(x)$). In addition, $\varphi^0(x) - \varphi^R(x)$ is displayed in the upper right figure to show the agreement between the 1D and the 2D computations on the pore walls.

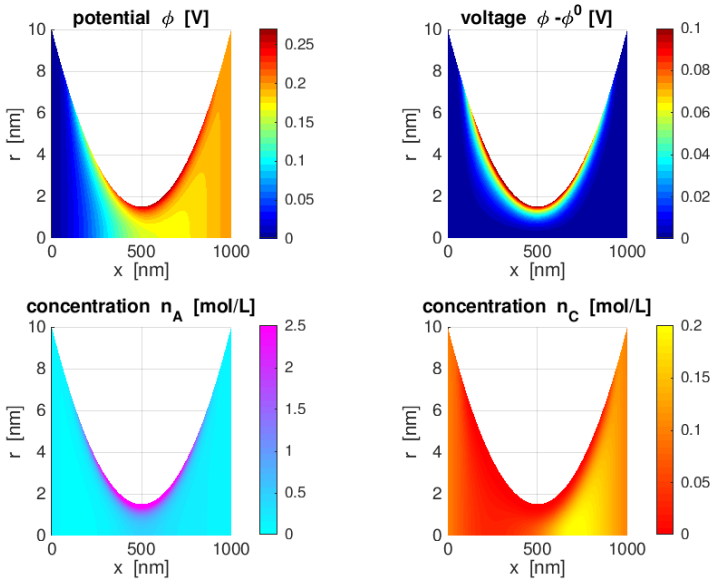

Figure 4.2: Reconstructed 2D solution based on the 1D solution with $\kappa = 10$ from Fig. 4.1. Only the upper half of the symmetric solution is displayed.

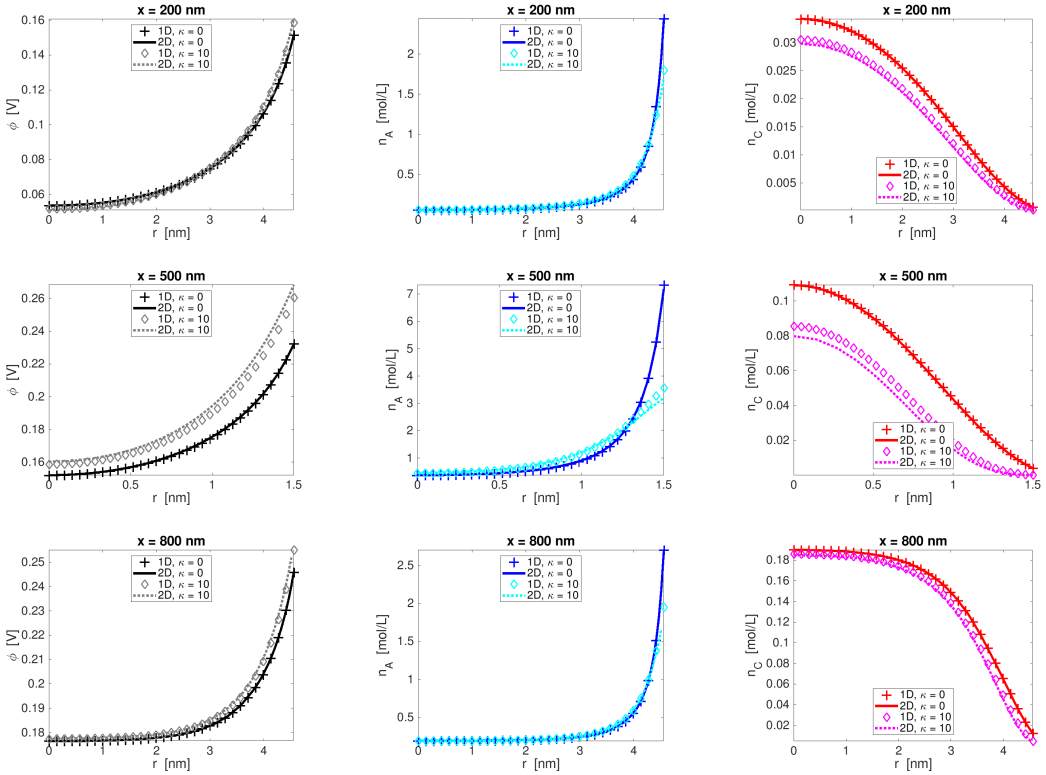

Figure 4.3: Cross sections of the potential for the trumpet shape case together with the number densities at $x = 200$nm (top row), $x = 500$nm (middle row) $x = 800$nm (bottom).

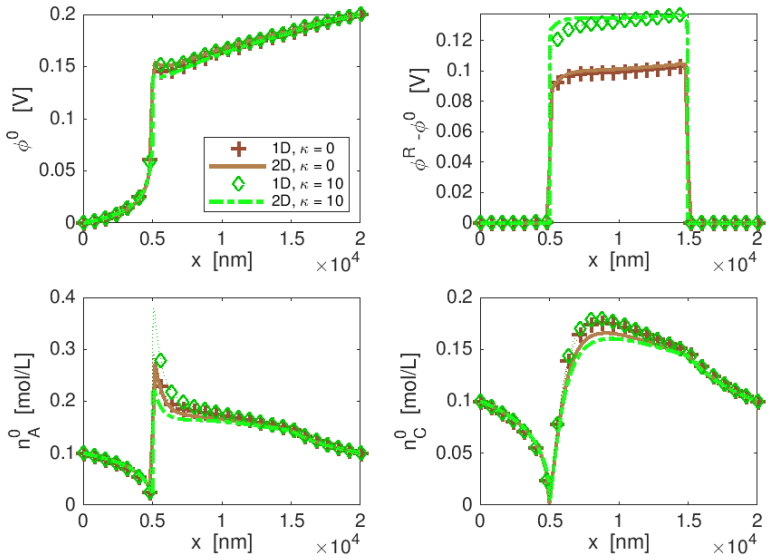

Figure 4.4: Comparison of the 1D and 2D solution for the conical shape pore. The computed 1D solution $\varphi^0(x)$, $n_A^0(x)$ and $n_C^0(x)$ agree with the corresponding 2D solution. In addition, $\varphi^0(x) - \varphi^R(x)$ is displayed in the upper right figure and also shows agreement between the 1D and the 2D computations.

in front of the charged pore wall, reaching a concentration of 7mol/L for $\kappa = 0$. For $\kappa = 10$ the anion concentration is significant lower at $n_A \approx 3.5$mol/L what is still considerably lower than the saturation limit of 5mol/L for this case. The cations are repelled from the positively charged wall, leading to similar profiles with respect to r, only starting from a significantly higher level for $x = 800$nm.

Conical shape geometry. Motivated by experimental work on pores with conical shape obtained using the etching technique, we consider a conically shaped pore of length $\bar{L} = 10000$nm with radius varying between 1.5nm and 10nm which corresponds with the polyethylene terephthalate (PET) nanopore, as used by Siwy [134]. It is well known that such narrow tips strongly influences the ion transport through the pore [115]. We include two bath regions of 5000nm length each. The computational domain is thus described by

$$\frac{R(x)}{\bar{R}} = \begin{cases} -28\left(\frac{2x-\bar{L}}{\bar{L}}\right) + 2 & \text{for } 0 \le \frac{x}{\bar{L}} \le \frac{1}{2}, \\ 8\left(\frac{2x-\bar{L}}{2\bar{L}}\right) + 2 & \text{for } \frac{1}{2} \le \frac{x}{\bar{L}} \le \frac{3}{2}, \\ 20\left(\frac{2x-3\bar{L}}{\bar{L}}\right) + 10 & \text{for } \frac{3}{2} \le \frac{x}{\bar{L}} \le 2. \end{cases} \tag{4.28}$$

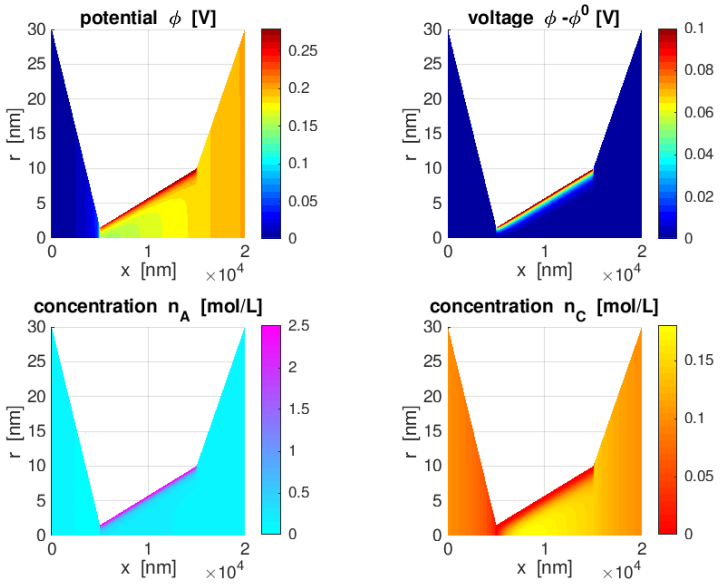

Figure 4.5: Reconstructed 2D solution based on the 1D solution with $\kappa = 10$ from Fig. 4.4. Only the upper half of the symmetric solution is displayed.

We consider a pore with surface charge density inside the pore which corresponds with 5000nm $< x <$ 15000nm and zero outside this section.

$$\sigma(x) = \sigma_0 \left(\tfrac{1}{2} + \tfrac{1}{2}\tanh\left(300\tfrac{2x-\bar{L}}{2\bar{L}}\right)\right)\left(\tfrac{1}{2} + \tfrac{1}{2}\tanh\left(-300\tfrac{2x-3\bar{L}}{2\bar{L}}\right)\right). \tag{4.29}$$

The solution of the 1D problem is shown in Fig. 4.4. We observe a very sharp, step-like transition layer of the electric potential at the narrow opening of the pore at $x = 5000$nm. The potential difference between the pore wall and the center line approaches a plateau inside the pore. The ion concentrations also show the sharp layers at $x = 5000$nm with accumulation on the right side of the narrow opening and depletion to the left. The anions show a sharp peak of the concentration directly right to the narrow opening. Fig. 4.5 shows a 2D reconstruction of the 1D solution for $\kappa = 10$. As in the parabolic case, we observe a very sharp layer near the charged pore wall.

The solutions from the 1D model show to a large extend good agreement with the results from the full 2D computations along the center line $r = 0$, cf. Fig. 4.4. While the potential difference between the pore wall and the center line agrees very well between the 1D and the 2D results, there is some deviation between the values on the center line near the narrow opening of the pore. In particular when looking at $\kappa = 10$, we observe that the peak in n_A^0 is more pronounced in the 1D

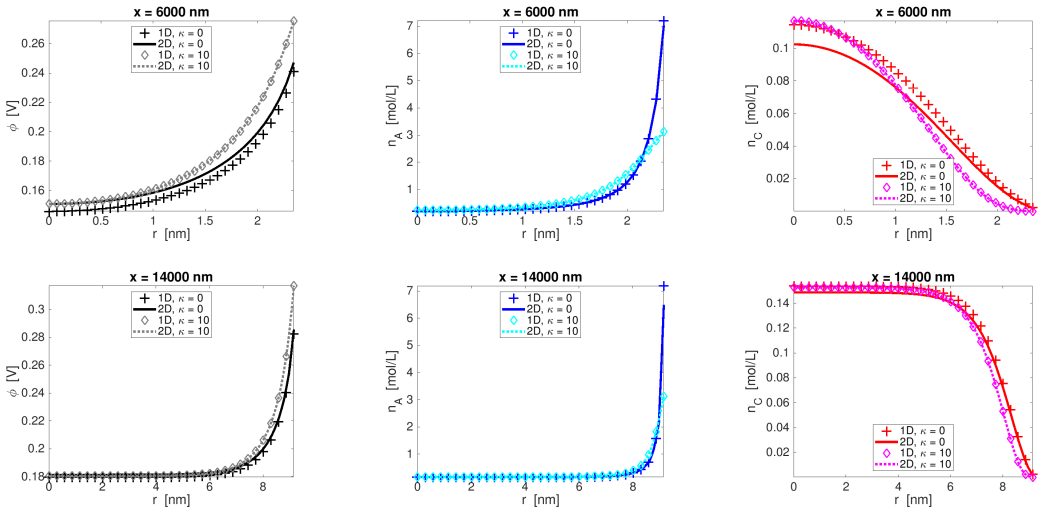

Figure 4.6: Cross sections of the potential for the conical shape case together with the number densities at $x = 6000$nm (top row), $x = 14000$nm (bottom) for the conical pore.

simulations compared to the corresponding full 2D case. This indicates limitations of the asymptotic model in situations where sharp peaks in x direction occur. Cross-sections of the (reconstructed 2D) solutions for fixed x are shown in Fig. 4.6. At $x = 600$nm we again observe the very strong accumulation of anions in front of the charged pore wall, reaching a concentration of 7mol/L for $\kappa = 0$ and $n_A \approx 3.5$mol/L for $\kappa = 10$.

Both examples – trumpet shape and conical pore – have also been solved numerically for the Poisson–Nernst–Planck model. As good agreement between the results from the 1D model and the 2D model was observed and the PNP model has the simplest structure among the models discussed here we do not present obtained results.

4.2.2 Solvation effect study for PNP, Bikerman and DGLM model

The Nernst–Planck model is build on the dilute solution assumption, and therefore is lacking any mechanism for volume exclusion. In the Bikerman model the size exclusion mechanism is introduced but as in the considered test cases the anion accumulation reaches only 7mol/L, whereas the saturation limit in this case is the mole density of the pure solvent (55mol/L), the volume exclusion still has no significant impact on the ion concentration. To reach higher anion concentration and and observe the exclusion effects in the Bikerman model ($\kappa = 0$), it would be necessary to increase the surface charge significantly (although the chosen value of $1e_0/\text{nm}^2$ is

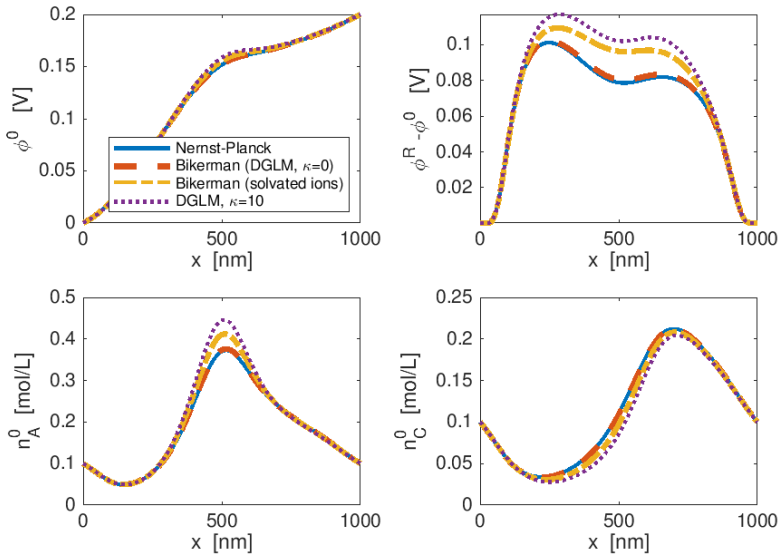

Figure 4.7: Comparison of different electrolyte models for the parabolic shape pore. Solvation effect leads to higher potential differences $\varphi^R - \varphi^0$ between the center line and the wall and stronger anion accumulation on the center line at the narrowest part of the pore.

already high) or consider higher concentrations in the bath regions.

In the profiles of n_A in Fig. 4.3 and Fig. 4.6, we observe that the larger specific volume $v_{A/C}^{ref}$ for $\kappa = 10$ effectively reduces the ion concentration already before getting close to the saturation limit of 5mol/L in this case. Thus it is reasonable to choose the lattice size in the Bikerman model according to the volume of the solvated ions as $(1+\kappa)v_S^{ref}$ and then to compare the results with the DGLM model with the same solvation number.

In the following, we compare only the results of the 1D computations, which already have shown to be in good agreement with the 2D solutions. The computations in this section were again performed using the parameters listed in Table 4.1.

Trumpet shape geometry. For all of the four considered models, the potential φ^0 along the center line at $r = 0$ is very similar, see Fig. 4.7. The largest differences can be observed in the region where the pore is the narrowest. Much more pronounced are the differences between the models for $\varphi^R - \varphi^0$. Here, the models containing solvation effects show a considerably higher potential difference than the Nernst–Planck and the Bikerman model without solvation. Moreover, the different treatment of the solvent causes a larger voltage $\varphi^R - \varphi^0$ in the DGLM model compared to the Bikerman model with solvated ions. The anion concentration n_a^0

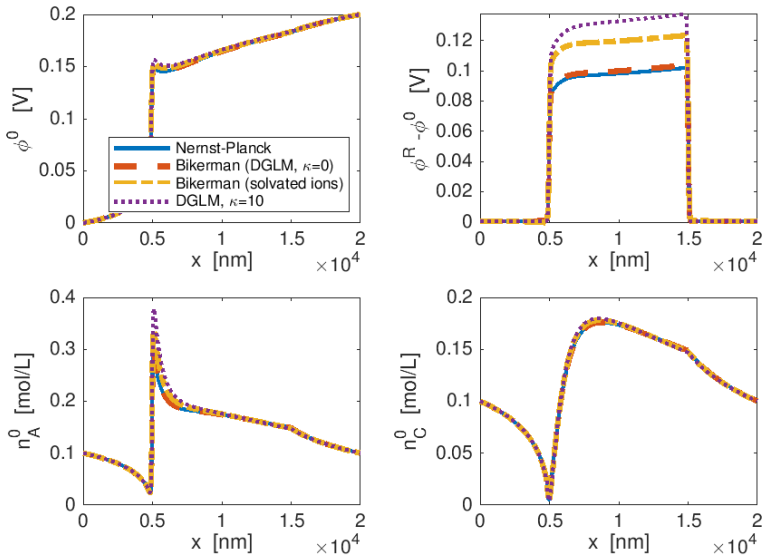

Figure 4.8: Comparison of different electrolyte models for the conical shape pore. Solvation effect leads to higher potential differences $\varphi^R - \varphi^0$ between the center line and the wall and stronger anion accumulation on the center line at the narrowest part of the pore.

along the center line shows a peak at the narrowest part of the pore where the charged pore wall with its adjacent diffuse charge layer gets closest to the center line. The peak height is almost the same for Nernst–Planck and Bikerman with $\kappa = 0$, but is larger for Bikerman with $\kappa = 10$ and is highest for the DGLM model. This higher anion concentration n_A^0 for $\kappa = 10$ is a consequence of the limitation of the space charge due to incompressibility and the large specific volume of the solvated ions which requires a larger boundary layer width to compensate the surface charge of the wall. The Bikerman model without solvated ions gives similar results to the Nernst–Planck as the summarised ion concentration is much smaller then the saturation level at 55mol/L.

Conical shape geometry. For the conical pore, a comparison of the different electrolyte model, see Fig. 4.8, leads to the same conclusions as for the trumped shaped pore above.

The value $\phi^R - \phi^0$ is essentially the zeta potential [82]. As observed above, the introduction of the solvation effect increases the zeta potential. In the absence of the mechanical equilibrium assumption taken for this contribution, according to the Helmholtz-Smoluchowski theory for pores with non-overlapping Debye layers this would lead to a proportionally increased electroosmotic velocity, see also [54]

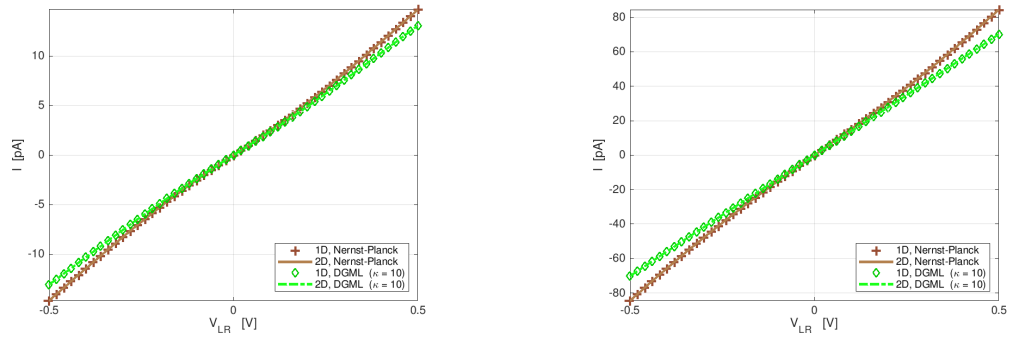

Figure 4.9: Current-voltage curves for the trumpet shape nanopore with bulk salt concentration of 0.1mol/L (left) and 1mol/L (right).

for discussion.

4.2.3 Current-voltage curves

While it is hard to precisely measure the internal structure like geometry and surface charge of nanopores, they can be well characterised by their current-voltage behaviour. Therefore, the stationary electric current flow through a nanopore is recorded for several applied voltages within a large potential range. The resulting current-voltage relation in general depends on the geometry of the pore, the spacial distribution of the surface charge, the ion concentration in the electrolyte bulk. For the accurate numerical simulation of these curves there is in addition the dependency on the applied electrolyte model, in particular, on the solvation model. Of particular interest is the current rectification property of nanopores, i.e. the ratio between the current at applied voltages of the same magnitude but opposite sign [77; 134; 35; 142; 115]. In steady state and for vanishing velocity, for the particles of different masses the current is given by the ion fluxes through an arbitrary cross-section A perpendicular to the pore axis,

$$\mathcal{J} = \int_A \sum_{\alpha=A,C} \frac{z_\alpha e_0}{m_\alpha} J_\alpha \cdot \nu \, da, \tag{4.30}$$

where ν is the normal vector of A pointing into negative x-direction.

Trumpet shape geometry. In Fig. 4.9 the calculated current-voltage curves (IV curve) for low and high ion concentrations are shown for the trumpet shaped nanopore. We first observe that the corresponding 1D and 2D computations show perfect agreement. The IV curves are almost linear, but have a lower slope near

$V_{appl} = 0$V. The symmetry of the IV curves can be attributed to the symmetry of the pore geometry and the surface charge with respect to the midpoint at $x = 500$nm. In particular, we do not observe current rectification. This is consistent with [102], where a pronounced rectification behaviour of a radially symmetric trumpet shaped pore was only obtained by the least accurate area averaged PNP scheme.

Comparison of the Nernst–Planck model and the DGLM model with $\kappa = 10$, shows that the volume exclusion of solvated ions lowers the current and, therefore, increases the electric resistance of the nanopore. In addition to the curves shown in Fig. 4.9, we also calculated IV curves for the Bikerman model without solvation ($\kappa = 0$) which produces results that are visually indistinguishable from the ones of the Nernst-Planck model, and for the Bikerman model with solvation ($\kappa = 10$) which produces IV curves in between those of the Nernst-Planck and the DGML model.

Finally, we observe that increasing the bulk salt concentration from 0.1mol/L to 1mol/L increases the current, but does not change the qualitative behaviour of the IV curves significantly.

Conical shape geometry. When computing IV curves for the conical shape pore and bulk salt concentration of 0.1mol/L, we observe a saturation of the current for absolute values of the applied voltage $|V_{appl}| > 0.2$V, see Fig. 4.10. This behaviour is unexpected and we are not aware of any description of such current saturation in the literature. Nevertheless, it seems very plausible, that this behaviour is related to the depletion of cations in the vicinity of the narrow pore opening, see Fig. 4.4, lower right plot. The IV curves are non-symmetric showing some current rectification behaviour such that the current at $V_{appl} = -0.5$V is about 1.5 times the current at $V_{appl} = 0.5$V.

We observe that the 1D results show good qualitative agreement with the 2D computations but for larger positive or negative applied voltage, some deviations between 1D and 2D solutions become visible. This corresponds to the above mentioned limitations of the 1D method at the narrow opening, where very steep gradients of the ion concentration occur, see Fig. 4.4. As for the trumpet shaped pore, the DGLM model with solvation number $\kappa = 10$, slightly increases the pore resistance, and thus lowers the electric current, compared to the Nernst-Planck model.

The unexpected saturation of the current and the possible explanation by the cation depletion inside the pore at the narrow opening motivated to study the IV curve for the conical pore at higher bulk salt concentration. An increased salt concentration reduces the width of the double layers and thus reduces the overlap of

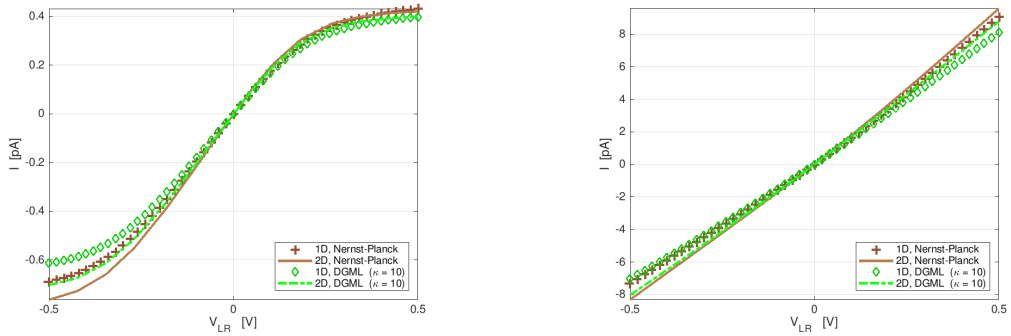

Figure 4.10: Current-voltage curves for the conical shape pore with bulk salt concentration of 0.1mol/L (left) and 1mol/L (right).

layers at the narrow opening. Moreover, the more effective screening of the positive surface charge does not require a depletion of the cations in this region.

We performed the simulation of the IV curves with a bulk salt concentration of 1mol/L, i.e. ten times larger than in the before simulation, and observe that the current saturation has been removed from the IV curves. This supports the above conjecture that the saturation can be attributed to the ion depletion. Similar as for the trumpet shaped nanopore, the shape of the IV curves is almost linear at bulk salt concentration of 1mol/L. We observe only minimal current rectification, such that $|I(+0.5\text{V})/I(+0.5\text{V}) \approx 1.25$ for the Nernst-Planck model and the rectification is about 1.15 for the DGLM model with $\kappa = 10$.

4.3 Conclusions and discussion

The asymptotic analysis used in this paper leads to quasi-equilibrium conditions governing the system in the cross-sections perpendicular to the pore axes. This allows the effective dimension reduction of the model to a one dimensional situation by the use of implicit representations that are known for equilibrium solutions. This procedure can be applied for a variety of material models for the electrolyte: to the classical PNP model, but also – for the first time – to models containing volume exclusion effects like the Bikerman model and to models that in addition take solvation effects into account.

The numerical study demonstrates that the asymptotic 1D models can approximate the results of the full 2D models very closely, but at a considerably lower computational cost. In steady state, the profile of the electric potential and the ion distribution can be accurately reproduced by the dimension reduced asymptotic models. We observe differences between the different electrolyte models. In general,

volume exclusion effects limit the charge accumulation in front of the charged wall. Nevertheless, going from the PNP model to the Bikerman model where the particle volume is given by the number density of the pure solvent, i.e. 55mol/L, we observe almost no difference in the counter ion accumulation in front of the charged wall. This result might seem surprising at the first sight, and it seems to suggests that the simpler PNP model without volume exclusion effects might be preferable over more complex models like Bikerman or DGLM. But, one has to notice that the maximal archived number density is only about 7mol/L and thus too low for the volume exclusion mechanism to get relevant. Given realistic values of the surface charge, in the range of $1e_0/\mathrm{nm}^2$ that we used here, therefore sufficiently large complexes like solvated ions are needed in order for the volume exclusion to have a visible effect. Then, the resulting ion distribution shows considerably less steep concentration gradients but also results in higher potential differences between the pore wall and the center line of the pore. In further extended models, which take electro-osmotic flow into account, cf. [54], this wider spreading of charge in the boundary layers can be expected to cause an increase of the flow velocity and thereby might contribute to the total current flow through the pore.

In the example of the conical pore, we can guess the limits of the asymptotic method. The narrow width of the pore, together with the abrupt change of geometry and surface charge, leads to very strong gradients in the electric potential and the ion concentrations. These quantities can become of order ε^{-1} and start contributing to the leading order equations of (4.9a). Then, the decoupling of the fluxes into the different coordinate directions is no longer possible, requiring a full 2D model.

We used a 2D approximation of the geometry for the asymptotic analysis, where the third coordinate is ignored. In case of rotational symmetric nanopores cylinder coordinates could be used. But this leads to asymptotic models which dependent explicitly on the radial coordinate. This inhibits the calculation of an exact solution of the 1D system for the cross-section problem, and no further reduction to truly one-dimensional system is possible, instead a coupled system for the axial and radial coordinate have to be solved.

The differences between the IV curves resulting from different electrolyte models are minor under the conditions of the numerical experiment considered here. However, this can change considerably, when electro-osmotic velocities convective transport are no longer ignored or charge macro-molecules like strands of DNA passing the pore, which interact with the charged boundary layers.

This work might be a starting point for further investigation, especially issues such as

- the extension of the asymptotic analysis and dimension reduction to nonlinear electrolyte models for radially symmetrical geometries,
- inclusion of convective transport and electro-osmotic flow inside the pore,
- study the influence of macro molecules crossing the nanopore on the IV characteristic of the pore.

Chapter 5

Application of the Poisson-Nernst-Planck system to model different types of electronic devices

In this chapter, we present application of the mean field theory in modelling nano-electronic devices. We study results of the PNP and the nPNP in comparison to the NP+ LEMC for two different in the current-voltage characteristic devices - diode and transistor. The scope of the chapter is to present application of the mean field theory in modeling of the nano-electronic devices as well as compare it with a mezzo-scale modeling approach such as NP+LEMC. We compare macroscopic quantities such as current-voltage characteristics as well as the microscopic ones i.e. concentration profiles. That provides insight in the phenomena inside the nanopore and can be used to investigate the significance of the omitted in the mean field theory phenomenas such as size exclusion and particle-particle interactions.

5.1 Introduction

As it was described in the Chapter 1 Local equilibrium Monte Carlo method is a multiscale method which combines the continuum equation with Monte Carlo method. Both methods use the Nernst-Planck (NP) transport equation to describe the ionic flux of $i = \{1, 2\}$ species:

$$\mathcal{J}_i = -D_i c_i \nabla \mu_i^e. \tag{5.1}$$

The main difference between the two techniques is that PNP makes use of the Poisson-Boltzmann (PB) theory to relate the concentration profile, c_i, to the electrochemical potential profile, μ_i^e, while the particle simulation method uses the Local Equilibrium Monte Carlo (LEMC) technique [15; 65; 18; 13] to establish this relation. The particle simulation method includes all the ionic correlations that are beyond the mean field approximation applied in PNP. The difference between the two approaches can be quantified by considering the electrochemical potential

$$\mu_i^e = \ln c_i + \mu_i^{\mathrm{EX}}, \tag{5.2}$$

The μ_i^{EX} term is the excess chemical potential that describes all the interactions acting between the particles forming the system and all the interactions with external forces (including an applied electrical potential). PNP defines the excess term as the interaction with the mean electric field produced by all the free charges and induced charges. Thus the electrochemical potential in the case of PNP is

$$\mu_i^{\mathrm{PNP}} = \ln c_i + z_i e V, \tag{5.3}$$

The missing term can be identified with what is beyond mean field (BMF) and quantifies the difference between PNP and a solution that is accurate from the point of view of statistical mechanics:

$$\mu_i^e = \mu_i^{\mathrm{PNP}} + \mu_i^{\mathrm{BMF}}. \tag{5.4}$$

In the implicit solvent framework used here the BMF term includes the volume exclusion effects (hard sphere effects) due to the finite size of the ions and electrostatic correlations that are beyond the mean-field level. This partitioning has been used to study selective adsorption of ions at electrodes [137] and in ion channels [58; 17].

It is also usual to break the electrochemical potential into a chemical and an electrical component that are loosely identified with the chemical and electrical works needed to bring an ion from one medium to the other:

$$\mu_i^e = \mu_i^{\mathrm{chem}} + \mu_i^{\mathrm{el}}, \tag{5.5}$$

where the EL term can be identified with $z_i \frac{e}{k_b T} V$, while the CH term can be identified with $\mu_i^0 + \ln c_i + \mu_i^{\mathrm{BMF}}$. Although these two terms cannot be separated in experiments [8; 11; 48], the separation is possible in computational studies because V can be determined.

In PNP, where $\mu_i^{\mathrm{BMF}} = 0$, the CH term is just $\mu_i^0 + \ln c_i$, the ideal expression

(ID).

In this work, we also use a non-linear variant of PNP as described in Section 1.3.8 that can be derived (formally) from a discrete hopping model [24]. In all these models Eqs. (5.1) and (5.3) are replaced by

$$\mathcal{J}_i^{\mathrm{nPNP}} = -D_i c_i (c_{\max} - c_1 - c_2) \nabla \mu_i^{\mathrm{nPNP}},$$

and

$$\mu_i^{\mathrm{nPNP}} = \mu_i^{\mathrm{PNP}} - \ln(c_{\max} - c_1 - c_2).$$

In this work, we use a two dimensional (2D) PNP (respectively nPNP) model which is a suitable approximation to the three-dimensional (3D), but rotationally symmetric, system studied here. Our simulations, furthermore, include the bulk regions and the access regions at the entrances of the nanopore, as opposed to other studies [144; 140]. Introducing the bath regions into the computational domain is necessary when studying the behaviour of nanoelectronic device.

Summarised, we can couple the NP equation either to LEMC simulations or to the PB theory. The former is referred to as the NP+LEMC technique, while the latter could be termed as NP+PB, but we stay with the usual name, PNP. Poisson's equation is satisfied in both approaches. In PNP, it is solved in every iteration, while it is automatically fulfilled in LEMC because Coulomb's law is used to handle electrostatics in the simulations (including the applied field in the framework of the Induced Charge Computation method [16]). Both approaches provide approximate indirect solutions for the dynamical problem through the NP equation. The main difference between NP+LEMC and PNP is the way they handle the statistical mechanical problem of establishing the closure between c_i and μ_i^e. The NP+LEMC technique provides a solution on the basis of particle simulations that contain all the correlations ignored by PNP. The main goal of our study is to discuss the effects of the approximations applied in PNP for different sets of physical parameters. Comparing to NP+LEMC results makes it possible to focus on the approximations applied in the statistical mechanical part of the PNP theory (the PB theory), because NP is what both models have in common.

Particle simulations are necessary for narrow pores, where ions are crowded and their size and the correlations between them (the BMF term) matter. This is the case in ion channels, where the ions correlate strongly with each other and with the charged amino acids along the ionic pathway. Although nanopores are larger in reality, the electrical double layers formed by the ions at the pore walls overlap if the the Debye length is larger than the pore radius. This occurs if the pore is narrow

enough (such as conical nanopores at their tips) or if the electrolyte is dilute.

The advantage of NP+LEMC over MD is that it is faster and can handle larger systems that are closer to realistic length scales of nano-devices. From this point of view, PNP is even more advantageous, because it does not involve particle simulations, therefore, it can handle even larger systems.

5.2 Nernst-Plank equation coupled to Local Equilibrium Monte Carlo

To solve the NP+LEMC system, an iterative procedure is needed, where μ_i is updated until the continuity equation (Eq. 5.1) is satisfied up to some error. Every iteration contains two different types of steps- LEMC for the electrochemical potential profile, $\mu_i^e[n]$,and NP for the concentration profile, $c_i[n]$, corresponding to is obtained from LEMC simulations. We divide the computational domain (inside the green lines in Fig. 5.1A) into volume elements and assume local equilibrium in these volume elements. We assume that these local equilibria can be characterised by local electrochemical potential values. We also assume that the gradient of the μ_i^e profile defined this way is the driving force of ion transport as described by the NP equation (Eq. 5.1).

The initial step of the procedure is to solve Laplace equation with the Dirichlet boundary condition of Eq. 5.6 for the applied potential field V^{appl}. Then the initial guess for $\mu_i^e[n]$ is set.

The heart of the LEMC simulation is a MC step, where we insert/remove an ion into/from a volume element $\mathcal{B}^k$. The acceptance probability of an insertion is

$$p_{i,\mathrm{INS}}^k = \min\left\{1, \frac{v^k}{N_i^k+1}\exp\left(\frac{-\Delta U^k + \mu_i^{e,k}}{kT}\right)\right\},$$

where v^k is the volume of subsystem $\mathcal{B}^k$, N_i^k is the number of particles of component i in $\mathcal{B}^k$ before insertion, ΔU^k is the energy change associated with the insertion (including the effect of the external field), and $\mu_i^{e,k}$ is the configurational (total minus $\mu_i^{e,0}$) electrochemical potential of component i in $\mathcal{B}^k$. In the particle deletion step we randomly choose a particle of component i in sub-volume $\mathcal{B}^k$ and delete it. The deletion is accepted with probability

$$p_{i,\mathrm{DEL}}^k = \min\left\{1, \frac{N_i^k}{v^k}\exp\left(\frac{-\Delta U^k - \mu_i^{e,k}}{kT}\right)\right\}.$$

Here, N_i^k is the number of particles of component i in sub-volume $\mathcal{B}^k$ before deletion. The energy change ΔU^k consists of the influence of the potential generated by the surrounding ions, that is

$$V^{ION} = \frac{1}{4\pi\varepsilon_0\varepsilon} \sum_k \frac{z_k}{|r - r_k|},$$

as well as the effect of the applied potential V^{appl} calculated in the initial guess. The resulting formula reads

$$\Delta U^k = z_i V^{ION} + z_i V^{APP}.$$

The result of the simulation is the concentration c_i^k in every volume element.

The next step is to solve the NP equation for the sub-volumes which is done using the finite volume method. The values c_i^k and $\mu_i^{e,k}$ are assigned to the centres of the volume elements and so the corresponding profiles are constructed. Both c_i^k and μ_i^k fluctuate during the iteration process, so the final results are obtained as running averages. The resulting procedure can be summarised as

$$\mu_i^e[n] \xrightarrow{\text{LEMC}} c_i[n] \xrightarrow{\text{NP}} \mu_i^e[n+1].$$

The NP+LEMC technique has been applied to study transport through membranes [15; 65] and calcium channels [18; 13].

The electrochemical potential for the next iteration, $\mu_i[n+1]$, is computed from the results of the previous iteration, $c_i[n]$, in a way that they together produce a flux (through the NP equation) that satisfies the continuity equation. Details on the algorithm can be found in the original paper [15].

5.3 Example 1 - Diode

5.3.1 Problem description

We apply our methods to a bipolar nanopore that is a suitable case study for our purpose. Bipolar nanopores have an asymmetrical surface charge distribution on the pore wall changing sign along the central axis of the pore. Pore regions with opposite surface charges can be achieved by chemical modifications. For example, in the case of PET nanopores, carboxyl groups can be transformed into amino groups by a coupling agent [141]. The surface potential can also be regulated similarly to field-effect transistors if the pore walls are made of conducting materials.

The reason of choosing the bipolar nanopore for this comparative work is that the source of rectification in this case is purely electrostatic in nature and thus a robust effect. Therefore, we can afford a short nanopore (only 6 nm in length) that can be handled with LEMC. In the case of conical nanopores, where only a geometrical asymmetry is present, long pores are needed to produce a considerable effect which makes it computationally unfeasible.

Although bipolar nanopores have been studied extensively using PNP [38; 36; 141; 90; 144; 88; 149; 107; 135; 130; 129; 133; 139; 136], we are not aware of any paper, where a direct comparison to particle simulations is discussed.

Water is a continuum background, whose energetic effect is taken into account by a dielectric screening ($\epsilon = 78.5$), while its dynamic effect is included in the diffusion coefficient in the NP equation (D_i in Eq. 5.1). The ions, however are point charges in PNP, while they are hard spheres (of radius 0.3 nm for both ions) with point charges at their centres in LEMC.

The nanopore is a cylinder of 6 nm in length with a varying (between the simulations) radius ($R = 0.5 - 3$ nm). It penetrates a membrane that separates two bulk electrolytes. The walls of the pore and the membrane are hard impenetrable surfaces in the LEMC simulations (Fig. 5.1A), while they are part of the boundaries of the solution domain in the PNP calculations (Fig. 5.1B).

The diffusion coefficient of the ions are set to be smaller inside the pore than outside in the bulk regions. This finding was confirmed by our other study that compares MD and NP+LEMC results [67]. Here, for simplicity, we assigned $D_i^{\text{bulk}} = 1.333 \times 10^{-9}$ m^{2}s^{-1} and $D_i^{\text{pore}} = 1.333 \times 10^{-10}$ m^{2}s^{-1} values in the bulk and in the pore, respectively, for both ions.

The charges on the cylinder's surface are partial point charges in the case of LEMC that are placed on grid points whose average distance is about 0.25 nm. The values of the partial charges depend on the prescribed surface charge density, σ. The surface charge densities are included in PNP through Neumann boundary conditions for the potential.

In LEMC, the electrical potential is also calculated in the interior of the membrane, which cannot be occupied by ions (Fig. 5.1A). The dielectric constant is the same there as in the electrolyte ($\epsilon = 78.5$), therefore, the surface of the membrane is not a dielectric boundary and polarisation charges are not induced there. For the 2D (n)PNP simulations, the computational domain is shown in Fig. 5.1B. In the case of PNP, the interior of the membrane is not part of the computational domain. An appropriate Neumann boundary condition is applied on the surface of the membrane in order to mimic the system used in LEMC. Boundary conditions as handled in the

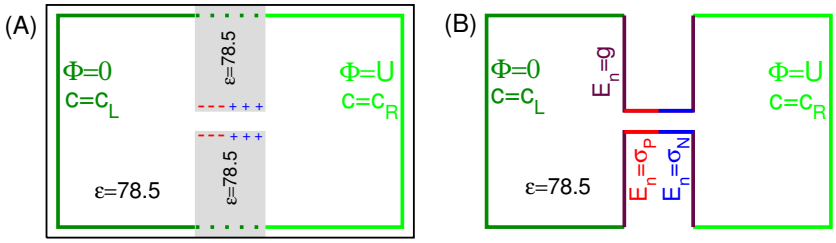

Figure 5.1: Geometry of computation domain (A) in the NP+LEMC system and (B) in the PNP system. (A) Boundary conditions for the NP+LEMC system are prescribed for the two half-cylinders (dark and light green lines, Γ_{L} and Γ_{R} domains) on the two sides of the membrane. Dirichlet boundary conditions are applied by using the appropriate applied potential obtained by solving the Laplace equation (a linear interpolation way used inside the membrane, see the dotted lines). Boundary conditions for the concentrations are ensured by using appropriate electrochemical potentials at the boundaries that correspond to the chemical potentials producing the prescribed concentrations. The domains outside the green lines are in thermodynamic equilibrium, where the chemical potential is constant, so equilibrium GCMC simulations are performed there. Pore charges are free charges present explicitly in the simulation cell. They are placed on the pore wall on a grid as partial point charges. The dielectric constant is the same everywhere, including the interior of the membrane. (B) The PNP computational cell excludes the interior of the membrane from the solution domain. The pore charges are polarisation charges that are induced as a result of the prescribed Neumann boundary conditions on the pore wall (red and blue lines, Γ_{W}). On the surface of the membrane (brown lines, Γ_{M}), a Neumann boundary conditions is applied in order to mimic the NP+LEMC solution. On the two half cylinders, the same boundary conditions are used as in NP+LEMC (Γ_{L} and Γ_{R}).

two methods are detailed in the following subsections.

When investigating our results we first discuss the macroscopic quantities such as ionic current and then discuss the micro-scopic phenomenas such as concentrations and potential fields. This way is driven by the fact that the macroscopic quantities are ones that are physically observable while the microscopic ones are impossible to observe inside the pore.

5.3.2 Poisson-Nernst-Planck simulation setup

The (n)PNP systems are solved inside the computational domain, whose boundary is separated into four parts as shown in Fig. 5.1B. The first two parts correspond to the left and right half-cylinders (dark and light green lines in Fig. 5.1B) and are denoted by Γ_{L} and Γ_{R}. These regions are the same in NP+LEMC. Both the concentration and the applied potential are set using the following boundary conditions

$$
\begin{aligned}
c_i &= c_i^{\mathrm{L}} \quad \text{and} \quad V = 0 \quad \text{on } \Gamma_{\mathrm{L}} \\
c_i &= c_i^{\mathrm{R}} \quad \text{and} \quad V = V^{apl} \quad \text{on } \Gamma_{\mathrm{R}}.
\end{aligned} \tag{5.6}
$$

The third part are the regions of the membrane which are attached to the baths and are denoted by Γ_{M} (brown lines in Fig. 5.1B). As the membrane is impenetrable for the particle flux, we set the flux to be equal to 0 there. In LEMC simulations the membrane is penetrable for the electric field, which is not the case in PNP. Therefore we impose the boundary conditions

$$
\mathcal{J}_i \cdot \boldsymbol{N} = 0 \quad \text{and} \quad \frac{\partial V}{\partial \boldsymbol{N}} = g(r) \quad \text{on } \Gamma_{\mathrm{M}}, \tag{5.7}
$$

where $\boldsymbol{N}$ is the outer normal on Γ_{M} and the function $g(r)$ is supposed to mimic the LEMC case (where there is an electric field across the membrane). More precisely, it is obtained by solving a Laplace equation with zero left hand side without permanent charges and with boundary condition Eq. 5.6 in the domain of Fig. 5.1A. Then, evaluating the normal derivative of this solution at the boundary Γ_{M} yields the function g. This additional Neumann boundary condition matches the value of applied potential crossing the membrane in the LEMC.

The last part of the boundary is on the inside wall of the pore, called Γ_{W}. As it is a part of the membrane, which is impenetrable for the particles, no-flux conditions are also imposed for the current. The permanent charges induce an additional electric field and are included by another Neumann boundary condition:

$$
\mathcal{J}_i \cdot \boldsymbol{N} = 0 \quad \text{and} \quad \frac{\partial V}{\partial \boldsymbol{N}} = \sigma_0(z) \quad \text{on } \Gamma_{\mathrm{W}}, \tag{5.8}
$$

where $\sigma_0 = \sigma$ and $\sigma_0 = -\sigma$ for $z < 0$ and $z > 0$, respectively, and $\mathbf{n}_{\mathrm{W}}$ is the outer normal on Γ_{W}.

To actually solve the 2D (n)PNP system we use the well-known Scharfetter–Gummel scheme which is based on a transformed formulation of the system in exponential variables, see [62] for detail. We use a 2D finite element method for the actual implementation and a triangular mesh containing $20-60$ thousand elements, depending on the radius of the pore. The mesh is also non-uniform in order to obtain high accuracy, especially close to the pore entrances.

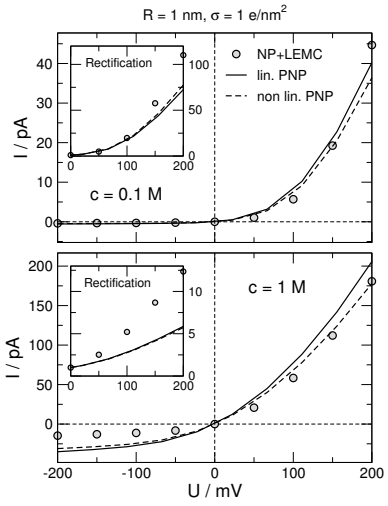

Figure 5.2: Current-voltage curves for concentrations $c = 0.1$ M (top panel) and $c = 1$ M (bottom panel) as obtained from NP+LEMC, PNP, and nPNP (symbols, solid curves, dashed curves, respectively). The insets show rectification as computed from the ratio of the ON and OFF state currents (the absolute values). The model parameters are $R = 1$ nm and $\sigma = 1\ e/\text{nm}^2$.

5.3.3 Results and Discussion

The reference point of all simulations corresponds to the following parameter set: voltages ± 200 mV (200 mV is the ON, while -200 mV is the OFF state of the nanopore), concentrations $c = 0.1$ and 1 M, surface charge $\sigma = 1\ e/\text{nm}^2$, and nanopore radius $R = 1$ nm. Then, we vary the parameters systematically by changing only one and keeping the others fixed. Rectification is defined by $|I(U)/I(-U)|$, i.e. the ratio between the currents in the ON and OFF state, respectively. In our case, this implies that it is always larger than 1. In all figures we plot the NP+LEMC, PNP, and nPNP results with symbols, solid lines, and dashed lines, respectively.

5.3.4 Comparison of I-U curves and rectification behaviour

First, we look at the nanopore as a device that gives an output signal (current) as an answer to the input signal (voltage). The relation of these is the transfer function of the device. Then, we study various profiles (concentration, potential, chemical potential) and try to understand the differences between PNP and NP+LEMC.

Figure 5.2 shows current-voltage (I-U) curves for the two studied concentrations. Rectification is observed using all the three methods: the current is larger at positive voltages than at negative voltages (note that currents are multiplied with -1

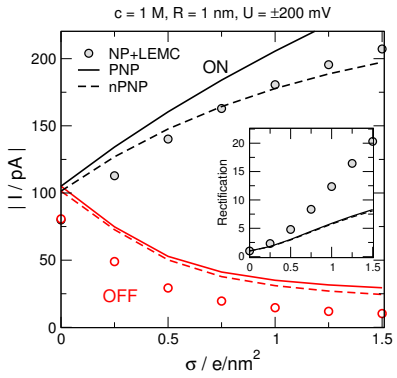

Figure 5.3: The absolute value of the current as a function of σ (characterising the strength of the polarity of the pore) in the ON and OFF states (200 vs. -200 mV, respectively) as obtained from NP+LEMC, PNP, and nPNP (symbols, solid curves, dashed curves, respectively). The inset shows rectification. The model parameters are $c = 1$ M and $R = 1$ nm.

in order to get positive currents for positive voltages). Rectification increases with increasing $|U|$ as shown in the insets. Agreement between NP+LEMC and (n)PNP data is better at low concentration (0.1 M) and smaller voltages as expected. The data from nPNP are slightly better than those from PNP, especially for $c = 1$ M.

The value of the σ parameter can be considered as a measure of the nanopore's polarity. At $\sigma = 0$ e/nm^2, the pore is uncharged and symmetric, so currents at the two voltages of opposite signs are the same and rectification is 1. Figure 5.3 shows current values in the ON and OFF states as functions of σ. As σ is increased, the current increases in the ON state, while decreases in the OFF state. Rectification, therefore, improves as the strength of the polarity of the pore increases. The σ-dependence is described qualitatively by (n)PNP. The errors manifest in the fact that rectification is underestimated by (n)PNP.

One source of the errors is that the effective cross section of the pore through which the centres of ions can move is smaller in the case of the charged hard sphere ions used in LEMC ($R - 0.15$ nm, where 0.15 nm is the ionic radius) than in the case of point ions used in (n)PNP (the whole pore radius, R, is used in (n)PNP). (n)PNP, therefore, systematically overestimates current in both the ON and OFF states as seen in Fig. 5.3. The overestimation of the denominator (OFF current) dominates the ratio. Rectification, therefore, is underestimated.

One way to partially overcome this difference between the two models would be using the effective cross section of the finite ions ($R - 0.15$ nm) in the PNP calculations. In this case, Fig. 5.3 would show better agreement, but cause other problems, such as the presence of ions with different diameters. Therefore, we

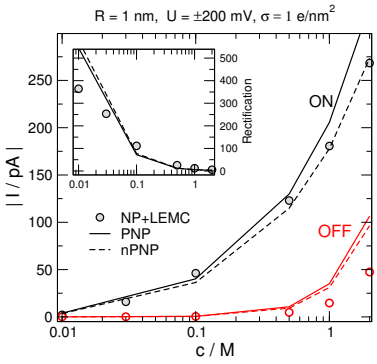

Figure 5.4: The absolute value of the current as a function of the electrolyte concentration in the ON and OFF states (200 vs. −200 mV, respectively) as obtained from NP+LEMC, PNP, and nPNP (symbols, solid curves, dashed curves, respectively). The inset shows rectification. The model parameters are $c = 1$ M and $R = 1$ nm.

decided to keep the pore cross section in PNP in this study as it is (R), but point out the problems with this approach.

Figure 5.4 shows the currents as functions of the electrolyte concentration, c. Currents decrease with decreasing c as expected, but the current decreases faster in the OFF state, so rectification increases with decreasing concentration, a well-known result. The explanation is that depletion zones dominate the currents in bipolar nanopores, but depletion zones are more depleted at low concentrations. Changing the sign of the voltage from positive (ON) to negative (OFF), therefore, can deplete the the depletion zone further more efficiently at low concentrations.

Agreement between NP+LEMC and (n)PNP is better in the ON state. The nonlinear version of PNP works better in this case, because it handles crowding better. In the OFF state, (n)PNP systematically overestimates the current partly from the reason discussed above. Rectification, interestingly, is underestimated by (n)PNP at large, while overestimated at small concentrations.

Finally, we show the dependence of currents on the pore radius in Fig. 5.5. Currents increase with widening pores as expected. The relative difference between the ON and OFF states decreases as R increases. Rectification is the result of the interplay between the effect of pore charges and the applied potential. The average distance of pore charges from the ions increases as R increases, therefore, the pore charges get less and less able to produce the depletion zones inside the pore. (n)PNP qualitatively reproduces the behaviour obtained from NP+LEMC. Also, the systematic underestimation of rectification is present for all pore radii studied.

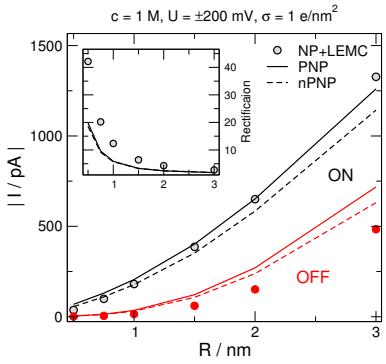

Figure 5.5: The absolute value of the current as a function of the pore radius in the ON and OFF states (200 vs. -200 mV, respectively) as obtained from NP+LEMC, PNP, and nPNP (symbols, solid curves, dashed curves, respectively). The inset shows rectification. The model parameters are $R = 1$ nm and $\sigma = 1$ e/nm^2.

5.3.5 Analysis of profiles for concentration, electrical potential, and electrochemical potential

To get additional insights into the physical mechanisms beyond the device-level behaviour, we also analyze profiles for the concentration, electrical potential, and electrochemical potential.

In Fig. 5.6, we plot the concentration profiles for $c = 1$ (panel A) and 0.1 M (panel B) in order to study the differences between high and low concentrations. This figure shows the results for $\sigma = 1$ e/nm^2. Figure 5.7 shows the same concentration profiles but for $\sigma = 0.25$ e/nm^2.

The curves show that the ions have depletion zones in the middle of the pore and in the zone, where they are the co-ions (having ionic charge with the same sign as the pore charge, σ). We distinguish basically four regions:

1. left bath, near the membrane ($z < -3$ nm)
2. the left part of the pore with positive surface charge ($-3 < z < 0$ nm, N region) – anions the counter-ions, cations the co-ions
3. the right part of the pore with negative surface charge ($0 < z < 3$ nm, P region) – cations the counter-ions, anions the co-ions
4. right bath, near the membrane ($z > 3$ nm)

In the access regions, close to the pore entrances (regions 1 and 4) ionic double layers are formed. Double layer is common name for the separation of cations and anions (polarisation of the ionic distributions) as a response to the presence of a charged

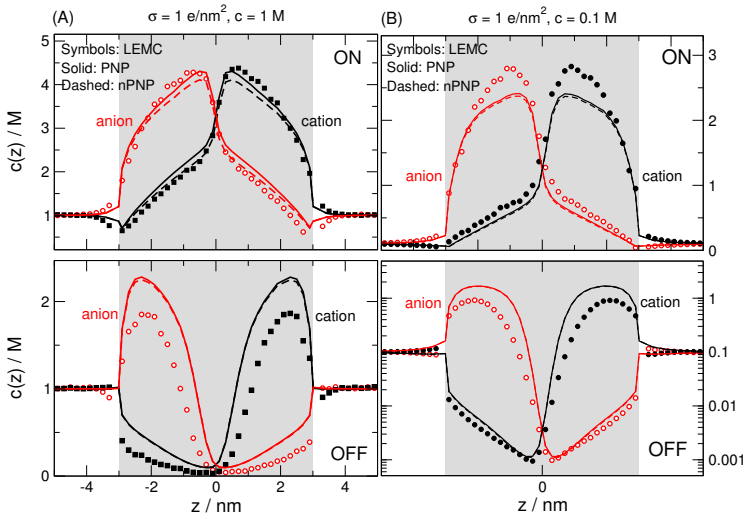

Figure 5.6: Concentration profiles of cations and anions as obtained from NP+LEMC, PNP, and nPNP for (A) $c = 1$ M and (B) $c = 0.1$ M for parameters $R = 1$ and $\sigma = 1$ e/nm^2. These concentration profiles have been computed by taking the average number of ions in a slab and dividing by the available volume. For $-3 < z < 3$ nm, the cross section of the pore was used to obtain this volume in both methods.

or polarised object. In this case, double layers appear partly as a response to the applied field, partly as a response to the charge imbalance inside the pore. Realise that the sign of the double layer (which ions are the co-ions and counter-ions in the double layer) depends on the sign of the applied voltage.

The basic reason of rectification is that the ions are more depleted in their depletion zones in the OFF state than in the ON state; cation concentration in the N zone is lower in the OFF state than in the ON state, for example. Basically, the depletion zones are caused by the pore charges. The applied field modulates the effect of pore charges, therefore, it increases or decreases concentrations compared to the zero-voltage case. Depletion zones are the main determinants of the current, because they are the high-resistance elements of the system modelled as resistors connected in series along the ionic pathway. So, if depletion zones are more depleted, current is reduced.

It is important, however, that not only the co-ion concentrations decrease by switching from ON to OFF, but also the counter-ion concentrations. As a matter of fact, this is crucial, because co-ions are brought into their depletion zones with the help of their strong correlations to counter-ions. So there are less co-ions because there are less counter-ions. The quantity of counter-ions, on the other hand, seems to be related to the double layers at the entrances of the pore on the two sides of

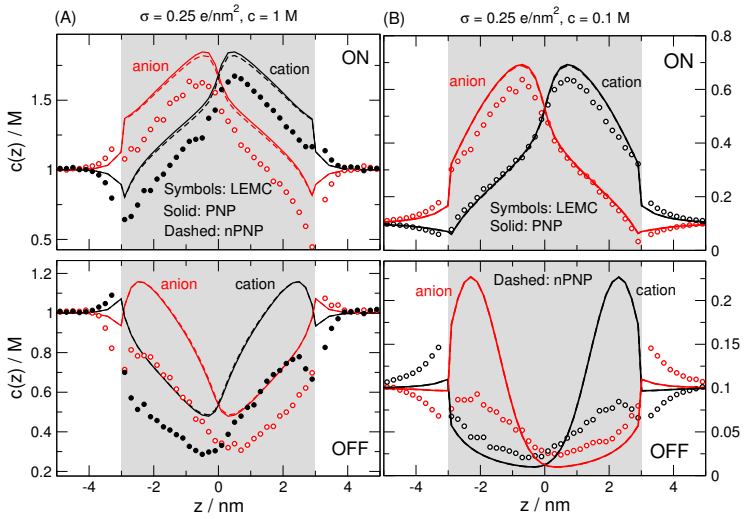

Figure 5.7: Concentration profiles of cations and anions as obtained from NP+LEMC, PNP, and nPNP for (A) $c = 1$ M and (B) $c = 0.1$ M for parameters $R = 1$ and $\sigma = 0.25$ e/nm^2.

the membrane. At least, this seems to be suggested by the results of NP+LEMC.

The double layers have opposite signs in the ON and the OFF states that can be explained through the mean electrical potential profiles that have two components produced by all the free charges, V^{ION}, and induced charges, V^{APP}, in the system. In this study, induced charges appear at the boundaries where the boundary conditions are applied, therefore, they produce the applied potential, V^{APP}. The total mean potential, therefore, is obtained as

$$V = V^{\mathrm{FREE}} + V^{\mathrm{APP}}. \tag{5.9}$$

In the case of NP+LEMC, the double layers are necessary to produce the $V^{\mathrm{FREE}}(z)$ component that counteracts the applied field, $V^{\mathrm{APP}}(z)$. Figure 5.8A shows that the slope of $V^{\mathrm{FREE}}(z)$ is the opposite to the slope of $V^{\mathrm{APP}}(z)$ in the bulks, so their sum (TOTAL) has the slope close to zero. This is necessary because the bulks are low-resistance elements, where the potential drop is small.

In the case of (n)PNP, this phenomenon depends on the imposed boundary conditions, Eq. 5.7, on the membrane surface. Using, for example, $g = 0$ yields totally different results which are in poor agreement with NP+LEMC as far as the structure of these double layers is concerned (the behaviour inside the pore is less influenced).

Comparing the counter-ion profiles in the double layers and in the neighbour-

ing half nanopore (Figs. 5.6 and 5.7), we can see that if there are less counter-ions in the double layer, there are less counter-ions in the half nanopore too (see anions on the left hand side in the OFF state compared to the ON state, for example). Although the decrease of counter-ion concentration in the pore is related to the decrease of the concentration of the same ion in the neighbouring double layer, it would be an overstatement to say that one is a consequence of the other.

Rectification works without this coupling between ion quantities in the double layer and in the nanopore. For example, rectification is reproduced in the case of PNP with boundary condition $g = 0$ although with worse agreement with NP+LEMC. Furthermore, the formation of the double layers is absent in MD simulations using explicit water, still, rectification is present. MD results using explicit water are in good agreement with NP+LEMC results using implicit water [67]. These contradictions require more study, but it seems that the formation of the double layers is rather related to boundary conditions and larger-scale effects, while the structure of the ionic profiles inside the pore is rather related to local effects such as interaction with pore charges, applied field, and other ions.

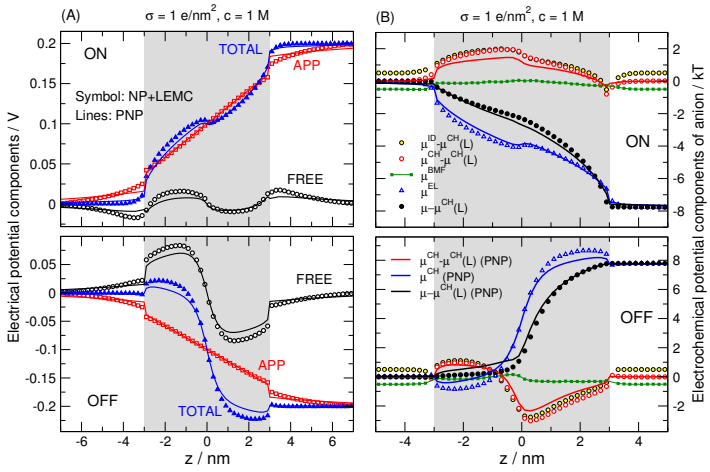

Figure 5.8: (A) Electrical potential profiles and components (see Eq. 5.9) as obtained from NP+LEMC and PNP. Component $V^{\mathrm{FREE}}(z)$ is the product of ions and pore charges in the system, while $V^{\mathrm{APP}}(z)$ is the applied potential computed from the Laplace equation with Dirichlet boundary conditions. (B) Electrochemical potential profiles and components (see Eqs. 5.2, 5.3-5.5) as obtained from NP+LEMC and PNP. The ideal ($\mu_i^{e,\mathrm{ID}}(z) = \mu_i^{e,0} + kT \ln c_i(z)$), the electrochemical ($\mu_{e,i}(z)$), and the chemical ($\mu_i^{\mathrm{CH}}(z)$) terms are shifted to zero by deducting $\mu_i^{\mathrm{CH}}(\mathrm{L})$, which is the value of the chemical term in the left bath. In the case of PNP the ID and CH terms are the same, so $\mu_i^{\mathrm{BMF}} = 0$. Results are shown for the anion; data for the cation do not reveal new insights (subscript i is dropped in the legend). Parameters are $c = 1$ M, $\sigma = 1\ e/\mathrm{nm}^2$, and $R = 1$ nm.

As far as the agreement between the NP+LEMC and the theoretical profiles

is concerned, it is generally better in the ON state than in the OFF state. In the OFF state, (n)PNP usually overestimates concentrations causing the overestimation of current as we have seen before. This is counterintuitive, because it was said that (n)PNP is better at low concentrations, but pore concentrations are higher in the ON state. We can resolve this contradiction if we consider that the system's behaviour is a result of the balance of basically three effects: (1) interaction with the fixed pore charges, (2) interaction with the fixed applied field, and (3) mutual and complicated interactions between ions. The mutual weight of these terms is different in the ON and OFF states.

In the ON state, pore charges and applied field act in the same direction, so they dominate the energy and errors in the ion-ion term have less effect. In the OFF state, however, pore charges and applied field act in the opposite directions, so their sum is smaller and the ion-ion term has a larger weight and the BMF term with it.

Our next goal is to better understand the different contribution to the total electrochemical potential μ_i as defined in Eqs. 5.2–5.5. The electrical component μ_i^{EL} is defined as the interaction with the (total) mean electrical potential that is shown in Fig. 5.8A. Note that the BMF term is fully included in the CH term and therefore, in the case of (n)PNP, μ_i^{CH} is just $\ln c_i$, while it also contains the BMF term in the case of NP+LEMC.

Figure 5.8B shows the full electrochemical potentials, the CH terms, and the EL terms. In the case of NP+LEMC, we also plot the $\ln c_i(z)$ term (denoted as ID) and the BMF term. The ID and CH terms, as well as the total electrochemical potential, are all shifted by the value of the CH term in the left bath ($\mu_i^{\mathrm{CH}}(\mathrm{L})$). In this way, the $\mu_i^e(z)$, $\mu_i^{\mathrm{CH}}(z)$, and $\mu_i^{\mathrm{EL}}(z)$ contributions take the value zero at the left edge of the plot.

The errors in μ_i have three components: the error in reproducing (1) the $\ln c_i$ term, (2) the EL term, and (3) the BMF term that can be identified with errors in reproducing the particle correlations which are missing in PNP, due to the mean field approximation. The first two errors have different signs and tend to balance each other. They are coupled through the Poisson equation, so in the limiting case of agreeing c_i profiles, the V profiles agree if the boundary conditions are also the same.

In this case, the NP equation would give the same flux if the BMF term were constant, because $\nabla\mu_i^e$ would be the same in the two methods. Therefore, the real source of errors is not the magnitude of the BMF term, but the **r**-dependence of the BMF term, that is, the fact that ionic correlations are different inside the pore than

outside. The nonzero value of the BMF term, on the other hand, indicates that there is an error in "chemistry", so there is a possibility for further errors in both the c_i and V profiles inside the pore. Those potential errors can eventuate inside the pore and become visible in all profiles. Local fluctuations in the BMF term inside the pore indicate how seriously do the errors of the mean-field treatment of PNP contribute to inaccuracies of all the profiles inside the pore.

5.3.6 Discussion of the example 1

One of the motivations of this section was to produce results for the model nanopore transistor using both a mean-field continuum theory (PNP) and a hybrid method including particle simulations (NP+LEMC) that can compute ion size effects and electrostatic correlations beyond the mean-field treatment. In the light of the results we can conclude that PNP is able to capture the qualitative behaviour of the device as shown by Figs. 5.2–5.8.

This indicates that the behaviour of ionic profiles (as the first-order determinant of current) mainly depends on the interaction of ions with pore charges and applied field, while interaction of ions beyond interaction with the mean electric field is secondary. Interaction with pore charges tunes the depth of depletion zones and directly modulates the electric current. The applied potential makes the profiles asymmetric along the axial dimension and produces the driving force of the steady-state current.

The approximate nature of the PNP theory appears in quantitative disagreement between PNP and NP+LEMC results. This can be seen both in the current data (Figs. 5.2A, 5.3, 5.4A, 5.5A, 5.6A, 5.7A, and 5.8) and in the concentration profiles (Figs. 5.2B, 5.5B, 5.6B, and 5.7B). Sources of this quantitative disagreement are the following. (1) The effective cross section through which the ionic centres are transported is $R_{\text{pore}}^2\pi$ in the case of PNP where the ions are point charges, while it is $(R_{\text{pore}} - R_i)^2\pi$ in the case of NP+LEMC, where ions are finite spheres with radii R_i. Because of this, PNP tends to overestimate concentration profiles at the peaks (Figs. 5.2B and 5.5B). (2) Lack of hard sphere exclusion in PNP also tends to cause overestimation compared to NP+LEMC. (3) Lack of electrostatic correlations in PNP, on the other hand, tends to decrease concentration profiles in the depletion zones compared to NP+LEMC, where ions that have peaks (counter-ions) tend to draw the ions of opposite charges (co-ions) into the depletion zones through pair-correlations.

Quantitative agreement, however, indicates that PNP is a proper tool to study the behaviour of this system and those even larger in dimensions as demon-

strated by several computational studies [38; 88; 1; 132; 86; 131; 112; 145; 151; 128]. Basically, PNP works well for these systems (also in the case of bipolar diodes), because the behaviour of these devices is primarily driven by the depletion zones caused by mean-field effects (interaction with pore charges and applied field).

Qualitative disagreement is expected in cases where ionic correlations cause asymmetric behaviour such as electrolytes containing multivalent ions (e.g., 2:1 and 3:1 electrolytes). Furthermore, PNP cannot compute cases where the size of ions and specific interactions with binding sites are important such as in the case of our nanopore sensor model [96], where the function of the sensor was based on the selective interaction of the analyte ions with square-well binding potentials and their competition with the main charge carrier cation (potassium) for space inside the nanopore. In general, particle simulations are better suited for modeling sensors based on specific interactions and geometries.

5.4 Example 2 - transistor

5.4.1 Simulation setup

The device studied here is composed of two baths separated by a membrane. The two sides of the membrane is connected by a single cylindrical pore that penetrates the membrane. The system has a rotational symmetry around the axis of the pore, therefore, the solution is done in terms of cylindrical coordinates z and r (the simulation cell in the LEMC simulation is three-dimensional, however). The solution domain is a cylinder of 30 nm width and 9 nm radius for a pore with $H_{\text{pore}} = 10$ nm length and $R_{\text{pore}} = 1$ nm radius. For longer and wider pores, these dimensions are proportionately larger. Fixed values of the concentrations and potential are prescribed on the half-cylinders on the left and right hand side.

The simulation setup for this example is similar to the previous one with one main difference - a symmetric charge pattern is created on the wall of the nanopore as shown in Fig. 5.9. There are regions of widths H_{n} on the two sides of the pore carrying σ_{n} surface charges, while there is a central region of width H_{x} and charge σ_{x}.

Here, the σ_{n} regions set the main charge carrier. In this study, we typically use negatively charged regions (hence the notation n), so the main charge carriers are the cations because the σ_{n} surface charges produce depletion zones of cations in these regions.

The task of the central region with the adjustable surface charge σ_{x} is to regulate the flow of cations (this is the independent variable of the device, hence

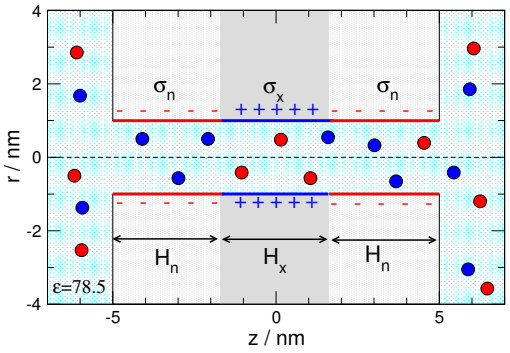

Figure 5.9: Schematics of the cylindrical nanopore that has three regions of lengths $H_{\rm n}$, $H_{\rm x}$, and $H_{\rm n}$. These regions carry $\sigma_{\rm n}$, $\sigma_{\rm x}$, and $\sigma_{\rm n}$ surface charges, respectively. The radius of the nanopore is $R_{\rm pore} = 1$ nm in this study. The simulation cell is larger than this domain of this figure, but also rotationally symmetric; the three-dimensional model is obtained by rotating the figure about the z-axis. The electrolyte inside the pore and on the two sides of the membrane is represented as charged hard sphere ions immersed in a dielectric continuum of dielectric constant $\epsilon = 78.5$. The dielectric constant is the same everywhere including the interior of the membrane. The PNP model closely mimics this model as described in the main text.

the notation x). If $\sigma_{\rm x}$ is positive, it produces a depletion zone for cations, so the pore contains depletion zones for both ionic species. The total current, therefore, is small. This corresponds to the closed state of the device. We distinguish special cases for combinations of $\sigma_{\rm n}$ and $\sigma_{\rm x}$ when these surface charges are -1, 0, or 1 e/nm^2. We denote these charges by symbols "$-$", "0", and "+", respectively. So if $\sigma_{\rm n} = -1$ e/nm^2 and $\sigma_{\rm x} = 1$ e/nm^2, the nanopore is characterised by the string "$-+-$" (as in Fig. 5.9).

In the three-dimensional LEMC model, the pore charges are placed on the pore wall as point charges on a grid. The size of a grid surface element is about 0.2×0.2 nm^2. The magnitude of point charges was calculated so that the surface charge density agrees with the preset values $\sigma_{\rm n}$ or $\sigma_{\rm x}$. This solution was chosen to mimic the continuous charge distribution used in the PNP calculations.

5.4.2 Results

This paper studies the quantitative effect of changing the charge pattern (the values of $\sigma_{\rm n}$, $\sigma_{\rm x}$, $H_{\rm n}$, and $H_{\rm x}$) on the nanopore's wall. We introduce special cases that we denote by strings "$-+-$", "$-\,0\,-$", "$---$" and so on as introduced earlier. Some of these patterns are defined as open states of the transistor ("$-\,0\,-$" and "$---$"),

while "$-+-$" is defined as the closed state. This way, we can define a switch whose device function is the ratio of currents in the open and closed states, $I_{\text{open}}/I_{\text{closed}}$. The larger this number is, the better the device works as a switch.

In this work, we use a 1:1 electrolyte with the same ionic diameters for the cation and the anion (0.3 nm). This choice makes a more straightforward comparison with PNP that cannot distinguish between ions of different sizes. The dielectric constant is $\epsilon = 78.5$, the temperature is $T = 298.15$ K. The bulk diffusion constant of both ion species is $1.334 \cdot 10^{-9}$ m^2/s, while the value inside the pore is ten times smaller [103; 96], a choice that has no consequence on qualitative conclusions.

In the case of 0.1 M concentration, this corresponds to about 800 ions in the LEMC simulations. An NP+LEMC calculation contained 80 iterations with LEMC simulations sampling 30 million configurations in an iteration. Running such a simulation lasted about 3 days. This resulted in small statistical uncertainties for the currents; the error bars ar smaller than the symbols with which the current data are plotted in the figures. The PNP calculations, on the other hand, took only a few minutes.

Effect of charge pattern: changing surface charges

As a first step, we vary the charge densities σ_{x} and σ_{n} and examine the resulting effect on the ionic current through the nanopore for a fixed geometry ($H_{\text{n}} = 3.4$ nm and $H_{\text{x}} = 3.2$ nm). This current is driven by voltage 200 mV; the concentration of the electrolyte is $c = 0.1$ M on both sides of the membrane. These parameters are valid for all figures unless otherwise stated.

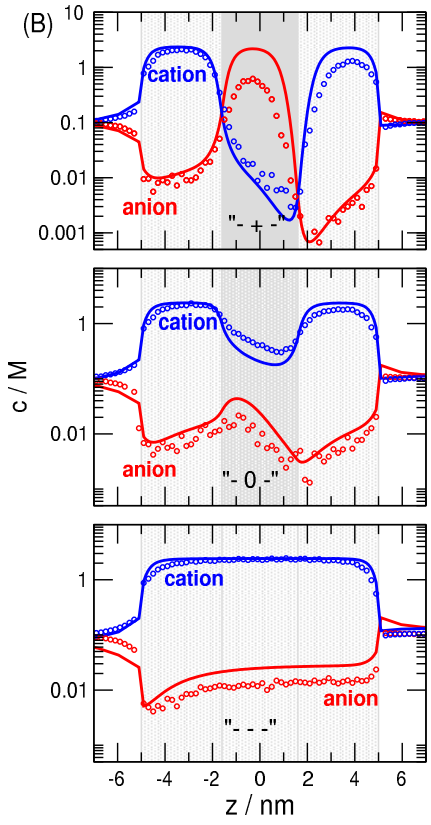

Figure 5.10: Current as a function of $-\sigma_x$ while $\sigma_n = -1\ e/\text{nm}^2$ is kept fixed. Selected charge patterns are indicated with "$---$", "$-\,0\,-$", and "$-+-$". Increasing σ_x makes the x region more negative, so the $I(-\sigma_x)$ function is monotonically increasing.Symbols and lines denote NP+LEMC and PNP results, respectively.

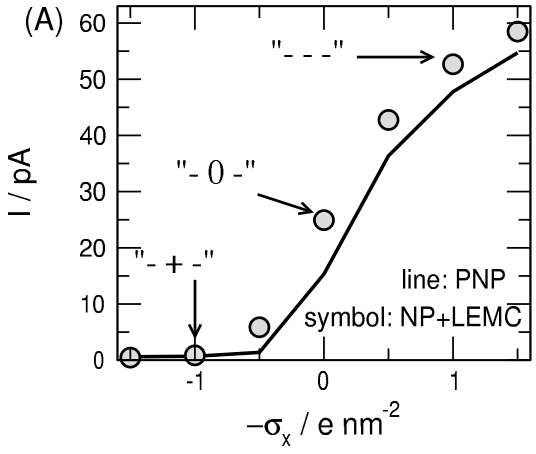

Figure 5.11: Concentration profiles for these selected charge patterns. Widths of the regions are $H_x = 3.2$ and $H_n = 3.4$ nm, electrolyte concentration is $c = 0.1$ M, voltage is 200 mV. Symbols and lines denote NP+LEMC and PNP results, respectively, here and in all the remaining figures unless otherwise stated.

Figure 5.10 shows results for a fixed $\sigma_n = -1$ e/nm^2 and varying σ_x. The negative value of σ_n makes the nanopore cation-selective due to the large surface charge and small pore radius. Therefore, the main charge carrier is the cation. The current of the anion remains below 0.5 pA. The anions have depletion zones in the two n regions as seen in Fig. 5.11. Whether the anions have depletion zones in the central x region depends on the value of σ_x, but this is irrelevant.

In this model, the value of σ_x tunes the depletion zones of the cations, and, thus, the cation current. In the case of $\sigma_x = 1$ e/nm^2 ("$-+-$"), cations have a depletion zone in the middle, so their current is cut. This is a closed state of the device (Fig. 5.11). Decreasing σ_x towards negative values, the depletion zone of cations gradually vanishes (see Fig. 5.11) and the cation current gradually increases (see Fig. 5.10).

Effect of charge pattern: changing region widths

Next, we fix the charge densities and change the geometry, namely, the widths H_x and H_n for a fixed pore radius. Particularly, we examined the effect of changing the relative widths of the x and n regions while keeping the total width $H_{pore} = 2H_n + H_x = 10$ nm fixed. In the open state ("$---$"), there is no difference between these regions, so we need to examine the closed state ("$-+-$") only. We plot the currents in the closed state as functions of H_x in Fig. 5.12.

The top panel showing the total current exhibits a minimum that is better

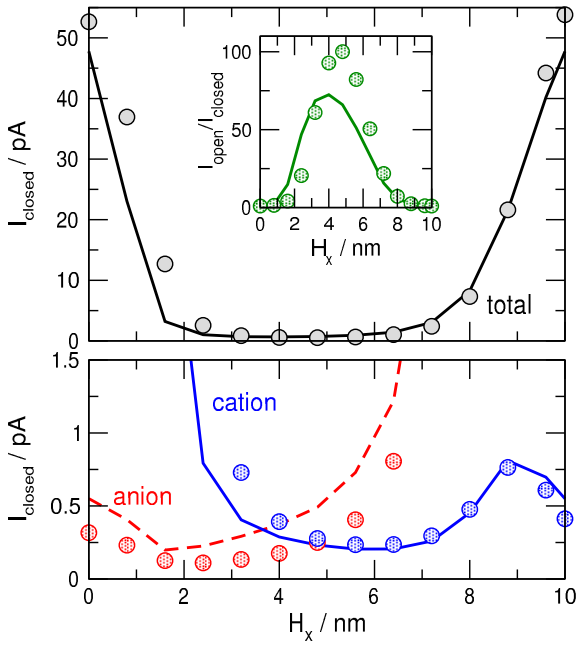

Figure 5.12: Currents in the closed state ("$-+-$") through nanopores with varying region lengths. The total length, $H_{\mathrm{pore}} = 2H_{\mathrm{n}} + H_{\mathrm{x}} = 10$ nm, is kept fixed. The results are shown as functions of H_{x}. Top panel shows the total current, while the bottom panel shows the cation and anion currents. The inset of the top panel shows the $I_{\mathrm{open}}/I_{\mathrm{closed}}$ ratio, where the charge pattern of the open state is "$---$" (its current is independent of H_{x}).

observed in the inset that shows $I_{\mathrm{open}}/I_{\mathrm{closed}}$. Because I_{open} does not depend on H_{x}, the ratio is proportional to the reciprocal of I_{closed}. The minimum in I_{closed}, therefore, corresponds to a maximum in the ratio characterising the quality of the device as a switch.

The explanation of this extremum can be depicted from the bottom panel of Fig. 5.12. For small H_{x} values, the pore is largely negatively charged, so the main charge carrier is the cation. For large H_{x} values, the situation is reversed: the main charge carrier is the anion. The minimum of the current occurs at a H_{x} value, where both regions have sufficient size to produce sufficiently deep depletion zones for both ionic species: for cations in the n regions, while for anions in the x region. This value is somewhere around $H_{\mathrm{x}} = 5$ nm.

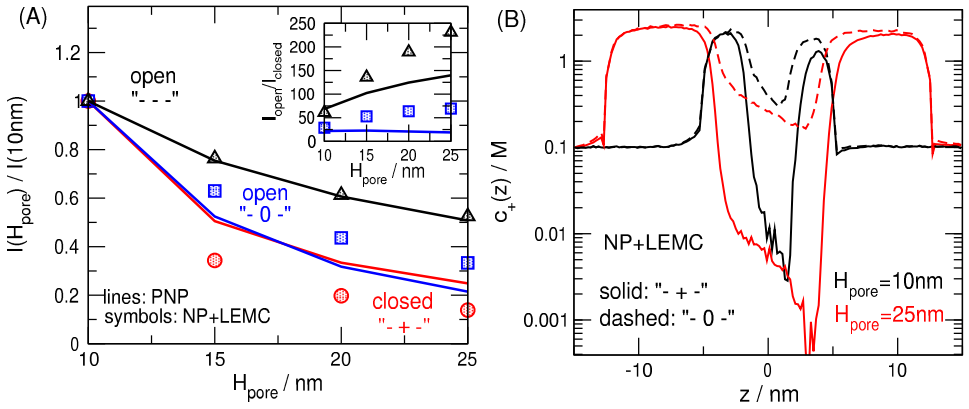

Figure 5.13: (A) Total currents as functions of pore length, H_{pore}, for various charge patterns with $H_{\text{n}}/H_{\text{x}} = 1.0625$ kept fixed. The currents are normalized with the values at $H_{\text{pore}} = 10$ nm. The inset shows the $I_{\text{open}}/I_{\text{closed}}$ ratio for the two cases where the open states are defined either with "$-\,0\,-$" or "$-\,-\,-$". (B) Concentration profiles of the anions (the charge carriers) for $H_{\text{pore}} = 10$ nm (black) and $H_{\text{pore}} = 25$ nm (red) for charge patterns "$-\,+\,-$" (solid) and "$-\,0\,-$" (dashed) as obtained from NP+LEMC simulations.

Effect of pore length

Figure 5.13 shows the result for the case, where the $H_{\text{n}}/H_{\text{x}}$ ratio is kept fixed at the value of 1.0625 and the total pore length, $H_{\text{pore}} = 2H_{\text{n}} + H_{\text{x}}$ is changed. Figure 5.13A shows the relative currents for the "$-\,-\,-$", "$-\,0\,-$" (open), and "$-\,+\,-$" (closed) states. We plot relative currents (normalised by the values at $H_{\text{pore}} = 10$ nm) because we are rather interested in how fast the currents decrease as functions of H_{pore} in the different cases (open and closed).

Figure 5.13A shows that the currents decrease faster in the closed state than in the open states. This results in an increasing $I_{\text{open}}/I_{\text{closed}}$ ratio as shown in the inset of Fig. 5.13A. The explanation is the deepening depletion zones with increasing H_{pore} (Fig. 5.13B).

The inset of Fig.5.13A also shows that the open/closed ratio exhibits a saturation behaviour so we can extrapolate to large H_{pore} values that are more common in experiments, but harder to attain with particle simulations such as LEMC. Summarised, increasing pore length promotes the formation of depletion zones due to weakening electrostatic correlations between neighbouring zones.

Effect of pore radius and concentration

We discuss the effect of nanopore radius and concentration together, because concentration determines λ_D , so R_{pore} and c influence the R_{pore}/λ_D ratio that distinguishes nanopores from micropores as discussed in the Introduction. In this work, we study the effect of changing R_{pore}/λ_D in three ways. First, we keep λ_D constant by fixing the concentration at $c = 0.1$ M and vary R_{pore}, then we do the reverse. Finally, we change both R_{pore} and c while keeping R_{pore}/λ_D fixed.

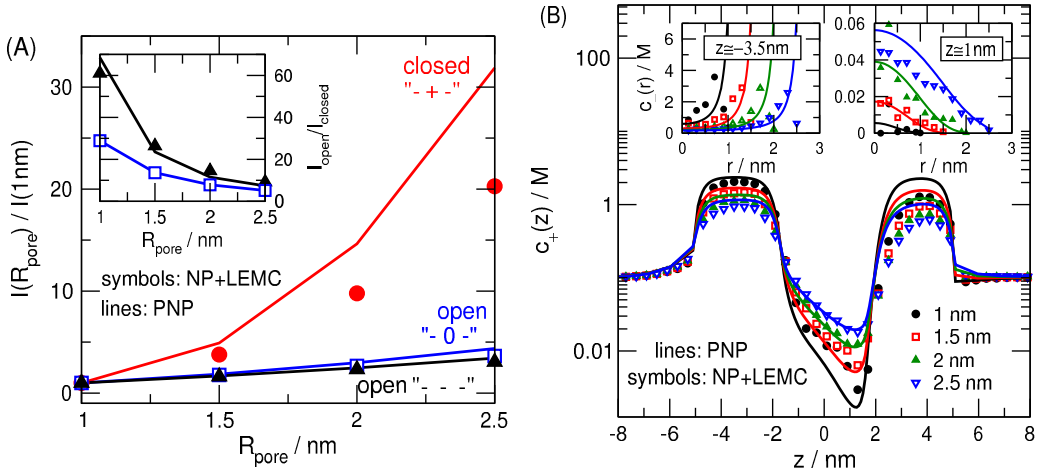

Figure 5.14: (A) Total currents as functions of pore radius, R_{pore}, for various charge patterns for $H_n/H_x = 1.0625$ and $H_{pore} = 10$ nm. The currents are normalized with the values at $R_{pore} = 1$ nm. The inset shows the I_{open}/I_{closed} ratio for the two cases where the open states are defined either with "$-\,0\,-$" or "$-\,-\,-$". (B) Axial concentration profiles of the cations (the charge carriers) for various R_{pore} values for charge pattern "$-+-$" (closed state). The insets show the radial concentration profiles for $z \approx -3.5$ nm (at a peak) and $z \approx 1$ nm (at the depletion zone).

Figure 5.14A shows the normalised currents as functions of R_{pore} for the closed ("$-+-$") and the two open ("$-\,0\,-$" and "$-\,-\,-$") cases. Here, we normalise with the currents at $R_{pore} = 1$ nm. The relative current in the closed state decreases faster with decreasing R_{pore} than in the closed state, which, in turn, results in increasing I_{open}/I_{closed} ratios with decreasing R_{pore} as shown by the inset.

Figure 5.14B shows the cross-section-averaged axial concentration profiles of the cations, $c_+(z)$, in the closed state for different pore radii. As R_{pore} decreases, the depletion zones in the middle get deeper, so the current decreases as Fig. 5.14A shows. The two insets show the radial concentration profiles, $c_+(r)$, at z-coordinates $z \approx -3.5$ nm (at a peak) and $z \approx 1$ nm (at the depletion zone). The profiles at $z \approx -3.5$ nm show that the cations are attracted to the pore wall and their

concentrations decline approaching the pore centreline ($r \sim 0$). The absence of a bulk electrolyte along the centreline is more apparent from the $c_+(r)$ profiles for $z \approx 1$ nm showing that concentrations never reach the bulk value (0.1 M).

Next, we study the effect of changing $R_{\text{pore}}/\lambda_{\text{D}}$ by keeping R_{pore} fixed at 1 nm and changing λ_{D} through varying concentration from $c = 0.05$ M to $c = 1$ M (it corresponds to changing the Debye length from $\lambda_{\text{D}} = 1.36$ nm to $\lambda_{\text{D}} = 0.304$ nm). Figure 5.15A shows the currents for the "$- - -$" (open) and "$-+-$" (closed) states. Both currents decrease with decreasing concentration, but the closed-state current decreases faster than the open-state current. This results in a increasing $I_{\text{open}}/I_{\text{closed}}$ ratio with decreasing c (see inset). The explanation again follows from the behaviour of depletion zones.

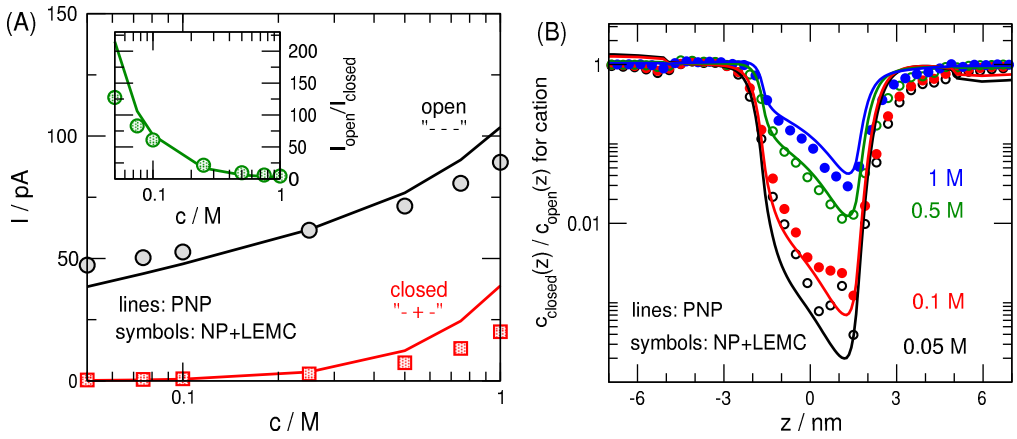

Figure 5.15: (A) Concentration dependence of the current in the open ("$- - -$") and closed ("$-+-$") states. The inset shows the $I_{\text{open}}/I_{\text{closed}}$ ratio. (B) Ratio of cation concentration profiles in the closed and open states for different bulk concentrations.

Figure 5.15B shows the cation concentration profiles in the closed state divided by the profiles in the open state. The behaviour of these curves for different bulk concentration reveals that the cations have deeper depletion zones compared to the open state for smaller bulk concentrations. Because the $c_{\text{open}}(z)/c_{\text{closed}}(z)$ ratio is a first-order determinant of the $I_{\text{open}}/I_{\text{closed}}$ ratio, this ratio increases with decreasing c due to deepening depletion zones in the closed state relative to the open state at same c.

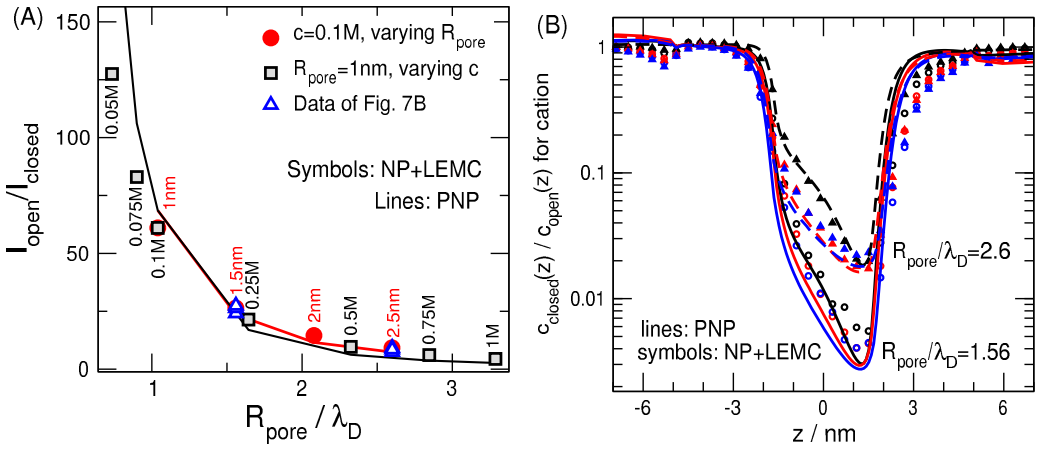

Figure 5.16: (A) The $I_{\text{open}}/I_{\text{closed}}$ ratio as a function of the $R_{\text{pore}}/\lambda_{\text{D}}$ variable for the cases, when we change R_{pore} at fixed λ_{D} ($c = 0.1$ M, red), and when we change λ_{D} by changing concentration for a fixed $R_{\text{pore}} = 1$ nm (black). The numbers near symbols indicate pore radii (red) or concentration (black). (B) Ratio of cation concentration profiles in the closed and open states for combinations of R_{pore} and λ_{D} for fixed $R_{\text{pore}}/\lambda_{\text{D}} = 1.56$ (solid lines and open symbols) and 2.6 (dashed lines and closed symbols) ratios. From bottom to top, the curves correspond to the following (R_{pore}/nm; c/M) pairs: (1.924; 0.0563) (blue), (1.5; 0.1) (red), (1; 0.225) (black) for $R_{\text{pore}}/\lambda_{\text{D}} = 1.56$ and (3.5; 0.0511) (blue), (2.5; 0.1) (red), (1; 0.626) (black) for $R_{\text{pore}}/\lambda_{\text{D}} = 2.6$. The $I_{\text{open}}/I_{\text{closed}}$ values for these points are indicated by blue triangles in Fig. 5.16A.

Finally, we performed simulations for two fixed values of $R_{\text{pore}}/\lambda_{\text{D}}$ (1.56 and 2.6) by using various combinations of R_{pore} and c (see caption of Fig. 5.16). These ways of studying $R_{\text{pore}}/\lambda_{\text{D}}$ dependence are summarised in Fig. 5.16A by plotting the $I_{\text{open}}/I_{\text{closed}}$ ratio against the $R_{\text{pore}}/\lambda_{\text{D}}$ ratio. The fact that the data are located along a single curve shows a scaling behaviour: we can either use a wide pore with small concentration (if fabrication of a narrow pore is the limiting factor), or a narrow pore with large concentration (if using small concentrations is the limiting factor due, for example, to detecting small currents).

Figure 5.16B shows the $c_{\text{closed}}(z)/c_{\text{open}}(z)$ cation profiles for those combinations of R_{pore} and λ_{D} (changed via changing c) that provide the 1.56 and 2.6 values for the ratio. The coincidence of the curves shows that scaling is valid not only for current ratios, but also for concentration ratios. Such scaling behaviour is always advantageous in designing devices for a given response function.

5.4.3 Discussion of the example 2

Manipulating charge pattern on the nanopore surface is a non-trivial chemical treatment for which, generally, the nanopore needs to be removed from the measuring cell. There is, however, a way of altering charge pattern during the measurement by changing the pH of the bath electrolytes in the measuring cell. If there are different chemical groups on the pore surface in the x and n regions that respond differently to pH (protonation vs. deprotonation), their charge can be changed with varying pH.

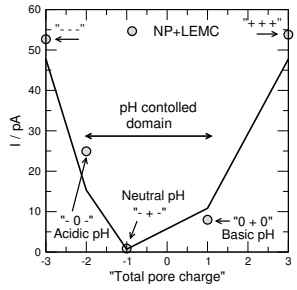

Figure 5.17: Demonstration of the effect of pH by plotting the current against the "total pore charge" characterising the asymmetry of the pore's charge distribution. Assuming that the `n` and `x` regions have about equal lengths, this dimensionless number is obtained by $\sum_{k=1}^{3} \sigma_k/\sigma_0$, where σ_k is the surface charge of region k and $\sigma_0 = 1\ e/\mathrm{nm}^2$. Closed states of the transistor are present in cases when this number is close to zero, namely, when depletion zones for both ionic species are present ("$-+-$"). For the example given in the main text (carboxyl and amino groups), this charge pattern is present at neutral pH. Open states are present when depletion zones for one of the ionic species are absent. The charge patterns "$0+0$" or "$-\,0\,-$" can be produced by tuning the pH towards basic or acidic, respectively. Parameters are those stated at Fig.5.10.

For example, if the surfaces of the n and x regions are functionalised by carboxyl and amino groups, respectively, they become negative and positive, respectively, at neutral pH ("$-+-$", closed state). Changing the pH to acidic, the carboxly groups in the n regions get protonated and become neutral. The amino groups of the x region, in the meantime, remain positive, so this results in a "$0+0$" (open) state. Changing the pH to basic, the amino groups in the x region get deprotonated and become neutral. The carboxyl groups of the n regions, in the meantime, remain negative, so this results in a "$-\,0\,-$" (also open) state. The results are shown in Fig. 5.8. Currents are shown as functions of a quantity depicted as "total pore charge". This is practically the sum of the magnitudes (with sign) of surface charges in the three regions. This figure is closely related to Fig. 5.3, where this "total pore

charge" was controlled with H_x. There, the minimum of the curve was at $H_x \approx 5$ nm, that corresponds to zero "total pore charge". In that case, there are both positive and negative regions in a balanced ratio so that depletion zones of both cations and anions form in an optimal way so that current is minimised. Here, the closed state ("$+-+$") appear at neutral pH, while the pore can be switched open with changing pH in any direction [88].

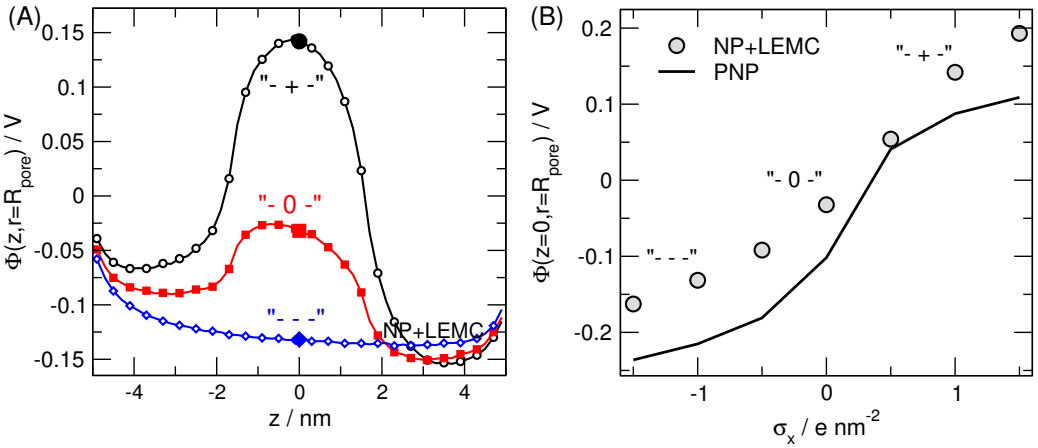

Figure 5.18: (A) The value of the mean electrical potential on the surface of the pore wall ($r = R_{\text{pore}}$) for three selected charge patterns as obtained from NP+LEMC calculations. (B) The value of this potential in the center of the pore ($z = 0$, $r = R_{\text{pore}}$ shown with larger symbols in panel A) as a function of σ_x. The figure demonstrates the monotonic relation between surface charge density, σ_x, and surface potential, $V(z = 0, r = R_{\text{pore}})$.

Controlling surface charge is quite different from controlling the electrical potential from a practical point of view, but from a modeling point of view, they are similar because charge is always related to electrical potential through Poisson's equation. To show this, we plot the electrical potential profile on the surface of the nanopore, $r = R_{\text{pore}}$, for different values of σ_x in Fig. 5.18A. The potential profile changes in zone x, because it is not an imposed quantity. The magnitude of the potential characterised by its value in the center, $z = 0$, depends unambiguously on σ_x. As Fig. 5.18B shows, there is a monotonic relation between charge, σ_x, and potential, $V(0, R_{\text{pore}})$. Therefore, to a first approximation, controlling the surface charge can mimic controlling the electrical potential, so the results of this study can be informative regarding the case of field effect nanofluidic transistors too.

Using an electrode to control the electrical potential near the nanopore leads to the presence of dielectric interfaces between materials of different polarisation properties (electrolyte vs. metal, for example). Polarisation charges are induced at

these dielectric boundaries that are different in every configuration of the ions, therefore, their presence influences the outcome of the calculations through influencing the probabilities of the individual configurations. Calculation of induced charges or the electrical potential produced by them is a time consuming process compared to the homogeneous dielectric model and pre-calculated applied potential used here, because the ion-ion interactions are not additive any more [16; 19; 20]. We refer studying this important case to future studies.

It is common to include electrodes (through imposing Dirichlet boundary conditions) and dielectric boundaries in mean field calculations (such as PNP). These calculations, however, include the effect of polarisation charges only on the *average* electrical potential. Electrostatic correlations resulting from the effect of induced charges on individual ionic configurations is ignored. If the electrodes are far from the nanopore, this approximation can be sufficient, however.

5.5 Summary

The general conclusion is that the BMF term is small and the agreement between PNP and NP+LEMC is very good. Yet, since the mean field theory does not capture the OFF state behaviour as good as the ON state, derived quantifies as the rectification cannot be predicted that well. Still the results are very promising given that these calculations have been performed for a narrow ($R = 1$ nm) and short (6 nm) pore with experimentally typical, but quite large surface charges ($\sigma \sim 1\ e/\text{nm}^2$). This indicates that the 2D PNP used in this study is an appropriate tool to study more realistic geometries (wider and longer pores), at least, as far as the agreement with simulations in the framework of an implicit solvent model is concerned.

This work is a link in a series of works, where a given system (a bipolar nanopore) is studied using different levels of modeling. Our results only prove that PNP calculations are useful in the framework of an implicit water model. Whether the implicit water model is a useful one is the topic of another publication [138], where we compare implicit-water NP+LEMC simulations with explicit-water MD simulations.

A real nanopore is obviously too big to use MD simulations and all-atom models as a general tool. Although computers are getting faster and faster, the quality of force fields seems to be a serious limiting factor. Still, all-atom (in this case, this means explicit water) MD simulations can be done for the nanopore of the size studied in this work. Therefore, MD simulations can have a serious role in a chain of calculations, where we increase the complexity of modeling step by step.

In general, simulation studies are more useful where local effects are important. The typical example is the narrow bottleneck of a nanopore, where double layers overlap. Nanopores can also be used as sensors [126; 78; 140; 117; 1; 80], where the detectable analyte molecule is selectively bound by a binding site of another molecule that is attached to the tip of the nanopore. The binding of the analyte molecule influences the effective cross section, and, thus, the current. An associated and thoroughly studied phenomenon is the crossing the a DNA molecule through the nanopore during which the sequencing might be possible in an efficient and fast manner [113; 110]. These are obviously local effects, where simulations are useful.

The device itself that is around the tip of the nanopore, however, is too big to compute with simulations using its real dimensions. In general, it is our purpose to model phenomena with their appropriate boundary conditions using close to real time and length scales at least on the meso-scopic level. This purpose can be achieved using the multiscale modeling framework in which the advantages of all the modeling levels and associated computation methods can be used.

This series of calculations proves that reducing the models by neglecting certain effects is an appropriate procedure for the case of ionic solutions and the bipolar nanopore studied here. This is also due to the fact that the transport of ions is mainly determined by electrostatic effects. The interactions with the applied field, permanent surface charges, and other ions treated on a mean field level are sufficient to reproduce the system's basic behaviour. For different systems, procedures similar to this should be repeated in order to evaluate the validity of the mean field approximation.

Chapter 6

Optimal control problems for nanoscale pores

In this chapter, we focus on optimal control problems for nanopores, in particular how one can optimise the surface charge to obtain a desired ionic flux. Similar problems were considered for the semiconductor devices in [69; 70]. Here the authors optimised the doping profiles to obtain a desired current. The doping profile of a semiconductor corresponds to the distribution of implanted impurities and has a strong influence on the IV curve. In nanopores the shape as well as the surface charge influence the current-voltage characteristics, see [31; 5; 29]. In the chapter, we consider a pore with fixed geometry and aim at optimising the surface charge distribution to obtain a desired current. As a next step, one could think of optimising the shape as well or considering different target functionals, such as maximising its rectification behaviour.

We consider radially symmetric pores, which allow us to use the 1D area averaged PNP model derived in Chapter 2. This reduces the computational complexity significantly, which is particularly important since we have to solve the forward problem as well as the corresponding adjoint system, in every iteration step of the optimal control solver. We discuss two different optimal control approaches for two ionic species of opposite charge - 1 and -1 for simplicity. Note that the proposed approaches can be generalised for multiple ionic species and different valencies, at the cost of readability.

The scaled 1D PNP system for two species is given by

$$-\gamma\partial_x\Big(A\partial_x V\Big) = A(p-n) + \kappa\partial A(x)\sigma, \tag{6.1a}$$

$$\partial_x\Big(D_n A[\partial_x n - n\beta\partial_x V]\Big) = \partial_x \mathcal{J}_n = 0, \tag{6.1b}$$

$$\partial_x\Big(D_p A[\partial_x p + p\beta\partial_x V]\Big) = \partial_x \mathcal{J}_p = 0, \tag{6.1c}$$

where $A(x) = r(x)^2\pi$ is the area function. We consider a pore of length L, which is connected to bath regions of length $2L$. Hence we consider (6.1) on the interval $(-2L, 3L)$, with a typical pore length of $L = 12000$nm. System (6.1) is considered with Dirichlet boundary conditions given by $V = 0|_{x=-2L}$, $V = V_{apl}|_{x=3L}$ and the bath concentrations given by $p(-2L) = p(3L) = n(-2L) = n(3L) = c_B$.

6.1 Minimisation problem

The existence and regularity results presented in Chapter 2 ensure the well-posedness of the forward problem, that is the 1D PNP model. To formulate the optimal control problem we define the state space

$$Y := y_D + [H_0^1(\Omega) \cap L^\infty(\Omega)]^3,$$

where $y_D = (V_D, c_B, c_B)$ denotes the boundary data.

The space $H_0^1(\Omega)$ corresponds to $H^1(\Omega)$ functions with zero trace at the boundary. This space is a Banach space with the norm

$$||y||_Y = ||y||_{(H^1(\Omega))^3} + ||y||_{(L^\infty(\Omega))^3}.$$

By Z we denote the co-state space given by $Z := [H^1(\Omega)]^3$ and Σ stands for the admissible control space given by

$$\Sigma := \{\sigma \in H^1(\Omega) \cap L^\infty(\Omega) : supp(\sigma) = [0, L]\}.$$

We define the state vector $y = (V, p, n)$ and write (6.1) in operator form

$$0 = e(y, \sigma) := \begin{pmatrix} -\gamma\partial_x\Big(A\partial_x V\Big) - A(p-n) - \kappa\partial A\sigma \\ \partial_x\Big(D_n A[\partial_x n - n\beta\partial_x V]\Big) \\ \partial_x\Big(D_p A[\partial_x p + p\beta\partial_x V]\Big) \end{pmatrix}.$$

The existence of a solution to (6.1) for a given $\sigma \in \Sigma$ has been shown in Theorem 2.

Next we show that the operator $e(y,\sigma)$ is Frechet differentiable.

Theorem 8. *The operator $e(y,\sigma)$ is twice Frechet differentiable with a first derivative at (x,σ) in the direction $\bar{y} = (\bar{V},\bar{n},\bar{p}) \in [H_0^1(\Omega) \cap L_0^\infty(\Omega)]^3$,*

$$\begin{aligned} < e_y(y,\sigma)\bar{y}, h > =& < -\gamma\partial_x\Big(A\partial_x\bar{V}\Big), h_V > \\ & - < D_n\partial_x[An\beta\partial_x\bar{V}], h_1 > + < D_p\partial_x[Ap\beta\partial_x\bar{V}], h_2 > \\ & + < A\bar{n}, h_V > - < \partial_x\Big(D_nA[\partial_x\bar{n} - \bar{n}\beta\partial_xV]\Big), h_1 >, \\ & + < -A\bar{p}, h_V > + < \partial_x\Big(D_pA[\partial_x\bar{p} + \bar{p}\beta\partial_xV]\Big), h_2 > \end{aligned}$$

for all $h = (h_V, h_1, h_2) \in Z$ and

$$< e_\sigma(x,\sigma)\bar{\sigma}, h >= -\kappa\partial A < \bar{\sigma}, h_V >,$$

for $\bar{\sigma} \in \Sigma$ and $h \in Z$.

Proof. The proof follows the lines of Theorem 2.3 in [69]. □

Next we formulate the constrained optimisation problem. We want to minimise (maximise) a cost functional $\mathcal{Q}(y,\sigma)$ under the constraint that (6.1) is satisfied. The cost functional $\mathcal{Q}$ corresponds misfit between the actual and the desired current, but could be chosen differently as well (to obtain a desired rectification behaviour for example). We consider

$$\mathcal{Q}(y,\sigma) \to \max_{\sigma} \text{ s.t. } 0 = e(y,\sigma). \tag{6.2}$$

To prove that this optimisation problem has a solution we need to make the following assumptions on $\mathcal{Q}(y,\sigma)$:

(A5) Let $\mathcal{Q}(y,\sigma) : X \times \Sigma \to \mathbb{R}$ be twice Frechet differentiable with Lipschitz continuous second derivative.

(A6) Let $\mathcal{Q}(y,\sigma)$ be separable, that is $\mathcal{Q}(y,\sigma) = \mathcal{Q}_1(y) + \mathcal{Q}_2(\sigma)$, bounded from below and weakly lower semi-continuous.

Theorem 9. *Let A1-A4 from Chapter 2 be satisfied and let $\mathcal{Q}(y,\sigma)$ satisfy A5-A6 then the constrained optimisation problem* (6.2) *admits a solution $(V^*, n^*, p^*, \sigma^*) \in Y \times \Sigma$.*

Proof. The proof is based on Stampaccias method and can be found in [69]. □

We recall that we can not expect unique minimisers, since the forward problem does not have a unique solution. We will illustrate the non-uniqueness of the surface charge distribution with different numerical experiments at the end of this chapter.

6.1.1 First order optimality conditions

Optimal current

In the following we want to determine the optimal surface charge σ to obtain a desired current. In this case the cost functional is given by

$$\mathcal{Q}_y(y,\sigma) = \frac{1}{2}\left|\int_\Gamma \mathcal{J}\, d\nu - \mathcal{J}^*\right|^2 dx, \tag{6.3}$$

where $\mathcal{J}^*$ denotes the desired current. Note that this functional satisfies (A5) as a Lipschitz operator in y. Note that the current J is constant along the pore and we evaluate it only on the boundary $\{-2L, 3L\}$.

First order optimality conditions

The first order optimality conditions can be computed from the corresponding Lagrange functional. The Lagrangian $\mathcal{L}(y,\sigma,\lambda) : Y \times \Sigma \times Z \to \mathbb{R}$ is given by

$$\mathcal{L}(y,\sigma,\lambda) = Q(y,\sigma) + < e(y,\sigma), \lambda >,$$

where $\lambda = (\lambda_V, \lambda_1, \lambda_2)$. Theorem 8 and assumption (A5) ensure that the Lagrangian $\mathcal{L}$ is continuously Frechet differentiable. The first order optimality condition is

$$\nabla_{y,\sigma,\lambda}\mathcal{L}(y,\sigma,\lambda) = 0.$$

Note that we obtain the state equation $e(y,\sigma) = 0$ from condition $\nabla_\lambda \mathcal{L}(y,\sigma,\lambda) = 0$. The variation with respect to σ gives

$$-Q_\sigma(y,\sigma) = e^*_\sigma(y,\sigma)\lambda \text{ in } \Sigma^*, \tag{6.4}$$

where $e^*(y,\sigma) \in L(Z,\Sigma^*)$ denotes the adjoint operator of $e(y,\sigma)$. The last variation leads to

$$-Q_y(y,\sigma) = e^*_y(y,\sigma)\lambda \text{ in } Y^*. \tag{6.5}$$

The next step is to derive the adjoint system to the 1D PNP equations and show its solvability for $\lambda = (\lambda_V, \lambda_1, \lambda_2)$. To calculate the optimality condition (6.5) we need to derive the adjoint equation to the $< e_y(y,\sigma)\bar{y}, \lambda >$. After calculating the Frechet

derivative and integration by part we obtain the following adjoint system

$$-\gamma\partial_x\Big(A\partial_x\lambda_V\Big) - \beta D_n\partial_x\Big(nA\partial_x\lambda_2\Big) + \beta D_p\partial_x\Big(pA\partial_x\lambda_1\Big) = 0 \tag{6.6a}$$

$$-A\lambda_V + \partial_x\Big(AD_n\partial_x\lambda_1\Big) - \beta AD_n\partial_x V\partial_x\lambda_1 = 0, \tag{6.6b}$$

$$A\lambda_V + \partial_x\Big(AD_p\partial_x\lambda_2\Big) + \beta AD_p\partial_x V\partial_x\lambda_2 = 0,, \tag{6.6c}$$

with boundary conditions

$$\begin{aligned}
&\lambda_V(-2L) = \lambda_V(3L) = 0,\\
&\lambda_1(-2L) = 0 \quad \lambda_1(3L) = \frac{\partial\mathcal{Q}(x,\sigma)}{\partial n}(3L),\\
&\lambda_2(-2L) = 0 \quad \lambda_2(3L) = \frac{\partial\mathcal{Q}(x,\sigma)}{\partial p}(3L).
\end{aligned}$$

The existence and uniqueness of the solutions in space Z is discussed in [69] [Theorem 4.2].

6.2 Optimisation in Slotboom variables

The so-called Scharfetter Gummel scheme, which solves the PNP system in Slotboom variables iteratively, is a robust and popular computational method in engineering. Since we use this discretisation to solve the forward problem (6.1), we need to calculate the respective adjoint equations in these variables. We recall that the Slotboom variables are given by

$$u_1 = \exp(-\beta V)n \quad \text{and} \quad u_2 = \exp(\beta V)p,$$

and the current reads as

$$\mathcal{J}_1 = A\exp(\beta V)\nabla u_1 \quad \text{and} \quad \mathcal{J}_2 = -A\exp(-\beta V)\nabla u_2.$$

For simplicity we set here and latter on the diffusion coefficients D_n and D_p to 1. Hence system (6.1) in Slotboom variables is

$$-\gamma\nabla\cdot(A\nabla V) = A(-e^{\beta V}u_1 + e^{-\beta V}u_2) + \kappa\partial A\sigma, \tag{6.7a}$$

$$\nabla\cdot(Ae^{\beta V}\nabla u_1) = 0, \tag{6.7b}$$

$$\nabla\cdot(Ae^{-\beta V}\nabla u_2) = 0. \tag{6.7c}$$

System (6.7) is solved in Netgen using a hybrid discontinuous Galerkin method on

a 1D the non-uniform mesh, see [93; 34; 104]. The discretisation allows for a stable and accurate discretisation of the system even in the case of non-smooth parameters.

Donnan equilibrium We will consider another simplification of the problem by omitting the bath regions in the following. This has the advantage that we do not have to restrict the control variable to the pore region, where we want to modify the surface charge. To do so, we assume that the system is in thermal equilibrium at the pore entrances. This corresponds to a so-called Donnan-equilibrium boundary conditions, see for example [31]. We set

$$V_D = V - V_{apl}, n_D = c_B \exp(-\beta V_D) \text{ and } p_D = c_B \exp(\beta V_D),$$

and use the charge neutrality condition on the pore entrees (0 and L), that reads

$$A\gamma(p-n) + \kappa \partial A \sigma = 0$$

to obtain

$$\begin{aligned} n_D(x) &= \frac{\kappa \partial A(x)\sigma(x) + \sqrt{(\kappa \partial A(x)\sigma(x))^2 + 4(A(x)c_B)^2}}{2A(x)} \\ p_D(x) &= \frac{-\kappa \partial A(x)\sigma(x) + \sqrt{(\kappa \partial A(x)\sigma(x))^2 + 4(A(x)c_B)^2}}{2A(x)}, \end{aligned}$$

and

$$V_D(x) = -\frac{\ln(\frac{n_D(x)}{c_B})}{\beta} \text{ for } x \in \{0, L\}.$$

In the following we impose Donnan boundary conditions and omit the bath regions in the optimisation, therefore $\Omega = (0, L)$.

Lagrange multiplier with Donnan boundary condition Optimal control as well as inverse problems are usually ill-posed. Therefore the solution either does not exist, is not unique or does not depend continuously on the data, see [120; 118]. Due to the ill-possedness of the problem we introduce an additional regularisation term in the cost functional $\mathcal{Q}$. To ensure that the minimum of the regularised problems is close to the initial guess we choose $\frac{\epsilon}{2}\int_0^L (\sigma - \sigma^*)^2$ where σ^* is the initial surface charge distribution. Next we consider the Lagrange functional of the optimal control

problem in adjoint variables to calculate the respective equations. It is given by

$$\begin{aligned}\mathcal{L}_\epsilon(V,u_1,u_2,\sigma,\lambda_V,\lambda_1,\lambda_2) = Q + \frac{\epsilon}{2}\int_0^L (\sigma-\sigma^*)^2 \\ + \int_0^L \big(-\gamma\nabla\cdot(A\nabla V) - A\kappa(-e^{\beta V}u_1 + e^{-\beta V}u_2) - 2\kappa\partial A\sigma\big)\lambda_V \\ - \int_0^L Ae^{\beta V}\nabla u_1\nabla\lambda_1 - \int_0^L Ae^{-\beta V}\nabla u_2\nabla\lambda_2\end{aligned}$$

The first variations of the functional reads

$$\frac{\partial\mathcal{L}_\epsilon}{\partial V}\bar{V} = \frac{\partial Q}{\partial V}\bar{V} + \int_0^L \beta\bar{V}A[-e^{\beta V}\nabla u_1\nabla\lambda_1 + e^{-\beta V}\nabla u_2\nabla\lambda_2] \tag{6.8a}$$

$$+ \int_0^L \big(-\gamma\nabla\cdot(A\nabla\lambda_V) + A\beta\kappa(e^{\beta V}u_1 + e^{-\beta V}u_2)\lambda_V)\bar{V}, \tag{6.8b}$$

$$\frac{\partial\mathcal{L}_\epsilon}{\partial u_1}\bar{u}_1 = \frac{\partial Q}{\partial u_1}\bar{u}_1 - \int_0^L Ae^{\beta V}\nabla\bar{u}_1\nabla\lambda_1 + \int_0^L \bar{u}_1 A\kappa e^{\beta V}\lambda_V, \tag{6.8c}$$

$$\frac{\partial\mathcal{L}_\epsilon}{\partial u_2}\bar{u}_2 = \frac{\partial Q}{\partial u_2}\bar{u}_2 - \int_0^L Ae^{-\beta V}\nabla\bar{u}_2\nabla\lambda_2 - \int_0^L \bar{u}_2 A\kappa e^{-\beta V}\lambda_V, \tag{6.8d}$$

$$\frac{\partial\mathcal{L}_\epsilon}{\partial\sigma}\bar{\sigma} = \epsilon\int_0^L \bar{\sigma}(\sigma-\sigma^*) + \int_0^L \kappa\partial A\bar{\sigma}\lambda_V. \tag{6.8e}$$

The first order optimality condition gives the adjoint system of equations for λ_i, that is

$$-\gamma\nabla\cdot(A(x)\nabla\lambda_V) + \lambda_V A(x)\kappa\beta(e^{\beta V}u_1 + e^{-\beta V}u_2) \tag{6.9a}$$

$$-A(x)\beta e^{\beta V}\nabla u_1\nabla\lambda_1 + A(x)\beta e^{-\beta V}\nabla u_2\nabla\lambda_2 = 0, \tag{6.9b}$$

$$\nabla\cdot(A(x)e^{\beta V}\nabla\lambda_1) + A(x)\kappa e^{\beta V} = 0, \tag{6.9c}$$

$$\nabla\cdot(A(x)e^{-\beta V}\nabla\lambda_2) - A(x)\kappa e^{-\beta V} = 0, \tag{6.9d}$$

with boundary condition given by

$$\begin{aligned}\lambda_V(0) = 0 \quad \text{and} \quad \lambda_V(L) = 0, \\ \lambda_1(0) = 0 \quad \text{and} \quad \lambda_1(L) = \mathcal{J} - \mathcal{J}^*, \\ \lambda_2(0) = 0 \quad \text{and} \quad \lambda_2(L) = \mathcal{J} - \mathcal{J}^*.\end{aligned}$$

6.2.1 Results

In this section we present numerical results based on the formulation in Slotboom variables. Having an initial σ^0 the solver is based on the following iteration:

Set $\bar{\sigma}(x) = \sigma^0$ an initial guess;
Calculate $V^0, u_1^0, u_2^0, \mathcal{J}^0$ solving the PNP equation;
while $err > 10^{-2}$ **and** $max\_iter > k$ **do**
  Solve the adjoint system (6.9c) - (6.9b) to obtain λ_V;
  Update $\sigma^{k+1} = \sigma^k + \frac{\partial \mathcal{L}_\epsilon}{\partial \sigma}\bar{\sigma}$ using equation (6.8e) ;
  Calculate $V^{k+1}, u_1^{k+1}, u_2^{k+1}, \mathcal{J}^{k+1}$, solving the PNP equation;
  Calculate value of the functional Q^{k+1} (6.3) ;
  Calculate the stoping criterion err $= \frac{|Q^k - Q^{k+1}|}{Q^k}$
end

Algorithm 2: Adjoint optimisation method.

The algorithm is implemented using the software package Netgen-Ngsolve. We consider a pore of length 12000nm with a radius changing from 10 to 20nm. The applied potential is set to 200mV and the bath concentration for both ionic species are 0.1M.

In the first test case we set the goal current to be 1.5 times the value of the initial current. The initial value of the surface charge is given by $\sigma = \sin(\frac{2\pi x}{12000})$. To obtain the solution we use a mesh consisting of 4000 elements. 20% of these elements are uniformly distributes in the first 50nm of the pore and the other 80% is also uniformly distributed on the remaining part. This mesh refinement was necessary to obtain stable and accurate numerical results.

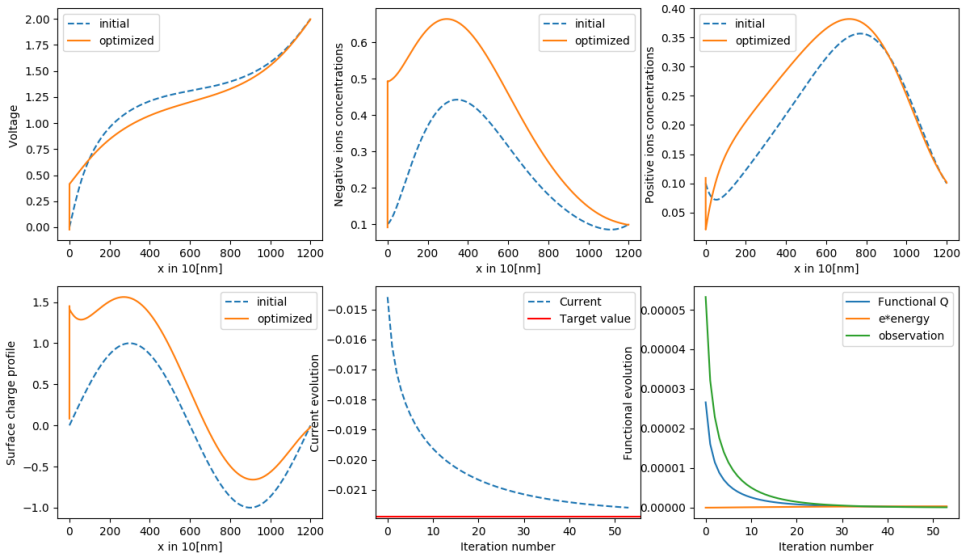

Figure 6.1: Evolution of the V (left upper plot), concentrations (n and p), surface charge profile, current with the target value and the evolution of the functional Q .

Figure 6.1 shows the initial and obtained profiles. We observe that the functional Q as well as the data misfit term $|\mathcal{J} - \mathcal{J}^*|$ decreases during the iterations. At the same time the regularisation term $\frac{\epsilon}{2}\int_0^L(\sigma - \sigma^*)$, denoted by the expression e*energy in the figures, increases. The main disadvantage of this method is the fact that the obtained surface charge profile is not smooth around $x = 0$. This problem is clearly visible close to the pore entrance. For that reason the method is not suitable for very small pores or for pores with complex geometry at the entrance.

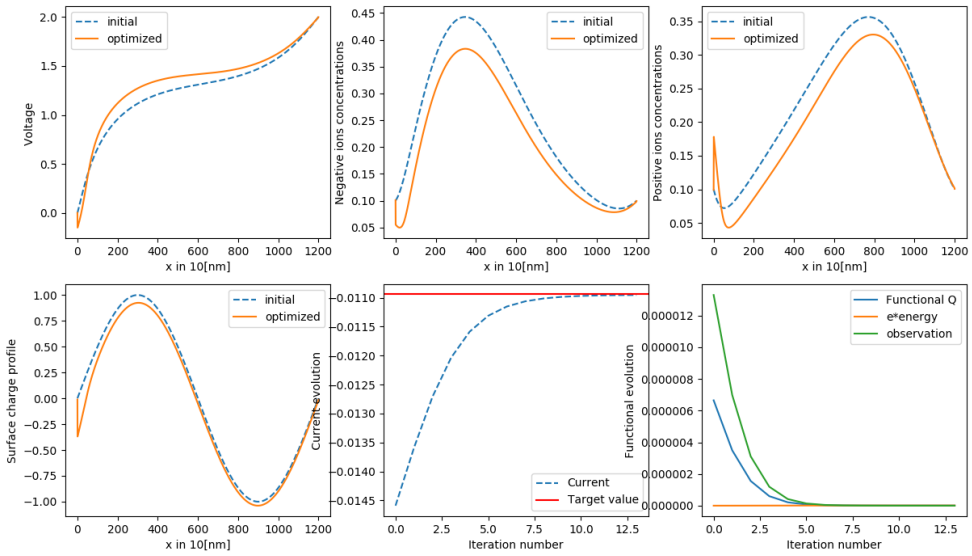

Figure 6.2: Evolution of the V (left upper plot), concentrations (n and p), surface charge profile, current with the target value and the evolution of the functional Q .

Figure 6.2 shows the result for the same problem, but a different target value. Here the desired current is 0.75 times the initial value. We observe significant changes in the surface charge close to the pore entrance. This suggests that the narrow part of the pore has the strongest influence on the obtained current.

6.3 Fast optimisation method

We will compare the previously discussed approach, see subsection 6.2, with a fast optimisation technique presented by Burger and Pinnau in [25]. The proposed method is based on different control, which results in a decoupled system that can be solved very efficiently. In this section, we adapt this method for the 1D area averaged a PNP system derived in 2.1. This method introduces a much stronger regularisation, which leads to smoother profiles. This also implies lower computational costs, since one can use a coarser discretisation. We recall that the adjoint method introduced in 6.2 required a finer resolution at the narrow pore interface, due to the strong variation of the surface charge.

We introduce the control function W given by

$$W = \Delta(V - V^*), \tag{6.10}$$

where V^* is the initial potential profile inside the pore. Then W satisfies

$$\begin{aligned}-\gamma A(x)W - \gamma \nabla A(x)\nabla(V - V^*) = \\ A(x)[u_2 e^{-\beta V} - u_2^* e^{-\beta V^*}) - (u_1 e^{\beta V} - u_1^* e^{\beta V^*})] + \kappa \partial A(x) 2(\sigma - \sigma^*),\end{aligned}$$

where p^* and n^* denote the initial concentrations. The surface charge is then given by

$$\begin{aligned}\partial A(x) 2\pi\sigma = &- \gamma A(x)W - \gamma \nabla A(x)\nabla(V - V^*) \\ -A(x)[u_2 e^{-\beta V} - u_2^* e^{-\beta V^*}) - (u_1 e^{\beta V} - u_1^* e^{\beta V^*})] &+ \kappa \partial A(x)\sigma^*.\end{aligned}$$

From the above relations we conclude

$$W(0) = -\frac{\nabla A(0)\nabla(V - V^*)(0)}{A(0)} \text{ and } W(L) = -\frac{\nabla A(L)\nabla(V - V^*)(L)}{A(L)}.$$

The new control variable gives a new regularisation term, in particular $\frac{\epsilon}{2}\int_0^L W^2$. Let Q_ϵ denote the new objective functional given by

$$Q_\epsilon = Q + \frac{\epsilon}{2}\int_\Omega W^2 dx. \tag{6.11}$$

Then the minimisation problem in terms of the new control function reads as

$$\min Q_\epsilon \text{ such that } (u_1, u_2, V, W) \in \mathcal{D}_{adm}, \tag{6.12}$$

where the admissible domain is given by

$$\begin{aligned}\mathcal{D}_{adm} := \{(u_1, u_2, V, W) \in (H^1(\Omega))^2 \times H^1(\Omega) \cap L^\infty(\Omega) \times L^2(\Omega) \\ \text{and } (u_1, u_2, V) \text{ satisfy the PNP system (6.7) and } W \text{ satisfies (6.10)}\}.\end{aligned}$$

6.3.1 Existence of the minimisers

To ensure that (6.12) has a solution we need the following two properties: lower semi-continuity of the functional $\mathcal{Q}$ and the weak closedness of the domain. The first poperty is satisfied in $H^1(\Omega) \cap L^\infty(\Omega)$. The second part requires that W is in $\mathcal{D}_{adm}$ i.e. $\Delta(V - V^*) \in L^2(\Omega)$.

Theorem 10. *Let $\epsilon > 0$ and $A \in H^1(\Omega)$ then there exist a minimiser $(\bar{u}_1, \bar{u}_2, \bar{V}, \bar{W}) \in (H^1(\Omega))^2 \times H^1(\Omega) \cap L^\infty(\Omega) \times L^2(\Omega)$ of (6.12).*

Proof. Let take $(u_1^k, u_2^k, V^k, W^k)_{k\in\mathbb{N}}$ the minimising sequence then $W^k \in L^2(\Omega)$ and we obtain that $(V^k - V^*) \in H^2(\Omega) \hookrightarrow \bar{C}(\bar{\Omega})$. We set the initial guess $V^* \in L^\infty(\Omega)$ to provide that $V^k \in L^\infty(\Omega)$. The $u_{1,2}^k$ satisfy the elliptic equations (6.14c) – (6.14d) so (See Gilbarg Trudinger [Theorem 8.3]) ensures that $u_{1,2}^k \in H^1(\Omega) \cap L^\infty(\Omega)$.

Thus we extract a weakly convergent subsequent $(u_1^{k^l}, u_2^{k^l}, V^{k^l}, W^{k^l})$ in $(H^1(\Omega))^2 \times H^1(\Omega) \times L^2(\Omega)$. From the weak closedness of the admissible domain and weak lower semi-continuity we conclude the existence of the minimisers. □

Since

$$\kappa\partial A\sigma = \kappa\partial A\sigma^* - \gamma AW - \nabla A\nabla(V - V^*) - A[u_2 e^{-\beta V} - u_2^* e^{-\beta V^*}) - (u_1 e^{\beta V} - u_1^* e^{\beta V^*})],$$

and together with the regularity of W, initial guess σ^* and the area function we conclude that the charge profile $\sigma \in L^2(\Omega)$ and satisfies the PNP equations (6.1).

Corollary 6.3.1.1. *There exists a doping profile $\sigma \in L^2(\Omega)$ that minimise the the functional $\mathcal{Q}$ such that $(u_1, u_2, V, W) \in \mathcal{D}_{adm}$.*

6.3.2 Fast optimisation method

Next we derive the optimality conditions, which gives us a decoupled system that can be solved very efficiently. The Lagrangian of (6.12) is given by

$$\begin{aligned}\mathcal{L}_\epsilon(V, u_1, u_2, W, \lambda_V, \lambda_1, \lambda_2) = Q + \frac{\epsilon}{2}\int_0^L W^2 + \int_0^L A\exp(\beta V)\nabla u_1 \nabla\lambda_1 \\ - \int_0^L A\exp(-\beta V)\nabla u_2\nabla\lambda_2 + \int_0^L \nabla(V - V^*)\nabla\lambda_V + W\lambda_V.\end{aligned}$$

Note that the Lagrangian $\mathcal{L}_\epsilon$ is continuously Frechet differentiable on $\mathcal{D}_{adm} \times H^1(\Omega)^3$. Differentiation with respect to the primal variables (V, u_1, u_2, W) gives

$$\frac{\partial \mathcal{L}_\epsilon}{\partial V}\bar{V} = \frac{\partial Q}{\partial V}\bar{V} + \int_0^L \beta \bar{V} A[\exp(\beta V)\nabla u_1 \nabla \lambda_1 + \exp(-\beta V)\nabla u_2 \nabla \lambda_2] + \nabla \bar{V} \nabla \lambda_V, \tag{6.13a}$$

$$\frac{\partial \mathcal{L}_\epsilon}{\partial u_1}\bar{u}_1 = \frac{\partial Q}{\partial u_1}\bar{u}_1 + \int_0^L A \exp(\beta V)\nabla \bar{u}_1 \nabla \lambda_1, \tag{6.13b}$$

$$\frac{\partial \mathcal{L}_\epsilon}{\partial u_2}\bar{u}_2 = \frac{\partial Q}{\partial u_2}\bar{u}_2 - \int_0^L A \exp(-\beta V)\nabla \bar{u}_2 \nabla \lambda_2, \tag{6.13c}$$

$$\frac{\partial \mathcal{L}_\epsilon}{\partial W}\bar{W} = \int_0^L \bar{W}(\epsilon W + \lambda_V). \tag{6.13d}$$

Note that the adjoint system (6.13b) – (6.13a) has a triangular structure and can be analysed and solved separately. That provides existence and uniqueness of the solutions of the adjoint equations. Setting the equation (6.13d) to 0 the multiplier λ_V can be replaced by setting $\epsilon W = -\lambda_V$. Then the system (6.13b) – (6.13a) can be written as

$$\frac{\partial \mathcal{L}_\epsilon}{\partial V}\bar{V} = \frac{\partial Q}{\partial V}\bar{V} + \int_0^L \bar{V}\beta A[\exp(\beta V)\nabla u_1 \nabla \lambda_1 + \exp(-\beta V)\nabla u_2 \nabla \lambda_2] + \bar{V}\Delta \epsilon W.$$

Which leads to

$$-\epsilon \Delta W = A\beta[\exp(\beta V)\nabla u_1 \nabla \lambda_1 + \exp(-\beta V)\nabla u_2 \nabla \lambda_2].$$

That leads to the system of equations for solving the optimization problem given by the system of equations

$$\Delta V = \Delta V^* + W, \tag{6.14a}$$

$$\nabla \cdot (Ae^{\beta V}\nabla u_1) = 0, \tag{6.14b}$$

$$\nabla \cdot (Ae^{-\beta V}\nabla u_2) = 0, \tag{6.14c}$$

$$\nabla \cdot (Ae^{\beta V}\nabla \lambda_1) = 0, \tag{6.14d}$$

$$\nabla \cdot (Ae^{-\beta V}\nabla \lambda_2) = 0, \tag{6.14e}$$

$$-\epsilon \Delta W = A\beta[\exp(\beta V)\nabla u_1 \nabla \lambda_1 + \exp(-\beta V)\nabla u_2 \nabla \lambda_2]. \tag{6.14f}$$

together with the boundary condition for respective equations

$$
\begin{aligned}
u_1(0) &= n_D, & u_1(L) &= n_D \exp(-\beta V_{appl}),\\
u_2(0) &= p_D, & u_2(L) &= p_D \exp(\beta V_{appl}),\\
\lambda_1(0) &= 0, & \lambda_1(L) &= \mathcal{J}^* - \mathcal{J},\\
\lambda_2(0) &= 0, & \lambda_2(L) &= \mathcal{J}^* - \mathcal{J},\\
W(0) &= -\frac{\nabla A(0)\nabla(V-V^*)(0)}{A(0)}, & W(L) &= -\frac{\nabla A(L)\nabla(V-V^*)(L)}{A(L)}.
\end{aligned}
$$

The numerical procedure together with dumping algorithm is summarised in algorithm 3.

Set $\bar{\sigma}(x) = \sigma^0$ an initial guess;
Calculate $V^0, u_1^0, u_2^0, \mathcal{J}^0$ solving the PNP equation;
while $err > 10^{-2}$ **and** $max\_iter > k$ **do**
  Solve $\nabla \cdot (Ae^{\beta V^k}\nabla\lambda_1^{k+1}) = 0$;
  Solve $\nabla \cdot (Ae^{-\beta V^k}\nabla\lambda_2^{k+1}) = 0$;
  Solve $-\epsilon\Delta W^{k+1} + \tau W^{k+1} =$
  $\tau W^k + \beta A[\exp(\beta V^k)\nabla u_1^k \nabla\lambda_1^{k+1} + \exp(-\beta V^k)\nabla u_2^k\nabla\lambda_2^{k+1}]$;
  Solve $\Delta V^{k+1} = \Delta V^* + W^k$;
  Solve $\nabla \cdot (Ae^{\beta V^{k+1}}\nabla u_1^{k+1})$;
  Solve $\nabla \cdot (Ae^{-\beta V^{k+1}}\nabla u_2^{k+1}) = 0$;
  Calculate current $\mathcal{J}$ and the value of the functional $\mathcal{Q}$;
  Calculate the stoping criterion err $= \frac{|Q^k - Q^{k+1}|}{Q^k}$
end

Algorithm 3: Fast optimisation method.

6.3.3 Results

Next, we present some optimised surface charge profiles for a pore of length 12000mm, with a radius function varying from 1 to 100nm. First, we illustrate the influence of several parameters, namely τ, ϵ and the initial guess. We compare the results to the ones obtained in the previous section. The radius is linear varying from 10 to 20nm, the initial surface charge is set to $\sigma = \sin(\frac{2\pi x}{1200})$. We use the following set of parameters (if not stated otherwise): mesh size = 1000, $\tau = 0.1$. The stopping criterion was set as described in the algorithm 3. Figures 6.3 and 6.4 shows the initial and obtained profiles of the voltage and concentrations as well as the current value and functional Q evolution for two different values of the target current. The two plots show the obtained profiles for the target current set to be $1.5\mathcal{J}^{start}$ (figure

6.3) and $0.75\mathcal{J}^{start}$ (figure 6.4).

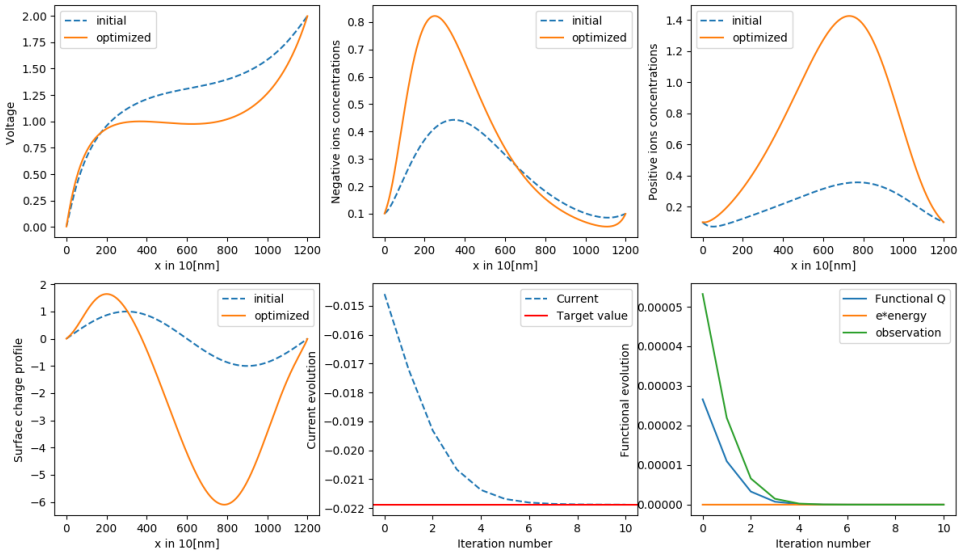

Figure 6.3: Evolution of the V (left upper plot), concentrations (n and p), surface charge profile, current with the target value and the evolution of the functional Q. The target current was set to $\mathcal{J}^* = 1.5\mathcal{J}^{start}$, the stabilisation parameters τ and ϵ set to 0.1 and 10^{-2} respectively.

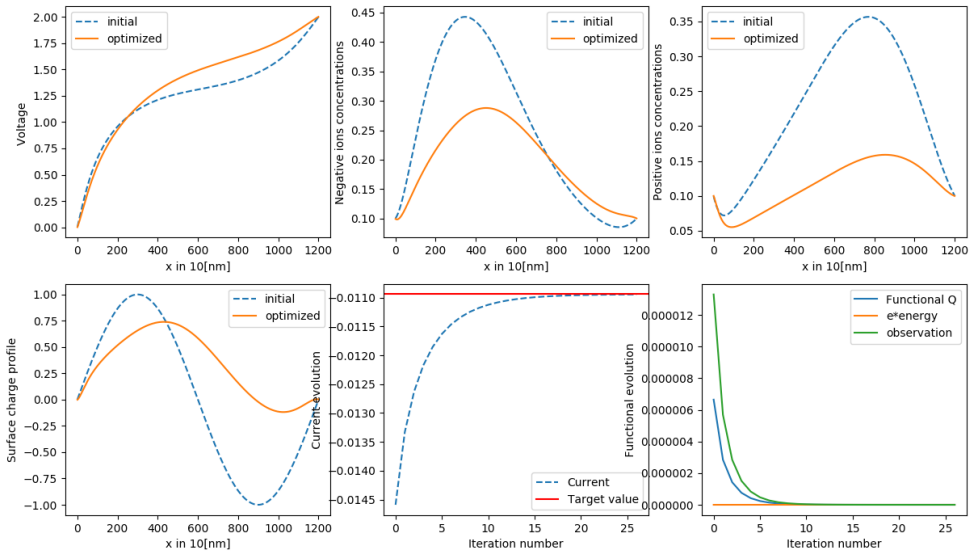

Figure 6.4: Evolution of the V (left upper plot), concentrations (n and p), surface charge profile, current with the target value and the evolution of the functional Q . The target current was set to $\mathcal{J}^* = 0.75\mathcal{J}^{start}$, the stabilisation parameters τ and ϵ set to 0.1 and 10^{-2} respectively.

What is more, due to the strong stabilisation effect of the method it can be applied for the pores with more demanding geometry in which the previous method does not converge. Figure 6.5 presents results obtained using a pore with linear radius varying from 1 to 100nm.

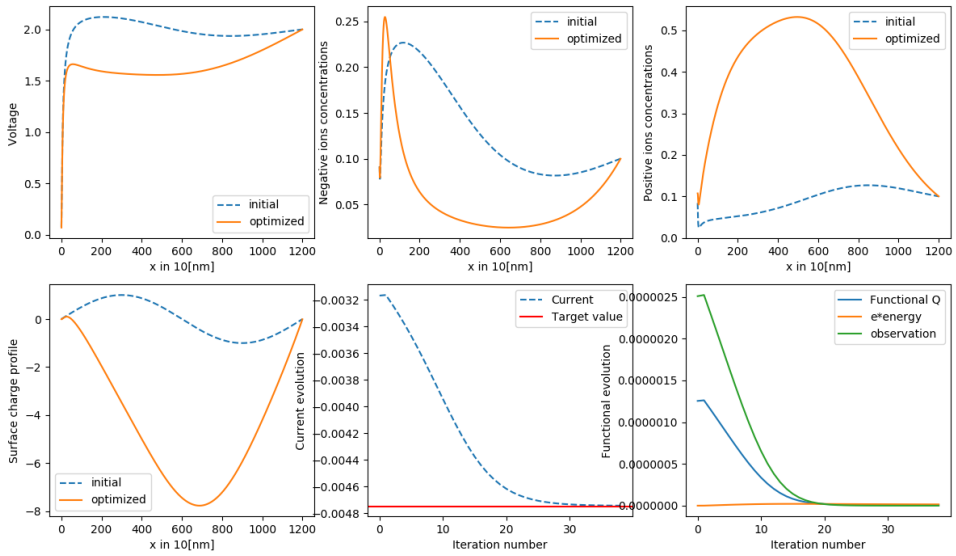

Figure 6.5: Evolution of the V (left upper plot), concentrations (n and p), surface charge profile, current with the target value and the evolution of the functional Q. The target current was set to $\mathcal{J}^* = 1.5\mathcal{J}^{start}$, the stabilisation parameters τ and ϵ set to 10^{-2} and 10^{-3} respectively.

We observe that the obtained surface charge profiles are much smoother than in the first approach.

6.4 Differences of the obtained profiles

We conclude by discussing differences in the obtained surface charge profiles. Figures 6.1 and 6.3 shows the results obtained by using two methods for the same test case. As we can observe the obtained profile differ highly.

What is more, choosing different initial guess lead to different solutions as well. By initialising the iterative schema with different σ^0 and setting the same target current, we obtain significant differences in the obtained profiles using the adjoint approach, see Figure 6.6 where we chose the following starting profiles:

$$\sigma_1 = 2\sin(\frac{2\pi x}{12000}) \text{ and } \sigma_2 = 6(\frac{x}{12000})(\frac{x}{12000} - 1).$$

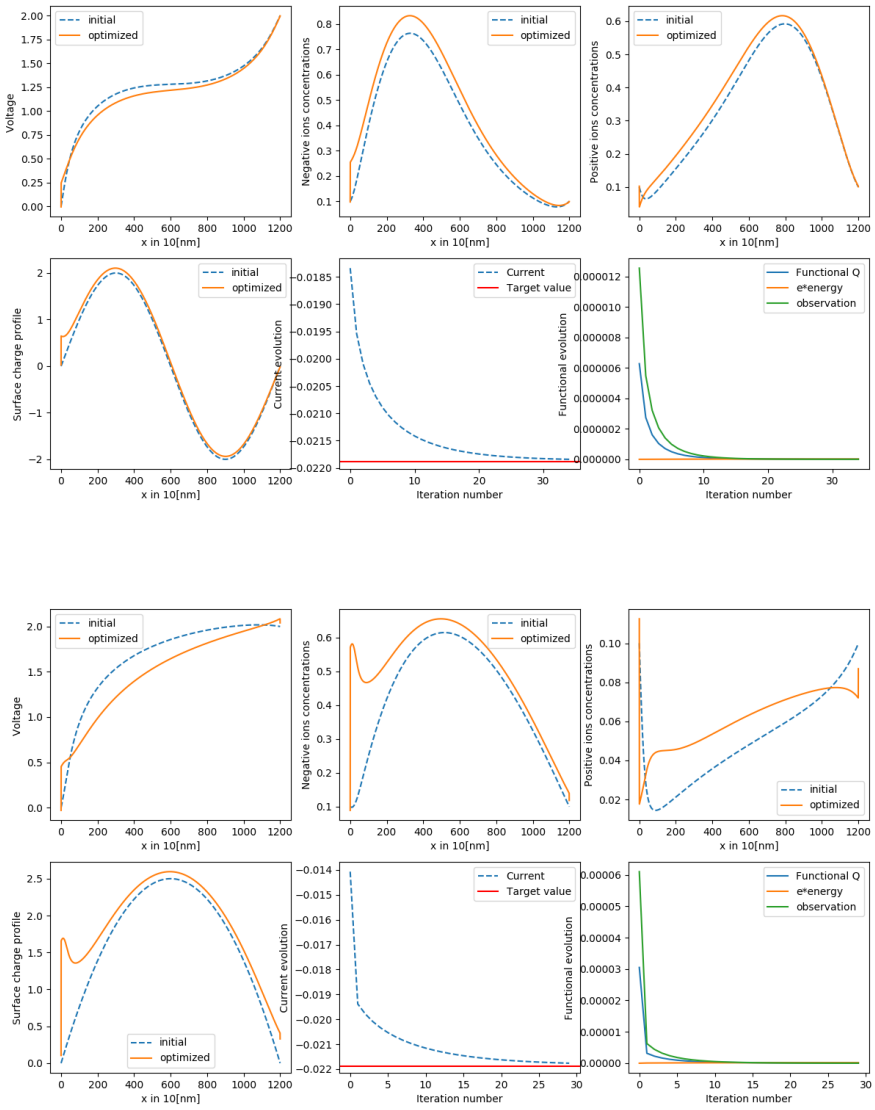

Figure 6.6: Comparison of the obtained profile using different initial guess.

We see that we obtain different profiles for all cases considered so far, even though the target current was the same. This shows that we can not expect uniqueness of the minimisers using only one measurement. We need to underline here that because of the construction of the methods we do not optimise exactly the same functionals in all of the cases. As it was mentioned before our stabilisation term $(\int(\sigma - \sigma^*))$ depends on the initial guess σ^* and though influence the obtained profiles.

6.5 Conclusions

In this chapter, we presented a theoretical and computational framework to optimise the current-voltage profile of nanopores. The optimisation is based on the surface charge profile. We investigate the effect of changes using two different optimal control approaches in the case of radially symmetric nanopores. Both approaches are based on the 1D area averaged PNP equations together with Donnan boundary conditions to reduce the computational complexity.

The first method is based on the adjoint equations and the steepest descent scheme. The optimised surface charge profile show strong variations in the narrow pore region. The solver requires a fine spatial discretisation and is computationally costly. On the other hand, the obtained profiles do not differ significantly from the initial guesses.

The second method - the so-called fast optimization method replaces the nonlinear part of the PNP equation by introducing a new control function. This modification leads to a decoupling of the forward and adjoint equations, which can be solved quickly and efficiently. The new control introduces a much stronger regularisation than the first method - hence the surface charge profiles are much smoother. However, it results in a much high carrier concentration at the pore wall and does not 'use' the geometry as much.

We conclude by stating possible future research directions:

- Since nanopores of a particular shape can be produced, an extension of the proposed framework which is based on optimising the surface charge and the pore geometry would be a natural next step. The dependence between shape and obtained current is more complex as the area function is involved in all the equations in the PNP system and would require the development of suitable splitting techniques.

- One of the most important characteristics of a nanopore is rectification. The optimization problem can be developed to maximise or minimise the rectification for a given pore geometry. Since the rectification is defined by the current ratio for two different applied voltages, the computational complexity of this problem is much larger.

- One current measurement leads to a non-unique solution to the optimisation problem. To address that issue the number of observation can be increased. Finding the surface charge profile that provides a given IV characteristic can

be another problem solved using similar tools.

Chapter 7

Conclusions and future work

7.1 Conclusions

This thesis focused on several challenges relate to modelling and computational aspects of the ion transport in confined geometries such as synthetic or biological pores. We compare and develop different approaches used in the literature. The respective chapters focused on specific aspects, such as modeling, analysis, asymptotic behaviour and optimal control problems related to ion transport.

A general introduction to the mathematical modeling of ion transport was given in Chapter 1. We discussed the most important driving forces of charged transport in confined geometries and how they can be included on the microscopic as well as macroscopic level. In Chapter 2 we derive a 1D area averaged Poisson-Nernst-Planck model, which can be used for radially symmetric pores. We use a fixed point argument to prove the existence of solutions and discuss the regularity depending on pore geometry. Moreover, we comment on existence for a nonlinear version of the PNP equations which accounts for finite size effects via additional nonlinearities in the mobility and entropy.

Chapter 3 develops an asymptotic analysis of the PNP equations which can be used for radially symmetric nanopores to resolve the behaviour around the charged surface walls correctly. The proposed methodologies were based on a suitable rescaling, which is valid in the case of large-aspect-ratio pores. It led to a decoupling of the radial and lateral direction, which allowed us to compute high-quality approximations very efficiently.

The methodologies developed in Chapter 3 can not be applied to respective nonlinear PNP systems, which includes finite volume effects. In Chapter 4 we use a different averaging strategy and compare the approximate solutions for several

mean-field models for ion transport in confined geometries. Detailed numerical investigations illustrate the impact of finite volume and solvation effects as well as solvent dynamics.

Chapter 5 compares different modeling approaches to describe ion transport in nanoscale pores (such as ion channels). Detailed numerical experiments illustrate the behaviour of solutions of the classic PNP equations and the so-called local equilibrium Monte Carlo method and give implications abound their validity in different regimes. In addition, we adapted the methodologies to analyse the behaviour of nanoscale devices.

In the last Chapter 6, optimal control problems related to nanopores were discussed. These problems are related to optimal control problems considered in the context of semiconductors - here one wants to optimise the doping profile to obtain specific current-voltage characteristics. We generalise optimal control approaches to optimise the surface charge of synthetic nanopores using the reduced PNP models developed in the previous chapters. Furthermore, we investigate the non-uniqueness of solutions and the effect of the pore geometry.

7.2 Future work

A common assumption of most models for ion transport considered in this thesis is the fact that fluid flow across the membrane can be omitted. We have seen in Chapter 4 that the flow has an impact on the transport properties, especially in the narrow tip region. Hence the development of models that include this phenomenon would enhance the understanding of the entire physical setup.

The proposed asymptotic analysis in Chapter 3 and 4 led to the development of the very fast solvers for ion transport through long and thin nanopores. A similar strategy could be used to approximate the passage of large particles in pores. Understanding these dynamics is important since similar situations occur in DNA sequencing. Understanding how long DNA chains and the respective electrostatic forces influence the measured current is still an open problem.

Multiscale models, which resolve the dynamics on the different scales correctly are a next step to develop more accurate and efficient numerical solvers. Coupling micro-, meso and macroscopic models by identifying the right scales, will be of great importance in future research.

Developing stable and efficient optimal control solvers to obtain desired characteristics - such as IV curves or rectification behaviour, by modifying the surface charge or geometry, is another promising research direction. The modification of

nanoscale pores and the development of nanoscale devices has experienced a tremendous boost in the last decades providing mathematical methodologies to support experimental design is of great importance for future technology development. Here several aspects, such as the development of fast optimization techniques, but also the right choice of models needs to be investigated more thoroughly.

This thesis includes the first steps of the research perspectives detailed above, by contributing to various aspect in model development, analysis, and numerical simulations.

Appendix A

Table of notation

Notation	Definition	Units
c_i	Concentration of the ionic species i	None
D_i	Diffusion coefficient	ms^{-2}
$\mathcal{E}$	Electric field	Vm^{-1}
e	Elementary charge	C
ϵ_r	Relative permittivity	None
ϵ_0	Vacuum permittivity	Fm^{-1}
F_i	Force field associated with specie i	N
F	Faraday constant	$Cmol^{-1}$
k_B	Boltzmann constant	JK^{-1}
λ_D	Debye length.	m
$\mathcal{J}_i$	Flux of the ionic species i	None
m	Number of ionic species	None
$\mathfrak{m}(\vec{n})$	Mobility function	None
m_i	Mass of the ionic species i	g
μ_i^e	Electrochemical potential of the ionic species i	V
μ_i^{chem}	Chemical potential of the ionic species i	V
μ_i^0	Reference potential of the ionic species i	V
n_i	Number of ions of of the ionic species per unit of volume	m^{-3}
n_a	Avogadro number	M^{-1}
n_S	Number of ions of of solvent per unit of volume	m^{-3}
n^F	Free charge density $n^F = e_0 \sum_{i=1}^m z_i n_i$	C
n	Total number of ionic and solvent particles	m^{-3}
ρ	Total concentration of the ionic species $\rho = \sum_{i=1}^m c_i$	None
σ	Surface charge density	Cm^{-2}
T	Temperature	K
$\vec{u}$	Solvent velocity	ms^{-1}
V	Electric potential	V
v_i	Volume of the ionic species i	m^3
z_i	Valence of the ionic species i	None

Table A.1: Physical constants and parameters.

Bibliography

[1] Y. Ai, J. Liu, B. Zhang, and S. Qian. Ionic current rectification in a conical nanofluidic field effect transistor. *Sensors and Actuators B: Chemical*, 157(2):742–751, 2011.

[2] S. Alizadeh and A. Mani. Multiscale model for electrokinetic transport in networks of pores, part i: Model derivation. *Langmuir*, 33(25):6205–6219, 2017.

[3] S. Alizadeh and A. Mani. Multiscale model for electrokinetic transport in networks of pores, part ii: Computational algorithms and applications. *Langmuir*, 33(25):6220–6231, 2017.

[4] D. Andelman. Electrostatic properties of membranes: the Poisson-Boltzmann theory. *Handbook of biological physics*, 1:603–642, 1995.

[5] P. Y. Apel, I. V. Blonskaya, O. L. Orelovitch, P. Ramirez, and B. A. Sartowska. Effect of nanopore geometry on ion current rectification. *Nanotechnology*, 22(17):175302, 2011.

[6] C. Bean and W. De Sorbo. Porous bodies and method of making, November 6 1973. US Patent 3,770,532.

[7] O. Beckstein and M. SP. Sansom. The influence of geometry, surface character, and flexibility on the permeation of ions and water through biological pores. *Physical biology*, 1(1):42, 2004.

[8] R. S. Berry, S. A. Rice, and J. Ross. *Physical Chemistry*. Oxford University Press, New York, 2nd edition, 2000.

[9] J.J. Bikerman. XXXIX. structure and capacity of electrical double layer. *The London, Edinburgh, and Dublin Philosophical Magazine and Journal of Science*, 33(220):384–397, 1942.

[10] Bioelectrolab. Ion channel, 2004.

[11] J. O'M. Bockris and A. K. N. Reddy. *Modern Electrochemistry.* Plenum Press, New York, 2 edition, 1988.

[12] D. Boda. Monte carlo simulation of electrolyte solutions in biology: in and out of equilibrium. *Annual Review of Compuational Chemistry*, 10:127–164, 2014.

[13] D. Boda. Monte Carlo simulation of electrolyte solutions in biology: In and out of equilibrium. volume 10 of *Ann. Rep. Comp. Chem.*, chapter 5, pages 127–163. Elsevier, 2014.

[14] D. Boda and D. Gillespie. Steady-state electrodiffusion from the nernst–planck equation coupled to local equilibrium monte carlo simulations. *Journal of Chemical Theory and Computation*, 8(3):824–829, 2012.

[15] D. Boda and D. Gillespie. Steady state electrodiffusion from the Nernst-Planck equation coupled to Local Equilibrium Monte Carlo simulations. *J. Chem. Theor. Comput.*, 8(3):824–829, 2012.

[16] D. Boda, D. Gillespie, W. Nonner, D. Henderson, and B. Eisenberg. Computing induced charges in inhomogeneous dielectric media: Application in a Monte Carlo simulation of complex ionic systems. *Phys. Rev. E*, 69(4):046702, 2004.

[17] D. Boda, J. Giri, D. Henderson, B. Eisenberg, and D. Gillespie. Analyzing the components of the free energy landscape in a calcium selective ion channel by Widom's particle insertion method. *J. Chem. Phys.*, 134(5):055102, 2011.

[18] D. Boda, R. Kovács, D. Gillespie, and T. Kristóf. Selective transport through a model calcium channel studied by Local Equilibrium Monte Carlo simulations coupled to the Nernst-Planck equation. *J. Mol. Liq.*, 189:100–112, 2014.

[19] D. Boda, M. Valiskó, B. Eisenberg, W. Nonner, D. Henderson, and D. Gillespie. The effect of protein dielectric coefficient on the ionic selectivity of a calcium channel. *J. Chem. Phys.*, 125(3):034901, 2006.

[20] D. Boda, M. Valiskó, B. Eisenberg, W. Nonner, D. Henderson, and D. Gillespie. Combined effect of pore radius and protein dielectric coefficient on the selectivity of a calcium channel. *Phys. Rev. Lett.*, 98(16):168102, 2007.

[21] R. Boda, D.and Kovács, D. Gillespie, and T. Kristóf. Selective transport through a model calcium channel studied by Local Equilibrium Monte Carlo simulations coupled to the Nernst–Planck equation. *Journal of Molecular Liquids*, 189:100–112, 2014.

[22] B. R. Brooks, C. L. Brooks, et al. Charmm: The biomolecular simulation program. *Journal of Computational Chemistry*, 30(10):1545–1614, 2009.

[23] M. Burger, R. S. Eisenberg, and H. W. Engl. Inverse problems related to ion channel selectivity. *SIAM Journal on Applied Mathematics*, 67(4):960–989, 2007.

[24] M. Burger, M. Di Francesco, J.-F. Pietschmann, and B. Schlake. Nonlinear cross-diffusion with size exclusion. *SIAM J. Math. Anal.*, 42(6):2842–2871, 2010.

[25] M. Burger and R. Pinnau. Fast optimal design of semiconductor devices. *SIAM Journal on Applied Mathematics*, 64(1):108–126, 2003.

[26] M. Burger, B.A. Schlake, and M.-T. Wolfram. Nonlinear Poisson–Nernst–Planck equations for ion flux through confined geometries. *Nonlinearity*, 25(4):961, 2012.

[27] D.Gillespie D Boda B. S. Eisenberg E. Sangiorgi C. Berti, S. Furini and C. Fiegna. Three-dimensional brownian dynamics simulator for the study of ion permeation through membrane pores. *Journal of chemical theory and computation*, 10(8):2911–2926, 2014.

[28] W. A. Catterall. From ionic currents to molecular mechanisms: the structure and function of voltage-gated sodium channels. *Neuron*, 26(1):13–25, 2000.

[29] J. Cervera, P. Ramírez, S. Mafe, and P. Stroeve. Asymmetric nanopore rectification for ion pumping, electrical power generation, and information processing applications. *Electrochim. Acta*, 56(12):4504–4511, 2011.

[30] J. Cervera, B. Schiedt, R. Neumann, S. Mafe, and P. Ramirez. Ionic conduction, rectification, and selectivity in single conical nanopores. *J. Chem. Phys.*, 124(10):104706, 2006.

[31] J. Cervera, B. Schiedt, and P. Ramirez. A poisson/nernst-planck model for ionic transport through synthetic conical nanopores. *EPL (Europhysics Letters)*, 71(1):35, 2005.

[32] J. Cervera, B. Schiedt, and P. Ramírez. A Poisson/Planck-Planck model for ionic transport through synthetic conical nanopores. *Europhys. Lett.*, 71(1):35–41, jul 2005.

[33] J. Chapman, J. Norbury, C. Please, and G. Richardson. Ions in solutions and protein channels. *Fifth Mathematics in Medicine Study Group, University of Oxford*, 2005.

[34] B. Cockburn, J. Gopalakrishnan, and R. Lazarov. Unified hybridization of discontinuous galerkin, mixed, and continuous galerkin methods for second order elliptic problems. *SIAM Journal on Numerical Analysis*, 47(2):1319–1365, 2009.

[35] D. Constantin and Z. S. Siwy. Poisson–Nernst–Planck model of ion current rectification through a nanofluidic diode. *Phys. Rev. E*, 76:041202, 2007.

[36] D. Constantin and Z. S. Siwy. Poisson-Nernst-Planck model of ion current rectification through a nanofluidic diode. *Phys. Rev. E*, 76(4):041202, 2007.

[37] B. Corry, S. Kuyucak, and S.-H. Chung. Tests of continuum theories as models of ion channels. ii. poisson–nernst–planck theory versus brownian dynamics. *Biophysical Journal*, 78(5):2364–2381, 2000.

[38] H. Daiguji, Y. Oka, , and K. Shirono. Nanofluidic diode and bipolar transistor. *Nano Letters*, 5(11):2274–2280, 2005.

[39] W. Dreyer, P. E. Druet, P. Gajewski, and C. Guhlke. Analysis of improved Nernst–Planck–Poisson models of compressible isothermal electrolytes. Part I: Derivation of the model and survey of the results, 2017. WIAS Berlin, preprint 2395.

[40] W. Dreyer, P. E. Druet, P. Gajewski, and C. Guhlke. Analysis of improved Nernst–Planck–Poisson models of compressible isothermal electrolytes. Part II: Approximation and a priori estimates, 2017. WIAS Berlin, preprint 2396.

[41] W. Dreyer, P. E. Druet, P. Gajewski, and C. Guhlke. Analysis of improved Nernst–Planck–Poisson models of compressible isothermal electrolytes. Part III: Compactness and convergence, 2017. WIAS Berlin, preprint 2397.

[42] W. Dreyer, C. Guhlke, and M. Landstorfer. A mixture theory of electrolytes containing solvation effects. *Electrochem. Commun.*, 43:75–78, 2014.

[43] W. Dreyer, C. Guhlke, and R. Müller. Overcoming the shortcomings of the Nernst–Planck model. *Phys. Chem. Chem. Phys.*, 15:7075–7086, 2013.

[44] W. Dreyer, C. Guhlke, and R. Müller. Overcoming the shortcomings of the nernst–planck model. *Physical Chemistry Chemical Physics*, 15(19):7075–7086, 2013.

[45] W. Dreyer, C. Guhlke, and R. Müller. Bulk-surface electro-thermodynamics and applications to electrochemistry. *WIAS-Preprint*, 2511, 2018.

[46] D. Boda E. Csányi, D. Gillespie, and T. Kristof. Current and selectivity in a model sodium channel under physiological conditions: Dynamic monte carlo simulations.

[47] M. Edidin. Lipids on the frontier: a century of cell-membrane bilayers. *Nature Reviews Molecular Cell Biology*, 4(5):414–418, 2003.

[48] W. R. Fawcett. *Liquids, Solutions, and Interfaces: From Classical Macroscopic Descriptions to Modern Microscopic Details*. Topics in Analytical Chemistry. Oxford University Press, New York, 2004.

[49] A. Fick. On liquid diffusion. *Journal of Membrane Science*, 100(1):33 – 38, 1995. The early history of membrane science selected papers celebrating vol. 100.

[50] J. Fuhrmann. Comparison and numerical treatment of generalised nernst–planck models. *Computer Physics Communications*, 196:166–178, 2015.

[51] J. Fuhrmann. Comparison and numerical treatment of generalised Nernst–Planck models. *Comput. Phys. Comm.*, 196:166–178, 2015.

[52] J. Fuhrmann. A numerical strategy for Nernst–Planck systems with solvation effect. *Fuel cells*, 16(6):704–714, 2016.

[53] J. Fuhrmann and C. Guhlke. A finite volume scheme for nernst-planck-poisson systems with ion size and solvation effects. In *International Conference on Finite Volumes for Complex Applications*, pages 497–505. Springer, 2017.

[54] J. Fuhrmann, C. Guhlke, A. Linke, Ch. Merdon, and R. Müller. Models and numerical methods for electrolyte flows. *WIAS-Preprint*, 2525, 2018.

[55] J. Fuhrmann, C. Guhlke, B. Matejczyk, and R. Muller. Transport of solvated ions in nanopores: Asymptotic models and numerical study. *WIAS preprints*, 2018.

[56] M. G. Fyta, S. Melchionna, E. Kaxiras, and S. Succi. Multiscale coupling of molecular dynamics and hydrodynamics: application to dna translocation through a nanopore. *Multiscale Modeling & Simulation*, 5(4):1156–1173, 2006.

[57] D. Gilbarg and N.S. Trudinger. *Elliptic partial differential equations of second order*, volume 224. Springer, 2001.

[58] D. Gillespie. Energetics of Divalent Selectivity in a Calcium Channel: The Ryanodine Receptor Case Study. *Biophys. J.*, 94(4):1169–1184, 2008.

[59] D. Gillespie. A review of steric interactions of ions: Why some theories succeed and others fail to account for ion size. *Microfluidics and Nanofluidics*, 18(5-6):717–738, 2015.

[60] D. T. Gillespie. A general method for numerically simulating the stochastic time evolution of coupled chemical reactions. *Journal of computational physics*, 22(4):403–434, 1976.

[61] Weihua Guan, Sylvia Xin Li, and Mark A Reed. Voltage gated ion and molecule transport in engineered nanochannels: theory, fabrication and applications. *Nanotechnology*, 25(12):122001, 2014.

[62] H. K. Gummel. A self-consistent iterative scheme for one-dimensional steady state transistor calculations. *IEEE Transactions on electron devices*, 11(10):455–465, 1964.

[63] O. P. Hamill, A. Marty, E. Neher, B. Sakmann, and F. J. Sigworth. Improved patch-clamp techniques for high-resolution current recording from cells and cell-free membrane patches. *Pflügers Archiv European journal of physiology*, 391(2):85–100, 1981.

[64] Z. Ható, D. Boda, and T. Kristóf. Simulation of steady-state diffusion: Driving force ensured by dual control volumes or local equilibrium monte carlo. *The Journal of chemical physics*, 137(5):054109, 2012.

[65] Z. Ható, D. Boda, and T. Kristóf. Simulation of steady-state diffusion: Driving force ensured by Dual Control Volumes or Local Equilibrium Monte Carlo. *J. Chem. Phys.*, 137(5):054109, 2012.

[66] Z. Ható, D. Boda, D.and Gillespie, G. Vrabec, J.and Rutkai, and T. Kristof. Simulation study of a rectifying bipolar ion channel: Detailed model versus reduced model. *arXiv preprint arXiv:1603.02440*, 2016.

[67] Z. Ható, M. Valiskó, T. Kristóf, D. Gillespie, and D. Boda. Multiscale modeling of a rectifying bipolar nanopore: explicit-water versus implicit-water simulations. *Physical Chemistry Chemical Physics*, 19(27):17816–17826, 2017.

[68] B. Hille et al. *Ion channels of excitable membranes*, volume 507. Sinauer Sunderland, MA, 2001.

[69] M. Hinze and R. Pinnau. An optimal control approach to semiconductor design. *Mathematical Models and Methods in Applied Sciences*, 12(01):89–107, 2002.

[70] M. Hinze and R. Pinnau. Second-order approach to optimal semiconductor design. *Journal of optimization theory and applications*, 133(2):179–199, 2007.

[71] C. Ho, R. Qiao, J. B. Heng, A. Chatterjee, R. J. Timp, N. R. Aluru, and G. Timp. Electrolytic transport through a synthetic nanometer-diameter pore. *Proceedings of the National Academy of Sciences of the United States of America*, 102(30):10445–10450, 2005.

[72] A. L. Hodgkin and A. F. Huxley. The components of membrane conductance in the giant axon of loligo. *The Journal of physiology*, 116(4):473–496, 1952.

[73] A. L. Hodgkin and A. F. Huxley. Currents carried by sodium and potassium ions through the membrane of the giant axon of loligo. *The Journal of physiology*, 116(4):449–472, 1952.

[74] A. L. Hodgkin and A. F. Huxley. A quantitative description of membrane current and its application to conduction and excitation in nerve. *The Journal of physiology*, 117(4):500–544, 1952.

[75] J. Hoffmann and D. Gillespie. Ion correlations in nanofluidic channels: effects of ion size, valence, and concentration on voltage-and pressure-driven currents. *Langmuir*, 29(4):1303–1317, 2013.

[76] P. Hohenberg and W. Kohn. Inhomogeneous electron gas. *Physical review*, 136(3B):B864, 1964.

[77] S. Howorka and Z. Siwy. Nanopore analytics: sensing of single molecules. *Chem. Soc. Rev.*, 38:2360–2384, 2009.

[78] S. Howorka and Z. Siwy. Nanopore analytics: sensing of single molecules. *Chem. Soc. Rev.*, 38(8):2360–2384, 2009.

[79] S. Howorka and Z. Siwy. Nanopores: Generation, engineering, and single-molecule applications. In *Handbook of single-molecule biophysics*, pages 293–339. Springer, 2009.

[80] S. Howorka and Z. S. Siwy. Nanopores as protein sensors. *Nat. Biotechnol.*, 30(6):506–507, jun 2012.

[81] L. R. Huang, P. Silberzan, J. O. Tegenfeldt, E. C Cox, J. C. Sturm, R. H. Austin, and H. Craighead. Role of molecular size in ratchet fractionation. *Physical review letters*, 89(17):178301, 2002.

[82] R. J. Hunter. *Zeta potential in colloid science: principles and applications*, volume 2. Academic press, 2013.

[83] N. E. Ilott, J. A. Heward, et al. Long non-coding rnas and enhancer rnas regulate the lipopolysaccharide-induced inflammatory response in human monocytes. *Nature communications*, 5, 2014.

[84] W. Im, S. Seefeld, and B. Roux. A grand canonical monte carlo–brownian dynamics algorithm for simulating ion channels. *Biophysical Journal*, 79(2):788–801, 2000.

[85] T. Streckenbach J. Fuhrmann et al. pdelib. `http://pdelib.org`, 2018.

[86] Z. Jiang and D. Stein. Charge regulation in nanopore ionic field-effect transistors. *Phys. Rev. E*, 83(3):031203, 2011.

[87] S. Jo, T. Kim, V. G. Iyer, and W. Im. Charmm-gui: A web-based graphical user interface for charmm. *Journal of Computational Chemistry*, 29(11):1859–1865, 2008.

[88] E. B. Kalman, I. Vlassiouk, and Z. S. Siwy. Nanofluidic bipolar transistors. *Adv. Mater.*, 20(2):293–297, 2008.

[89] M. Karhanek, J. T. Kemp, N. Pourmand, R. W. Davis, and C. D. Webb. Single dna molecule detection using nanopipettes and nanoparticles. *Nano letters*, 5(2):403–407, 2005.

[90] R. Karnik, C. Duan, K. Castelino, H. Daiguji, and A. Majumdar. Rectification of ionic current in a nanofluidic diode. *Nano Lett.*, 7(3):547–551, 2007.

[91] D. Kinderlehrer, L. Monsaingeon, and X. Xu. A wasserstein gradient flow approach to poisson- nernst- planck equations. *ESAIM: Control, Optimisation and Calculus of Variations*, 23(1):137–164, 2017.

[92] A. R. Leach. *Molecular modelling: principles and applications*. Pearson education, 2001.

[93] C. Lehrenfeld. Hybrid discontinuous galerkin methods for solving incompressible flow problems. *Rheinisch-Westfalischen Technischen Hochschule Aachen*, 2010.

[94] R. MacKinnon. Potassium channels and the atomic basis of selective ion conduction (nobel lecture). *Angewandte Chemie International Edition*, 43(33):4265–4277, 2004.

[95] E. Mádai, B. Matejczyk, A. Dallos, M. Valiskó, and D. Boda. Controlling ion transport through nanopores: modeling transistor behavior. *Physical Chemistry Chemical Physics*, 20(37):24156–24167, 2018.

[96] E. Mádai, M. Valiskó, A. Dallos, and D. Boda. Simulation of a model nanopore sensor: Ion competition underlines device behavior. *J. Chem. Phys.*, 147(24):244702, 2017.

[97] A. Malasics and D. Boda. An efficient iterative grand canonical monte carlo algorithm to determine individual ionic chemical potentials in electrolytes. *J. Chem. Phys.*, 132(24):244103, 2010.

[98] P. A Markowich. *The stationary semiconductor device equations*, volume 1. Springer Science & Business Media, 1985.

[99] P. A. Markowich, C. A. Ringhofer, and C. Schmeiser. *Semiconductor equations*. Springer-Verlag New York, Inc., 1990.

[100] P. A. Markowich, C.A. Ringhofer, and C. Schmeiser. An asymptotic analysis of one-dimensional models of semiconductor devices. *IMA Journal of Applied Mathematics*, 37(1):1–24, 1986.

[101] P. A. Markowich and C. Schmeiser. Uniform asymptotic representation of solutions of the basic semiconductor-device equations. *IMA Journal of Applied Mathematics*, 36(1):43–57, 1986.

[102] B. Matejczyk, J.-F. Pietschmann, M.-T. Wolfram, and G. Richardson. Asymptotic models for transport in large aspect ratio nanopores. *European Journal of Applied Mathematics*, pages 1–28, 2018.

[103] B. Matejczyk, M. Valiskó, M.-T. Wolfram, J.-F. Pietschmann, and D. Boda. Multiscale modeling of a rectifying bipolar nanopore: Comparing poisson-nernst-planck to monte carlo. *J. Chem. Phys.*, 146(12):124125, 2017.

[104] J. Mergheim, E. Kuhl, and P. Steinmann. A hybrid discontinuous galerkin/interface method for the computational modelling of failure. *Communications in numerical methods in engineering*, 20(7):511–519, 2004.

[105] S. P. Mielke, N. Grønbech-Jensen, and C. J. Benham. Brownian dynamics of double-stranded dna in periodic systems with discrete salt. *Physical Review E*, 77(3):031924, 2008.

[106] W. Nernst. *Reasoning of theoretical chemistry: Nine papers (1889?1921).* Verlag Harri Deutsch, 2003.

[107] G. Nguyen, I. Vlassiouk, and Z. S Siwy. Comparison of bipolar and unipolar ionic diodes. *Nanotech.*, 21(26):265301, 2010.

[108] E. R. Nightingale. Phenomenological theory of ion solvation. effective radii of hydrated ions. *The Journal of Physical Chemistry*, 63(9):1381–1387, 1959.

[109] W. Nonner, D. P. Chen, and B. Eisenberg. Progress and prospects in permeation. *The Journal of general physiology*, 113(6):773–782, 1999.

[110] O. Otto and U. F. Keyser. DNA translocation. In *Engineered Nanopores for Bioanalytical Applications*, pages 31–58. Elsevier BV, 2013.

[111] S. Ovchinnikov, H. Kamisetty, and D. Baker. Robust and accurate prediction of residue–residue interactions across protein interfaces using evolutionary information. *Elife*, 3:e02030, 2014.

[112] G. Pardon and W. van der Wijngaart. Modeling and simulation of electrostatically gated nanochannels. *Adv. Coll. Interf. Sci.*, 199-200:78–94, 2013.

[113] H. Peng, B. Luan, and G. Stolovitzky. Nanopore-based DNA sequencing and DNA motion control. In *Nanopores*, pages 255–286. Springer Nature, 2011.

[114] C. Peter and G.Hummer. Ion transport through membrane-spanning nanopores studied by molecular dynamics simulations and continuum electrostatics calculations. *Biophysical Journal*, 89(4):2222 – 2234, 2005.

[115] J.-F. Pietschmann, M.-T. Wolfram, M. Burger, C. Trautmann, G. Nguyen, M. Pevarnik, V. Bayer, and Z. Siwy. Rectification properties of conically

shaped nanopores: consequences of miniaturization. *Phys. Chem. Chem. Phys.*, 15:16917–16926, 2013.

[116] R. Pinnau, S. Rau, F. Schneider, and O. Tse. The semi-classical limit of an optimal design problem for the stationary quantum drift-diffusion model. *arXiv preprint arXiv:1402.5518*, 2014.

[117] A. Piruska, M. Gong, and J. V. Sweedler. Nanofluidics in chemical analysis. *Chem. Soc. Rev.*, 39:1060–1072, 2010.

[118] A. I. Prilepko, D. G. Orlovsky, I. A. Vasin, et al. *Methods for solving inverse problems in mathematical physics*. CRC Press, 2000.

[119] A. Prohl and M. Schmuck. Convergent finite element discretizations of the navier-stokes-nernst-planck-poisson system. *ESAIM: Mathematical Modelling and Numerical Analysis*, 44(3):531–571, 2010.

[120] V. G. Romanov. *Inverse problems of mathematical physics*. Walter de Gruyter GmbH & Co KG, 2018.

[121] D.L. Scharfetter and H.K. Gummel. Large-signal analysis of a silicon Read diode oscillator. *IEEE Trans. Electron. Dev.*, 16(1):64–77, 1969.

[122] T. Schirmer and P. S. Phale. Brownian dynamics simulation of ion flow through porin channels. *Journal of molecular biology*, 294(5):1159–1167, 1999.

[123] B.A. Schlake. Mathematical models for particle transport: Crowded motion. *Westfälische Wilhelms-Universität Münster*, 2011.

[124] M. Schmuck. Analysis of the navier–stokes–nernst–planck–poisson system. *Mathematical Models and Methods in Applied Sciences*, 19(06):993–1014, 2009.

[125] J. Schöberl. Netgen an advancing front 2d/3d-mesh generator based on abstract rules. *Computing and visualization in science*, 1(1):41–52, 1997.

[126] L. T. Sexton, L. P. Horne, and C. R. Martin. Developing synthetic conical nanopores for biosensing applications. *Mol. BioSyst.*, 3:667–685, 2007.

[127] A. Singer, D. Gillespie, J. Norbury, and R.S. Eisenberg. Singular perturbation analysis of the steady-state Poisson–Nernst–Planck system: Applications to ion channels. *European Journal of Applied Mathematics*, 19(5):541?560, 2008.

[128] K. P. Singh and C. Guo. Current-voltage characteristics influenced by the nanochannel diameter and surface charge density in a fluidic field-effect-transistor. *Phys. Chem. Chem. Phys.*, 19(24):15701–15708, 2017.

[129] K. P. Singh and M. Kumar. Effect of nanochannel diameter and debye length on ion current rectification in a fluidic bipolar diode. *J. Phys. Chem. C*, 115(46):22917–22924, 2011.

[130] K. P. Singh and M. Kumar. Effect of surface charge density and electro-osmotic flow on ionic current in a bipolar nanopore fluidic diode. *J. Appl. Phys.*, 110(8), 2011.

[131] K. P. Singh and M. Kumar. Effect of gate length and dielectric thickness on ion and fluid transport in a fluidic nanochannel. *Lab Chip*, 12:1332–1339, 2012.

[132] K. P. Singh, K. Kumari, and M. Kumar. Field-effect control of electrokinetic ion transport in a nanofluidic channel. *J. Appl. Phys.*, 110(8), 2011.

[133] K. P. Singh, K. Kumari, and M. Kumar. Ion current rectification in a fluidic bipolar nanochannel with smooth junction. *Appl. Phys. Lett.*, 99(11), 2011.

[134] Z. Siwy, P. Apel, D. Baur, D.D. Dobrev, Y.E. Korchev, R. Neumann, R. Spohr, C. Trautmann, and K.O. Voss. Preparation of synthetic nanopores with transport properties analogous to biological channels. *Surf. Sci.*, 532:1061–1066, 2003.

[135] A. Szymczyk, H. Zhu, and B. Balannec. Ion rejection properties of nanopores with bipolar fixed charge distributions. *J. Phys. Chem. B*, 114(31):10143–10150, aug 2010.

[136] M. Tajparast, G. Virdi, and M. I. Glavinović. Spatial profiles of potential, ion concentration and flux in short unipolar and bipolar nanopores. *Biochim. Biophys. Acta (BBA) - Biomem.*, 1848(10, Part A):2138–2153, 2015.

[137] M. Valiskó, D. Gillespie, and D. Boda. Selective adsorption of ions with different diameter and valence at highly-charged interfaces. *J. Phys. Chem. C*, 111(43):15575–15585, 2007.

[138] M. Valisko, B. Matejczyk, T. Kristóf Z. Hato, E. Madai, D.Fertig, D. Gillespie, and D. Boda. Multiscale analysis of the effect of surface charge pattern on a nanopore's rectification and selectivity properties: from all-atom model to poisson-nernst-planck. *In press*, 2019.

[139] L. van Oeffelen, W. Van Roy, H. Idrissi, D. Charlier, L. Lagae, and G. Borghs. Ion current rectification, limiting and overlimiting conductances in nanopores. *PLOS ONE*, 10(5):e0124171, may 2015.

[140] I. Vlassiouk, T. R. Kozel, and Z. S. Siwy. Biosensing with Nanofluidic diodes. *J. Am. Chem. Soc.*, 131(23):8211–8220, 2009.

[141] I. Vlassiouk and Z. S. Siwy. Nanofluidic diode. *Nano Lett.*, 7(3):552–556, 2007.

[142] I. Vlassiouk, S. Smirnov, and Z. Siwy. Ionic selectivity of single nanochannels. *Nano Lett.*, 8(7):1978–1985, 2008.

[143] I. Vlassiouk, S. Smirnov, and Z. Siwy. Nanofluidic ionic diodes. comparison of analytical and numerical solutions. *Acs Nano*, 2(8):1589–1602, 2008.

[144] I. Vlassiouk, S. Smirnov, and Z. Siwy. Nanofluidic ionic diodes. comparison of analytical and numerical solutions. *ACS Nano*, 2(8):1589–1602, 2008.

[145] A. V. Volkov, K. Tybrandt, M. Berggren, and I. V. Zozoulenko. Modeling of charge transport in ion bipolar junction transistors. *Langmuir*, 30(23):6999–7005, 2014.

[146] G.-W. Wei, Q. Zheng, Z. Chen, and K. Xia. Variational multiscale models for charge transport. *siam REVIEW*, 54(4):699–754, 2012.

[147] M-T. Wolfram. Inverse dopant profiling from transient measurements. *Journal of Computational Electronics*, 6(4):409–420, 2007.

[148] X. M. Xia, B. Fakler, A. Rivard, G. Wayman, et al. Mechanism of calcium gating in small-conductance calcium-activated potassium channels. *Nature*, 395(6701):503, 1998.

[149] R. Yan, W. Liang, R. Fan, and P. Yang. Nanofluidic diodes based on nanotube heterojunctions. *Nano Lett.*, 9(11):3820–3825, 2009.

[150] Z. Yang, T.A. Van, D. Straaten, U. Ravaioli, and Y. Liu. A coupled 3-d PNP/ECP model for ion transport in biological ion channels. *Journal of Computational Electronics*, 4(1):167–170, 2005.

[151] L.-H. Yeh, Y. Ma, S. Xue, and S. Qian. Gate manipulation of ionic conductance in a nanochannel with overlapped electric double layers. *Sensors and Actuators B: Chemical*, 215:266–271, 2015.

[152] Z.Siwy. Nanopore, 2002.